

UNIVERSITÀ DEGLI STUDI DI TRIESTE  
XXVIII CICLO DEL DOTTORATO DI RICERCA IN FISICA

**Environment-driven evolution of galaxies in  
CLASH-VLT clusters**

SETTORE SCIENTIFICO-DISCIPLINARE: FIS/05

*Coordinatore:*

PROF. PAOLO CAMERINI

*Dottoranda:*

MARIANNA

ANNUNZIATELLA

*Supervisore:*

DR. ANDREA BIVIANO

*Co-Supervisore:*

PROF. MARISA GIRARDI

Anno Accademico 2014/15



---

Università di Trieste  
Dottorato di Ricerca in Fisica - XXVIII ciclo  
PhD thesis summary

## Environment-driven evolution in CLASH-VLT clusters

Candidate: Marianna Annunziatella  
Supervisor: A. Biviano  
Co-Supervisor: Prof. M. Girardi

The analysis of data from recent large spectroscopic and photometric surveys has shown that galaxy properties have a bimodal distribution (e.g., Kauffmann et al. 2003). Two main populations of galaxies can be identified, the bulge-dominated, high-mass, red galaxies with low star formation rate (SFR), and the disk-dominated, low-mass, blue, and high-SFR galaxies. Blue galaxies are the dominant population at high redshifts and in low-density environments, while red galaxies take over at lower redshifts and in high-density environments. One of the key question in this context is whether these correlations are intrinsic of the galaxy populations from their formation epoch ('nature' hypothesis) or they are the result of an environment-driven evolution ('nurture' scenario). In this context, the analysis of galaxy populations in massive clusters, characterized by the highest number densities in the Universe, is an ideal tool to shed some light on galaxy evolution, since clusters offer rather extreme physical conditions for the galaxies they host.

My work has been focused on investigating the mechanisms which drive the evolution of galaxies in clusters from the Cluster Lensing And Supernova survey with Hubble (CLASH; <http://www.stsci.edu/postman/CLASH/Home.html>, P.I.: M. Postman) sample and, more specifically, in the subsample of clusters with spectroscopic follow-up from the CLASH-VLT survey (P.I.: P. Rosati) in the redshift range  $z \sim 0.2 - 0.5$ . These spectroscopic data are complemented by wide-field images obtained with Subaru in five photometric bands (B, V, R, I and z) and by Hubble Space Telescope ACS and WFC3 observations in 16 optical/IR bands in the central regions of clusters.

First, in Annunziatella et al. 2014, I analyzed galaxy populations in the CLASH cluster MACS J1206-0847 (M1206), at  $z \sim 0.44$ . The first observable that I examined was the galaxy stellar mass function, i.e. the distribution function of galaxy stel-

lar masses. With the spectroscopic and photometric data available for this cluster, I determined the stellar masses,  $M^*$ , of cluster member galaxies. Using these, I investigated the stellar mass function (SMF) of cluster galaxies down to the mass limit of  $M_* = 10^{9.5} M_\odot$ , and its dependence on galaxy type (Star-forming and Passive galaxies), and environment. The SMF shows a strong, statistically significant dependence on galaxy type. In particular, the SMF of Star-forming (SF) galaxies tends to contain many galaxies with small masses (e.g below  $M_* = 10^{10} M_\odot$ ), resulting in a steeper mass function than that of Passive galaxies. This dependence is valid in the whole cluster as well as in different cluster regions. I characterized the environment in terms of local number density and clustercentric distance. The results obtained from the two definitions are completely equivalent. I found an environmental dependence of the SMF of Passive galaxies, in terms of a decreasing slope, in absolute value, in the densest cluster region with respect to that found in less dense regions. This steeper slope is related to a lack of subgiant galaxies ( $M_*/M_\odot \leq 10^{10.5}$ ) near the cluster center. This result suggests that subgiant galaxies have been either totally destroyed or mass-stripped below the completeness limit of our survey, becoming one of the main contributors to the intra-cluster light (ICL). Further support to this scenario comes from the agreement at  $\sim 1\sigma$  level between the difference in mass in the subgiant mass range between the densest and less dense cluster regions in M1206, and the mass of the ICL derived for this cluster (Presotto et al. 2014). The lack of subgiant galaxies in the cluster core is also visible in the ratio between the number and stellar mass density profiles. In this cluster there was no evidence of dynamical friction, either in the SMF of Passive galaxies, nor in the comparison between stellar and total mass density profiles.

In Annunziatella et al. (2015, A&A in press), I extended the analysis of galaxy populations to the CLASH cluster Abell 209 ( $\langle z \rangle \sim 0.209$ , hereafter A209). Because of the cluster lower redshift, a lower mass limit ( $M_* = 10^{8.6} M_\odot$ ) could be reached than in M1206. The SMF of Passive galaxies in this cluster is significantly different from that found in M1206, with a much steeper slope. In A209 the SMF of Passive galaxies shows a double component, more evident in lower density regions. In agreement with Peng et al. (2010), the SMF can be interpreted as the combination of the SMF of mass quenched galaxies at masses  $M^* > 10^{10} M_\odot$ , and the SMF of SF galaxies turned into Passive by “environmental quenching” at lower masses. In order to understand which are the processes that drive the evolution of galaxies in A209, I analyzed the mass-size relation of Passive early type galaxies (ETGs), separating the sample in low ( $M_* \leq 10^{10} M_\odot$ ) and high-mass galaxies ( $M_* \geq 10^{10} M_\odot$ ).



I found that low-mass galaxies follow a flatter relation than the one of high-mass galaxies. The relation of low-mass ETGs galaxies was in agreement, within  $1\sigma$ , with the relation for star-forming galaxies at similar redshift. This suggest that the mechanism responsible for the quenching of star-forming galaxies should also affect the galaxy morphology changing late types into early ones. Furthermore, according to the analysis of the SMF, the number of low-mass Passive galaxies increases in the external regions of the cluster, implying that the quenching mechanism has to be effective also at large radii. This and the possible change in galaxy morphology indicate harassment (Treu et al. 2003) as the main process responsible for the environmental quenching in A209. In the densest region of the cluster, the second component of the SMF of Passive galaxies is suppressed, due to a lack of subgiant galaxies. Moreover, when referring to a single Schechter parametrization, the slope of the SMF of Passive galaxies shows a similar trend to that observed in M1206, with a smaller slope in absolute value in the densest cluster region. In order to verify the scenario of the ICL formation proposed to explain the results obtained in M1206, I also analyzed the ICL component in this cluster, by evaluating its mass content and its color profile. The color of the ICL was found to be compatible with the color of Passive cluster members. This, together with the comparison between the missing mass from subgiant galaxies in the cluster core and the ICL mass, indicated that in A209 the main channel of formation of the ICL is the disruption of Passive subgiant galaxies, in particular in the mass range  $10^{9.0} < M_{\star} < 10^{10.0} M_{\odot}$ . Additional support to this scenario can come from the analysis of galaxy orbits in the cluster. I derived the orbits of Passive cluster members dividing the sample in low and high mass galaxies. Low-mass Passive galaxies are characterized by tangential orbits that avoid small pericenters, presumably because those that cross the cluster center get tidally destroyed. More massive galaxies shows, instead, radial orbits near the cluster center, suggesting that they can penetrate through dense cluster inner environments. The effect of dynamical friction is evident both in the SMF of passive galaxies, in terms of higher  $M^*$  towards the cluster center, and from the ratio between the tellar mass density and the number density profiles. This effect was not observed in the higher- $z$  cluster in M1206, and this suggest a characteristic timescale for the processes of  $\sim 2$  Gyr.

In conclusion, in my thesis I have shown that a full understanding of galaxy evolution in clusters requires the analysis of the contribution of the ICL and subgiant galaxies to the stellar mass, and the information on galaxy stellar populations, structural properties, as well as on galaxy kinematics. My analyses have shown that a

consistent scenario for galaxy evolution in clusters can be built by taking into account several, diverse physical processes, such as harassment, tidal stripping and destruction and dynamical friction.

# Contents

---

<b>1</b>	<b>Introduction</b>	<b>3</b>
1.1	Cluster of galaxies . . . . .	3
1.2	Galaxies in clusters: observational properties . . . . .	5
1.3	Galaxies in clusters: dynamics . . . . .	8
1.4	Physical processes effective in clusters . . . . .	11
1.5	Intracluster light . . . . .	17
1.6	This thesis . . . . .	19
<b>2</b>	<b>Data sample</b>	<b>21</b>
2.1	Cluster Lensing And Supernova Survey with Hubble (CLASH) . . .	21
2.1.1	Supporting observations . . . . .	24
2.2	CLASH-VLT followup . . . . .	25
2.3	Spectroscopic dataset . . . . .	26
2.3.1	Spectroscopic members identification . . . . .	26
2.4	Photometric dataset . . . . .	27
2.4.1	Photometric catalogs . . . . .	27
2.4.2	Photometric members selection . . . . .	30
2.4.3	Completeness and membership corrections . . . . .	31
2.5	Mass estimates - SED fitting technique . . . . .	32
2.6	Structural parameters - Sérsic fit . . . . .	36
<b>3</b>	<b>MACS1206-0847</b>	<b>39</b>
3.1	Introduction . . . . .	39
3.2	Main properties of M1206 . . . . .	42
3.3	The stellar mass function . . . . .	49
3.3.1	Different galaxy types . . . . .	51

---

3.3.2	Different environments . . . . .	52
3.4	The stellar mass density profile . . . . .	62
3.5	Discussion . . . . .	65
<b>4</b>	<b>Abell 209</b>	<b>71</b>
4.1	Introduction . . . . .	71
4.2	The A209 data sample . . . . .	73
4.3	The stellar mass function . . . . .	78
4.3.1	Different galaxy types . . . . .	78
4.3.2	Effects of global and local environments . . . . .	82
4.3.3	Double Schechter . . . . .	89
4.4	The Intra-cluster light . . . . .	93
4.4.1	ICL detection method . . . . .	94
4.4.2	ICL properties . . . . .	94
4.5	Orbits of passive galaxies . . . . .	97
4.6	Mass-size relation . . . . .	99
4.7	The stellar mass density profile . . . . .	105
4.8	Discussion . . . . .	106
4.8.1	Environmental dependence of the stellar mass function . . . . .	106
4.8.2	The origin of the intra-cluster light . . . . .	108
4.8.3	The differential evolution of high and low-mass galaxies . . . . .	108
4.8.4	Evidence of dynamical friction in stellar mass density profile . . . . .	109
<b>5</b>	<b>Conclusions</b>	<b>111</b>
	<b>Bibliography</b>	<b>117</b>

# Introduction

---

Galaxies are often defined as “the building blocks of the Universe”. However, how do they form, evolve, acquire their morphological appearance, is still a matter of debate. They exhibit a bimodality in a various range of properties. What is the origin of this bimodality? How does the environment in which they reside influence their evolution? Many theoretical models have been proposed to answer these questions. However, we still need to constrain many observational properties to discriminate between different evolutionary scenarios. In this context, the analysis of galaxy populations in massive clusters, characterized by the highest number densities in the Universe, is an ideal tool to shed some light on galaxy evolution, since clusters offer rather extreme physical conditions for the galaxies they host.

## 1.1 Cluster of galaxies

According to the current cosmological paradigm, structure formation arises from gravitational instabilities amplifying perturbations in the cold dark matter (CDM) density field. At early epochs the perturbations were linear in amplitude, and well described by a Gaussian random field with a known power spectrum. At later times, density perturbations became nonlinear and collapsed into gravitationally bound systems. According to the hierarchical scenario, structures form in a “bottom up” way, with smaller masses reaching first virialization and then growing by accretion

and mergers (Carlberg, 1993; Peacock, 1999). Hence, galaxy clusters correspond to the collapse of the largest gravitationally bound over-densities. The formation of galaxy clusters is rather recent (since  $z \sim 1$ ), therefore they can be used to study different mechanisms leading to the evolution of galaxies and to test different models of structures formation. According to the  $\Lambda$ CDM paradigm, only a small percentage of the total galaxy cluster mass is in the form of baryonic matter, the remain is indeed made of Dark Matter (DM). In fact, galaxy clusters are enclosed in extended DM halos, that can in turn shape the properties of the cluster itself, such as the cluster mass function (number of clusters above a given mass threshold), and clustering properties. The first evidence of dark matter was found in the 1930s by Fritz Zwicky in the Coma cluster (Zwicky, 1933), when he noted a large discrepancy between its virial and luminous mass. According to the DM cosmological numerical simulations, the density distribution of DM halos is universal, and can be characterized by the so-called Navarro, Frenk & White (NFW) profile (Navarro et al., 1997b):

$$\frac{\rho(r)}{\rho_{crit}} = \frac{\delta_c}{(r/r_s)(1 + r/r_s)^2}, \quad (1.1)$$

where  $\rho_{crit} = \frac{3H^2}{8\pi G}$  is the critical density in an Einstein-de Sitter Universe,  $r_s$  is the scale radius,  $G$  and  $H$  are the gravitational and Hubble constants, and

$$\delta_c = \frac{200}{3} c^3 / [\ln(1 + c - c/(1 + c))] \quad (1.2)$$

is the characteristic (dimensionless) density contrast. The concentration parameter,  $c$ , is defined as  $r_{200}/r_s$ , where  $r_{200}$  is the radius within which  $\rho(r < r_{200}) = 200\rho_{crit}$  and is usually identified with the virial radius. The mass profile deriving from the NFW model is given by:

$$M(r) = 4\pi\rho_{crit}r_s^3\delta_c(c) \left[ \ln(1 + cx) - \frac{cx}{1 + cx} \right], \quad (1.3)$$

where  $x = \frac{r}{r_s}$ . Several observations have confirmed that the NFW model provides a good fit to the mass distribution of clusters (Carlberg et al., 1997; Umetsu et al., 2011; Okabe et al., 2013).

The baryonic component constitutes  $\sim 14\% - 16\%$  (Komatsu et al., 2011; Gonzalez et al., 2013) of the cluster content. Most of this is in the form of an intra-cluster medium (ICM) and is constituted from hot gas emitting in the X-ray, while the remaining few percents is embedded in stars and galaxies. The distribution of the

baryonic content among its components can help us to discriminate between different models for cluster assembly and evolution. In particular, the relative fraction in light or mass between brightest cluster galaxy (BCG), intracluster light (ICL), and satellite galaxies is a powerful tool to constrain models of evolution of cluster galaxies (Conroy et al., 2007).

## 1.2 Galaxies in clusters: observational properties

Galaxies have been first discovered in the late XIX century, while the first classification based on their appearance was made by E. P. Hubble in the 1926 (Hubble 1926). He classified them in four main classes, which can be represented by the so-called “tuning fork” (see Fig. 1.1). Going from left to the right in this diagram, galaxies can be identified as:

- Ellipticals: smooth objects with a shape which can be round or more elongated according to their ellipticity.
- Lenticulars (S0): initially they were considered as transition types between ellipticals and spirals. These galaxies have smooth profiles and do not show any sign of spiral arms. However, like spirals, they show a disk and a bulge.
- Spirals: they consist of a central spheroid, called *bulge*, and a *disk* with spiral arm structures. This class is further divided according to the presence of a bar in the bulge.
- Irregulars: these galaxies do not have any defined shape.

Elliptical and lenticular galaxies are together commonly referred to as *early-type* galaxies, while spirals and irregular galaxies as *late-types*. The reason behind this classification is that the Hubble diagram was originally thought as an evolutive sequence. Even if the evolutionary picture has been discarded, the nomenclature still remains. The distribution of light in galaxies is described by the by the Sérsic law,

$$I(R) = I_e \exp(-R/R_e)^{1/n} - 1, \quad (1.4)$$

where  $R_e$  is the effective radius, which contains half of the total light, and  $n$ , commonly known as the Sérsic index, controls the concentration of the light. Purely ellipticals follow the Sérsic law with  $n = 4$ , also known as de Vaucouleurs’ profile

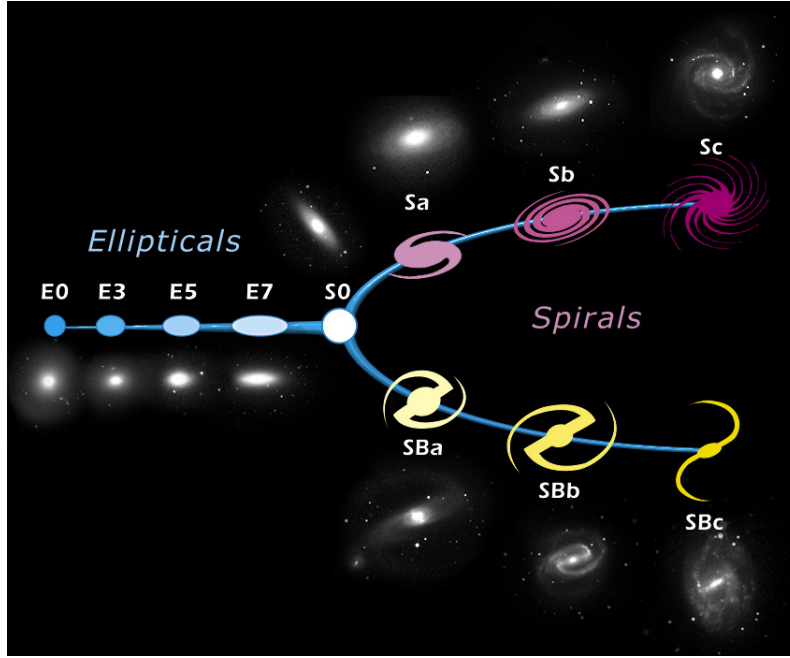


Figure 1.1. Representation of the Hubble *tuning fork* scheme.

(de Vaucouleurs, 1959), while purely disk galaxies follow the Sérsic law with  $n = 1$ . The Sérsic index is commonly used to discriminate between early-type ( $n > 2.5$ ), and late-type galaxies (Shen et al., 2003).

The two classes of galaxies obey to different scaling relations. For example, the luminosity of early type galaxies correlates with the stellar velocity dispersion (Faber and Jackson, 1976), with the galaxy effective radius (Fish, 1964), or with its surface brightness (Binggeli et al., 1984). Another correlation exists also between the surface brightness and the effective radius of elliptical galaxies (Kormendy, 1977). These relations are connected through the so-called *fundamental plane* (Djorgovski and Davis, 1987), which relates the stellar velocity dispersion, the effective radius and the effective surface brightness. There are analogous relations valid for late-type galaxies. For this class, the luminosity correlates with the rotational velocity associated to the stellar motion on circular orbits (Tully and Fisher, 1977).

Many other properties, other than their visual appearance can be used to classify galaxies. For example, they have been classified according to their color and their position on the color-magnitude (CM) diagram. The distribution of galaxy colors is, in fact, bimodal. Redder galaxies are in general brighter and occupy the so-called



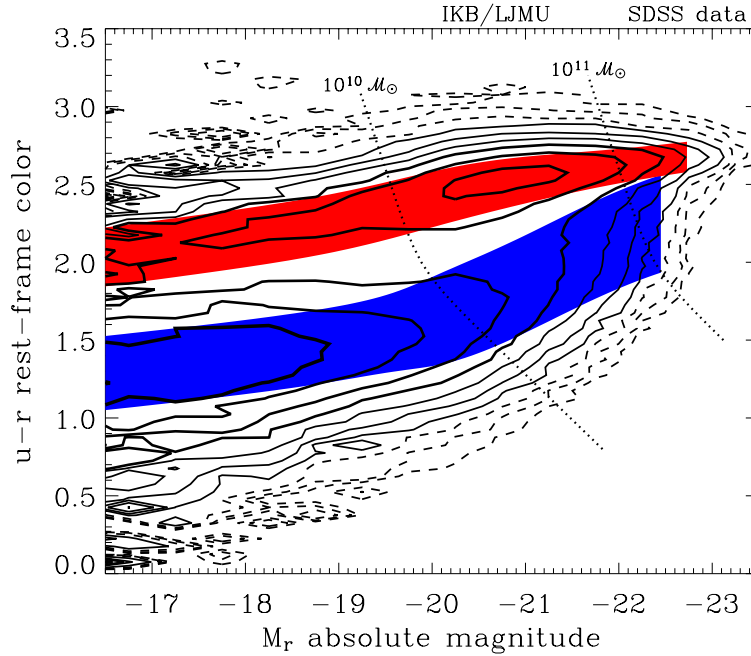


Figure 1.2. Color-magnitude distribution of galaxies from the Sloan Digital Sky Survey (SDSS) in the local Universe ( $z < 0.1$ ). Modified version of Fig. 2 of Baldry et al. (2004). Solid and dashed black contours represent the number density of galaxies, red and blue regions show the mean and dispersion ( $\pm 1\sigma$ ) of the red and blue sequences fitted in Baldry et al. (2004).

*red sequence* in the CM diagram, while bluer galaxies are fainter and located in the *blue cloud* (see Fig. 1.2). The CM relation holds in different environments from field to cluster galaxies and at different redshifts. From a morphological point, early-type galaxies are mostly located in the red-sequence, while late types tend to occupy the blue cloud (Tully et al., 1982). Galaxies tend to also segregate in stellar mass, as the blue population dominates the low-mass end of the distribution, while red sequence galaxies dominate the high-mass end.

The relative number fraction of different galaxy populations changes with redshift ( $z$ ) and with the local galaxy number density: blue galaxies are the dominant population at higher redshift and in low density environments, while red galaxies dominate at low density and at higher densities. The relation between galaxy type and the environment, also known as morphology-density relation (MDR), was first high-

lighted when studying nearby clusters: the first ones to quantify this effect were Oemler (1974) and Dressler (1980), while it was also found valid in groups (Postman and Geller, 1984) and compact groups of galaxies (Palumbo et al., 1995). According to the MDR, disk-like galaxies populate lower density regions, such as the field and cluster outskirts, while elliptical galaxies reside preferably in the higher density region like cluster cores. Postman et al. (2005) confirmed that the morphology-density relation holds also in clusters at higher redshift ( $0.8 < z < 1.2$ ). However at  $z \sim 1$ , they did observe a difference in the MDR due to a deficit of S0 galaxies and an excess of Sp+Irr galaxies relative to the local galaxy population.

Recent works based on wide-field surveys like the Sloan Digital Sky Survey (SDSS) have shown that the correlation between environment and morphology is valid not only in clusters, but over the full range of local density, from cluster cores to the field (Weinmann et al., 2006). Many physical processes can be responsible for the correlation between properties of galaxies and the environment in which they reside. One of the key question in this context is whether these correlations are intrinsic of the galaxy populations from their formation epoch ('nature' hypothesis) or they are the result of an environment-driven evolution ('nurture' scenario). In the following section, we give a review of the processes that can influence the evolution of a galaxy in different environments, and in particular in clusters.

### 1.3 Galaxies in clusters: dynamics

Galaxies in clusters can be considered as a non-collisional system which can be described by the *distribution function*  $f(\vec{x}, \vec{v}, t)$ , i.e. the density in the phase space. The number of objects lying in the volume  $d^3x$  centered in  $\vec{x}$  and having the velocity vector lying inside the volume  $d^3v$  centered in  $\vec{v}$  is given by the following relation:

$$dn = f(\vec{x}, \vec{v}, t) d^3x d^3v. \quad (1.5)$$

By definition  $f \geq 0$ . If the distribution function is known at the time  $t_0$ , it is possible to recover the configuration of the system at any time. For convenience we shall introduce the position vector in the phase space:

$$(\vec{x}, \vec{v}) \equiv \vec{w}, \quad (1.6a)$$

$$\dot{\vec{w}} = (\dot{\vec{x}}, \dot{\vec{v}}) = (\vec{v}, -\vec{\nabla}\Phi), \quad (1.6b)$$

where  $\Phi$  is the gravitational potential. Since in a non-collisional fluid there are no sudden changes in the particle position in the phase space, as we would have in case of collisions, it is possible to introduce a *continuity equation* for  $f$ :

$$\frac{\partial f}{\partial t} + \sum_{\alpha=1}^6 \frac{\partial(f\dot{w}_{\alpha})}{\partial w_{\alpha}} = 0. \quad (1.7)$$

Since  $x_i$  and  $v_i$  are independent coordinates in the phase space, the following relation holds:

$$\sum_{\alpha=1}^6 \frac{\partial \dot{w}_{\alpha}}{\partial w_{\alpha}} = \sum_{i=1}^3 \left( \frac{\partial v_i}{\partial x_i} + \frac{\partial \dot{v}_i}{\partial v_i} \right) = - \sum_{i=1}^3 \frac{\partial}{\partial v_i} \left( \frac{\partial \Phi}{\partial x_i} \right) = 0, \quad (1.8)$$

where the last equality is due to the fact that the gravitational potential does not depend on velocity. Using this relation in the eq. (1.7) we obtain the *non-collisional Boltzmann equation*:

$$\frac{\partial f}{\partial t} + \sum_{\alpha=1}^6 \dot{w}_{\alpha} \frac{\partial f}{\partial w_{\alpha}} = 0. \quad (1.9)$$

To better understand the meaning of this equation, we now recast it in another form by making use of the Lagrangian derivative:

$$\frac{df}{dt} = \frac{\partial f}{\partial t} + \sum_{\alpha=1}^6 \dot{w}_{\alpha} \frac{\partial f}{\partial w_{\alpha}}. \quad (1.10)$$

The collisionless Boltzmann equation then reads:

$$\frac{df}{dt} = 0. \quad (1.11)$$

This means that the fluid is incompressible in the phase space.

The distribution function  $f$  depends on 7 variables, therefore it is usually quite difficult to solve the collisionless Boltzmann equation. Still, the moments of eq. (1.11) can provide useful information. Such equation can be recast as follows:

$$\frac{\partial f}{\partial t} + \sum_{i=1}^3 \left( v_i \frac{\partial f}{\partial x_i} - \frac{\partial \Phi}{\partial x_i} \frac{\partial f}{\partial v_i} \right) = 0. \quad (1.12)$$

And integrating the velocities we obtain:

$$\int \frac{\partial f}{\partial t} d^3v + \int v_i \frac{\partial f}{\partial x_i} d^3v - \frac{\partial \Phi}{\partial x_i} \int \frac{\partial f}{\partial v_i} d^3v = 0, \quad (1.13)$$

where we have adopted the summation convention. The phase space volume within which we are integrating (this means all the velocities) does not depend on time and  $v_i$  does not depend on  $x_i$ . The time derivative and  $\partial/\partial x_i$  can be taken out of the integrals. The surface of the integration volume is composed by the velocities with modulus  $\infty$ . The theorem of the divergence states that  $\int_V \vec{\nabla} f d^3x = \int_S f \cdot \hat{n} d^2S$ , where  $\hat{n}$  is a versor perpendicular to the surface element  $d^2S$ . The last term of the equation vanishes, since there are no particles with infinite velocity. By defining the space density and the mean velocity as follows:

$$\nu \equiv \int f d^3v \quad \bar{v}_i \equiv \int f v_i d^3v, \quad (1.14)$$

eq. (1.13) reads:

$$\frac{\partial \nu}{\partial t} + \frac{\partial(\nu \bar{v}_i)}{\partial x_i} = 0. \quad (1.15)$$

Multiplying eq. (1.12) times  $v_j$ , integrating over the velocities and applying the divergence theorem we obtain:

$$\frac{\partial(\nu \bar{v}_j)}{\partial t} + \frac{\partial(\nu \bar{v}_i \bar{v}_j)}{\partial x_i} + \nu \frac{\partial \Phi}{\partial x_j} = 0, \quad (1.16)$$

where  $\overline{v_i v_j} \equiv \frac{1}{\nu} \int v_i v_j f d^3v$ . We can rewrite this equation by performing the following operation: (1.16)  $- \bar{v}_j$ (1.15). We obtain:

$$\frac{\partial \bar{v}_j}{\partial t} + \bar{v}_i \frac{\partial \bar{v}_j}{\partial x_i} = -\frac{\partial \Phi}{\partial x_j} - \frac{1}{\nu} \frac{\partial(\nu \sigma_{ij}^2)}{\partial x_i}, \quad (1.17)$$

where we have introduced the *stress tensor*, that describes an anisotropic pressure:

$$\sigma_{ij}^2 = \overline{(v_i - \bar{v}_i)(v_j - \bar{v}_j)} = \overline{v_i v_j} - \bar{v}_i \bar{v}_j. \quad (1.18)$$

The velocity field of the non-collisional matter provides a support to the system against the collapse in the same way the pressure does in a collisional system.

As presented in detail in Binney and Tremaine (1987), considering eq. (1.9) in spherical coordinates, and taking its moments we obtain the equivalent of eq. (1.17) in spherical coordinates:

$$\frac{d(\nu \bar{v}_r^2)}{dr} + \frac{\nu}{r} \left[ 2\bar{v}_r^2 - (\bar{v}_\theta^2 + \bar{v}_\phi^2) \right] = -\nu \frac{d\Phi}{dr}. \quad (1.19)$$

To obtain this equation one typically makes some simplifying assumptions.

1. Steady-state hydrodynamic equilibrium which implies:  $\frac{\partial}{\partial t} = 0$  and  $\bar{v}_r = 0$ .
2. Spherical symmetry which implies  $\bar{v}_\theta = \bar{v}_\phi = \sigma_{r\theta}^2 = \sigma_{r\phi}^2 = \sigma_{\theta\phi}^2 = 0$ .

Using the velocity dispersion  $\sigma$  instead of the velocity rms, we impose a further condition: let the system be invariant under rotations about the center. This means that the system appears statistically isotropic. This implies that  $\overline{\sigma_\theta^2} = \overline{\sigma_\phi^2}$ . Let us define the *velocity anisotropy parameter*:

$$\boxed{\beta = 1 - \frac{\sigma_t^2}{\sigma_r^2}}, \quad (1.20)$$

where  $\sigma_t = [\frac{\sigma_\theta^2 + \sigma_\phi^2}{2}]^{1/2}$  is the tangential velocity dispersion. The anisotropy parameter quantifies the anisotropy of the orbits. Negative values of  $\beta$  indicates that galaxies have tangential orbits, while positive values indicates radial orbits. Such anisotropy may be related to environmental processes effective in the cluster, like dynamical friction and tidal processes. The anisotropy parameter therefore provides important information about such processes. Cosmic structures form by the collapse of perturbations, therefore we may expect the radial velocity dispersion to be greater than the tangential component. Substituting the expression for the gravitational potential  $d\Phi/dr = GM(r)/r^2$ , eq. (1.19) reads:

$$\boxed{M(r) = -\frac{r\sigma_r^2}{G} \left( \frac{d \ln v}{d \ln r} + \frac{d \ln \sigma_r^2}{d \ln r} + 2\beta \right)}. \quad \text{Jeans equation} \quad (1.21)$$

Since this equation is derived from the Jeans equations (1.15)-(1.16)-(1.17), using a synecdoche we will refer to it as *the Jeans equation* hereafter. The particles that satisfy this equation are in equilibrium. It is possible to read this equation in another way: particles in equilibrium are tracers of the potentials because with their kinematics it is possible to infer the potential.

## 1.4 Physical processes effective in clusters

The processes that can affect the galaxy evolution, especially in high density environments like clusters, can be divided into two main classes: gravitational interactions, including all sorts of tidal interactions, and hydrodynamic interactions

between the galaxy interstellar medium (ISM) and the hot intra-cluster and intra-group medium (IGM or ICM). Below I will briefly discuss the most important among these processes. For more exhaustive reviews, see for example [Boselli et al. \(2006\)](#); [Biviano \(2008\)](#).

### Gravitational interactions

- **Dynamical friction.** A galaxy moving in a medium composed by DM particles feels a drag that slows it down due to gravitational interactions between DM particles and the galaxy itself. This force, first described by [Chandrasekhar \(1943\)](#), is the *dynamical friction*. DM particles tend to fall in the wake produced by the moving galaxy, creating an excess of density of matter behind the galaxy. This excess attracts gravitationally the galaxy, resulting in a drag force that is opposed to the motion of the galaxy, according to the following relation:

$$\frac{d}{dt}\vec{v}_{orb} = -4\pi G^2 \ln(\Lambda) M_{gal} \rho(< v_{orb}) \frac{\vec{v}_{orb}}{v_{orb}^3}, \quad (1.22)$$

where  $\rho(< v_{orb})$  is the density of background particles with velocities less than the orbital velocity  $v_{orb}$  of the galaxy,  $M_{gal}$  is the mass of the galaxy and  $\Lambda$  is the Coulomb logarithm (see, e.g. [Chandrasekhar, 1943](#); [White, 1976](#)). The effect of dynamical friction is that of making the galaxy lose energy and angular momentum, therefore sinking toward the center of the cluster and eventually merging with the central galaxy, on a time-scale ([Boylan-Kolchin et al., 2008](#)) given by

$$\tau_{df} \propto \frac{v_{gal}^3}{M_{gal}\rho}. \quad (1.23)$$

Therefore dynamical friction results to be more effective in higher density environments and for more massive galaxies and not very effective when the galaxy moves fast.

- **Galaxy-galaxy interactions (including mergers).** Tidal interactions among galaxy pairs involve all the components of the galaxies, from the dark matter halo, to gas, dust, and star content, with different efficiencies depending on the different binding degree between the various components. The timescale for a galaxy to experience a collision event is given by

$$\tau_c \propto \frac{1}{vr_{gal}^2 v_{gal}}, \quad (1.24)$$

where  $v_{gal}$  is the relative velocity between the two galaxies,  $r_{gal}$  is the galaxy radius, and  $\nu$  is the galaxy number density (Gnedin, 2003). From the previous equation it is evident that galaxy-galaxy interactions and mergers are more frequent in high-density regions. However, in these denser environment, their duration is shorter, due to the high relative velocities among galaxies. For this reason, they are likely to be more effective in the external cluster regions, where the relative speed of the encounters is not very high (Spitzer and Baade 1951, Negroponte and White 1983). Tidal interactions act more efficiently on the loose peripheral or extra-planar HI gas, than on the molecular gas, located in the inner potential well (Valluri and Jog, 1990). Numerical simulations have shown that mergers can also be responsible for morphological transformations from spiral galaxies to lenticulars and ellipticals, by destroying galactic disks, leaving a dynamically hot remnant (Toomre and Toomre, 1972). On the other hand, recent simulations by Mihos (2004), have shown that in the case of slow encounters, tidal interactions among galaxy pairs can drive the formation of spiral arms and in some cases of bars.

- **Tidal interactions between galaxies and the cluster potential well.** These interactions can induce in cluster galaxies gas inflow, bar formation, nuclear and disk star formation (Merritt 1984; Miller 1986; Byrd and Valtonen 1990). Depending on the inclination of the disk with respect to the orbital plane, due to these interactions its structure can be perturbed until spiral features form (disk parallel to the plane) or until the development of a bulge (Valluri, 1993).

- **Harassment.** Moore et al. (1996, 1998, 1999) proposed that the evolution of galaxies in clusters is the result of the combined effect of multiple high speed galaxy-galaxy close ( $\sim 50$  kpc) encounters with interaction with the whole cluster potential. This process was named galaxy harassment. The efficiency of this process depends on the clusters tidal field, on the collisional frequency, on the strength of each collision, and on the galaxy potential. The main effect of harassment is to heat the stellar component increasing the velocity dispersion and decreasing the angular momentum, and at the same time make the gas infall towards the galaxy center (Moore et al., 1996). Since harassment depends on the galaxy potential, it affects in different ways massive and dwarf galaxies. In particular, according to N-body simulations, low luminosity spirals are mostly affected by harassment, which can transform them into dwarf spheroidals. Small spheroidal galaxies can even be completely destroyed by harassment (Moore et al., 1999). Among bright spiral galaxies, those with high surface brightness, are relatively stable against the effect of galaxy harassment. The effect of the interaction is a small ( $0.5 \text{ mag arcsec}^{-2}$ ) increase of the central surface



brightness, with a fading of spiral features (Moore et al., 1999). The structural and kinematic properties of galaxies subjected to harassment, are similar to those of bright lenticulars. Low surface brightness galaxies are strongly influenced by harassment.

### Hydrodynamical interactions

- **Ram-pressure stripping.** The so-called ram-pressure is the process that strips the ISM from galaxies moving with velocities  $\sim 1000 \text{ km s}^{-1}$  in the hot ( $\sim 100 \text{ K}$ ) intra-cluster medium characterized by a mean density of  $\sim 10^3 - 10^4 \text{ atoms cm}^{-3}$  (Gunn and Gott, 1972). Ram-pressure, beside wiping away material from the stellar disk, can also affect galaxy morphology by forming a low density tail of gas (Quilis et al., 2000). The observational evidence of this process requires very high spatial resolution. Galaxies with this kind of features (see Fig.1.3) are called *jellyfish* and have been discovered recently (Ebeling et al., 2014). Ram-pressure is proportional to the



Figure 1.3. Evidence of gas tails in the galaxy 234144260358 belonging to the cluster Abell 2667 at  $z = 0.23$ . Color image composed from the ACS@HST images in the bands F450W, F606W, F814W (Cortese et al., 2007; Ebeling et al., 2014).



density of the intra-cluster medium and to the galaxy velocity, according to Eq. 1.25:

$$\rho_{ICM} v_{gal}^2 > \alpha \frac{GM_{gal} \rho_{gas}}{R_{gal}}, \quad (1.25)$$

where  $\rho_{ICM}$  is the ICM gas density,  $R_{gal}$  is the projected galaxy radius in the direction transverse to the galaxy motion,  $\rho_{gas}$  is the 3-D galaxy gas density profile and  $\alpha$  is a term that depends on the precise shape of the gas and mass profile of the galaxy (McCarthy et al., 2008). Approaching the cluster center both the galaxy velocity and the ICM density increase, thus increasing the ram-pressure. Therefore, the efficiency of ram pressure stripping depends strongly on the shape of the galaxy orbit within the cluster. Ram-pressure can trigger the star-formation of the galaxy on short timescales, by creating turbulent motions and thermal instabilities that increase cloud-cloud collision and collapse (Evrard, 1991). On longer timescales ( $> 10^8 yr$ ) however, the removal of the HI gas reservoir leads to a decrease of the fuel necessary to the star formation, thus turning galaxies into quiescent (e.g. Fujita, 1998).

- **Viscous stripping.** Nulsen (1982) proposed viscous stripping as a mechanism capable of removing the gas from galaxies in clusters. This mechanism removes the external layers of the ISM from the galaxy due to a viscosity momentum transfer. The effect of this process on the structural and kinematic properties, molecular gas content and star formation activity of galaxies is similar to that of ram-pressure.

- **Thermal evaporation.** This is another type of interaction between the ISM of galaxies in clusters and the IGM. Cowie and Songaila (1977) have shown that if the IGM temperature is high compared to the galaxy velocity dispersion, the temperature of the ISM rises rapidly, and the gas evaporates. This process drains the gas reservoir, hence it halts the star formation of the galaxy.

### Hybrid mechanisms

- **Starvation or Strangulation.** This mechanism, at variance with the ones proposed above with the exception of harassment, is most effective on large scales. Larson et al. (1980) first proposed this mechanism to explain the transformation of spirals into lenticulars. From numerical simulations, when a cluster collapses gas envelopes in disk galaxies are largely stripped away. On time scales of a few Gyr the galaxies would exhaust the available gas, quenching further star formation activity. Bekki et al. (2002) in their numerical simulations showed that even if a spiral orbits a cluster with a pericenter distance of 3 core radii, 80% of its halo is stripped within a

few Gyr by the hydrodynamical interaction with the ICM plus the global tidal field of the cluster, preventing gas accretion into the disk, and consequently suppressing the star formation.

- **Preprocessing.** In the hierarchical scenario of large scale structure formation, rich galaxy clusters form starting from infalling groups. These groups can therefore represent the natural sites for a preprocessing stage in the evolution of cluster galaxies through mechanisms, like tidal interactions among galaxy pairs, that are otherwise less effective in high-velocity environments such as cluster cores (Dressler et al., 2004; Mihos, 2004). It has been shown from numerical simulations that in these groups also ram-pressure, starvation and evaporation might be already effective from  $z \sim 0.5$  (Fujita, 2004). Preprocessing in groups could also drive the formation of lenticulars through unequal-mass mergers or minor mergers between spirals (Kodama et al., 2001).

The processes described above are effective in different regions of clusters (see for an example Fig. 3 of Treu et al. 2003). Many of them are also likely to be related

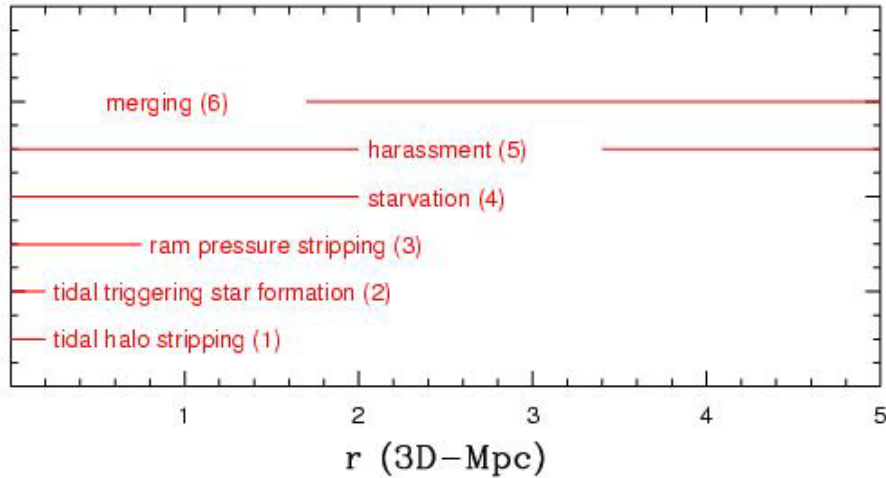


Figure 1.4. Figure taken from (Treu et al., 2003): summary of the regions where key physical mechanisms are likely to be more effective.

to galaxy orbits. Galaxies on radial orbits, characterized by small pericenters, can experience denser environments than galaxies on more tangential orbits. This can lead to their more rapid destruction (Taylor and Babul, 2004). It has been suggested by Solanes et al. (2001) that among Virgo cluster galaxies, those with evidence of gas stripping are on more radial orbits than the others.

The properties that are most likely to be influenced by these processes are: gas content, stellar mass, and morphological parameters like sizes or Sersic indices. Constraining the dependence of these properties from the environment can shed the light on the relative importance of these processes in shaping galaxy evolution.

## 1.5 Intracluster light

Part of the baryonic content of the cluster comes in form of a diffuse stellar component not gravitationally bound to cluster galaxies, i.e. the "intra-cluster light" (ICL). The discovery of the ICL dates back to Zwicky (1951) in the Coma cluster. The stars that constitute the ICL might originate from stripping of cluster member galaxies as the result of the interactions with either the cluster potential or with other members. However, it is still a matter of debate which is its major formation channel. From a theoretical point of view, the processes that can contribute to the formation of the ICL are several: disruption of dwarf galaxies (Conroy et al., 2007; Murante et al., 2007b; Purcell et al., 2007), tidal stripping of intermediate mass ( $10^{10} - 10^{11} M_{\odot}$ ) galaxies (Rudick et al., 2009; Laporte et al., 2013; Contini et al., 2014b), short-lived major mergers (Conroy et al., 2007; Murante et al., 2007b), stripping within galaxy groups accreting onto the cluster (Rudick et al., 2006). Finally, a percentage of the ICL may arise from in-situ star formation, wherein stars form in cold gas clouds stripped from infalling substructures (Puchwein et al., 2010). In a scenario where galaxy stripping and disruption are the main mechanisms for the production of the ICL, the major contribution comes from galaxies falling onto the cluster along almost radial orbits, since tidal interactions by the cluster potential are strongest for these galaxies (Contini et al., 2014b). It is still possible, however, that the formation of the ICL follows different path depending on the dynamical evolution of a particular cluster (Rudick et al., 2009). Some properties of the ICL, such as the radial profile, the color, and the presence of substructure are strictly linked to the accretion history and dynamical evolution of galaxy clusters. For example, the presence of tidal arcs can give information on the assembly history of the cluster. If the ICL is formed before the cluster has undergone virialization, the bulk of the ICL will be smooth with few faint tidal arcs. According to theoretical models these features are the result of recent interaction among galaxies with the cluster potential (Rudick et al. 2009). From an observational point of view, even if the ICL can shed light on many mechanisms occurring in galaxy clusters, it has proved very hard to study it due to its very

faint surface brightness, which is  $\sim 1\%$  of the night sky brightness. Ideally, the ICL is estimated as the residual light after having subtracted the contribution from all galaxies in the cluster including the BCG (Gonzalez et al., 2005). However, it is not always possible to perfectly fit the light distribution of each galaxy. For this reason, many works prefer to mask the galaxies down to a certain limit in surface brightness (Mihos et al., 2005; Zibetti et al., 2005; Montes and Trujillo, 2014) and attribute to the ICL the optical light coming from the outside of such boundaries. Recently, a hybrid method has been developed, which first fits a Sérsic profile to each galaxy and subtracts the best-fit model whenever it is possible, then it masks all the pixels which deviates more than a certain threshold from the sky brightness (Presotto et al., 2014). Information on the distribution and kinematics of the intra-cluster light have also been gathered through the presence of particular stars like supernovae (SN, Gal-Yam et al., 2003), red-giant branch (RGB) stars (Durrell et al., 2002), and planetary nebulas (PNs, Arnaboldi et al., 1996; Longobardi et al., 2015).

Beside characterizing the ICL properties related to the specific evolution of a single cluster, it is important to determine its contribution to the total baryon fraction. Observational studies have shown that the ICL fraction ranges from a few percent up to half of the optical light of the system (Feldmeier et al., 2004; Zibetti et al., 2005; Gonzalez et al., 2007; Guennou et al., 2012). It is not yet clear with which properties this fraction correlates and to what extent. Guennou et al. (2012) found a weak correlation between the ICL content and the cluster mass and no variation in the amount of ICL between  $z = 0.4$  and  $z = 0.8$ . The mildness or absence of this trends has been confirmed also at lower redshifts, i.e.,  $z < 0.3$ , (Zibetti et al., 2005; Krick and Bernstein, 2007). These findings are inconsistent with previous results from numerical simulations which claimed a positive correlation between ICL fraction and halo mass (Lin and Mohr, 2004; Murante et al., 2004; Purcell et al., 2007). However, more recent simulations suggest a much weaker dependence of the ICL fraction on cluster mass (Murante et al., 2007b; Puchwein et al., 2010; Cui et al., 2014).

The ICL is a promising and complementary way to understand the mechanisms occurring in galaxy cluster. The need for data at higher redshift is made even more stringent due to the fact that theoretical models agree that most of the ICL has formed at relatively young epoch ( $z \leq 1$ ) (Murante et al., 2007b; Conroy et al., 2007; Contini et al., 2014b). However, due to the fact that the surface brightness dimming scales with redshift as:  $(1+z)^4$ , there are only few detections at  $z > 0.3$  (Guennou et al., 2012; Montes and Trujillo, 2014; Presotto et al., 2014; DeMaio et al., 2015).

## 1.6 This thesis

This thesis is organized as follows.

In Chapter 2 I present the data used in this thesis. In particular I introduce the CLASH survey and its follow-up survey, CLASH-VLT. I describe how I derived the galaxy properties used in this work, focusing in particular on the data available for two of the CLASH clusters: MACS1206-0847 (hereafter M1206) and Abell 209 (hereafter A209).

In Chapter 3 I focus on how the environment shapes the galaxy stellar mass function in the higher redshift cluster M1206. I also compare the number, stellar and total density profiles in this cluster. By combining these informations, I set constraints on the evolutionary processes at work in M1206.

In Chapter 4 I analyze the distribution of galaxy stellar masses and the mass density profiles in the cluster Abell 209 at lower redshift than M1206. I also study some properties of the ICL in A209, in order to shed some light on which processes form the ICL and what type of galaxies are its progenitors.

To investigate further the evolution of galaxies in A209, I also carry out the dynamical analysis of the orbits of passive galaxies.

To discriminate between different quenching mechanisms into shaping the evolution of galaxies in this cluster, I also analyze the distribution of galaxy sizes.

In Chapter 5 I summarize the results obtained in the two clusters and draw my conclusion on which are the main processes that shape galaxy evolution on how they depend on redshift.



## Data sample

---

### 2.1 Cluster Lensing And Supernova Survey with Hubble (CLASH)

The number of clusters above a given mass limit as a function of redshift is sensitive to the geometry of the Universe and to the growth of large scale structures. Hence, galaxy clusters represent the bridge between astrophysics and cosmology. As said in Chapter 1, the mass budget of massive clusters is constituted for  $\sim 90\%$  in dark matter,  $\sim 10\%$  baryons, primarily hot X-ray-emitting plasma, and just  $\sim 1\%$  in stars. According to modern cosmology, clusters are associated to the largest (gravitationally bound) dark matter halos. Hence, their inner mass distribution can be used as a test for the current  $\Lambda$ CDM paradigm. This paradigm gives specific predictions for the mass density profiles of DM halos both at galaxy and cluster scales. Significant deviations from these theoretical predictions would imply a deviation from the  $\Lambda$ CDM paradigm: for example in the form of a different nature of dark matter. This could be revealed particularly in the inner, high-density cluster cores, where the inner slope of the mass distribution could be modified by a non-collisionless behavior of DM particles. To reveal discrepancies from theoretical predictions requires a very accurate measure of the inner mass distribution of a representative sample of clusters. This can be achieved by employing different techniques to determine the mass

distribution, like gravitational lensing, galaxy dynamics and X-ray hydrostatic equilibrium. In fact, each of these methods is most sensitive in a different radial range and is subjected to different systematic effects: structures along the line of sight for lensing, orbital anisotropy profiles for dynamical masses, deviations from hydrostatic equilibrium for X-ray masses. Combining these probes, one can in principle recover cluster density profiles with the required accuracy, provided a high quality and homogeneous dataset is available for a representative sample of clusters, with a known selection function. Among the different mass probes, strong gravitational lensing, can resolve the inner structure of dark matter halos down to galaxy scale, when a sufficient number of multiple images with distance information is available. In addition to this, close to the critical lines, clusters can magnify background galaxies by a factor of ten or more. Hence, massive clusters can also be used to discover very faint distant galaxies.

CLASH is a 524-orbit HST Multi-Cycle Treasury Program (Postman et al., 2012) which observed 25 massive clusters in the redshift range between  $0.2 < z < 0.9$  (Fig. 2.1) with the Wide-field Camera 3 (WFC3) and the new Advanced Camera for Surveys (ACS). This survey had four primary science goals.

1. Obtain the DM profile of galaxy clusters with unprecedented precision and resolution, using strong and weak gravitational lensing.
2. Measure the time dependence of the dark energy equation of state by detecting Type Ia supernovae out to redshift  $z \sim 2.5$ .
3. Detect the most distant galaxies yet discovered at  $z > 7$ .
4. Study the internal structure and evolution of cluster members and background and foreground galaxies.

The majority of the orbits (474 out of 524) were assigned to cluster imaging and to the parallel SN search program.

The majority of the CLASH sample is drawn from the MACS and Abell cluster catalogs (Ebeling et al., 2001b; Abell, 1958). Out of 25 clusters, 20 are selected to be “relaxed” according to their X-ray-morphology. This means that they have smooth X-ray emission and a BCG within a projected distance of 23 kpc of the X-ray centroid. One or more giant arcs are visible in at least 18 of the relaxed systems, so they ensure high quality strong lensing information HST imaging. Although the clusters



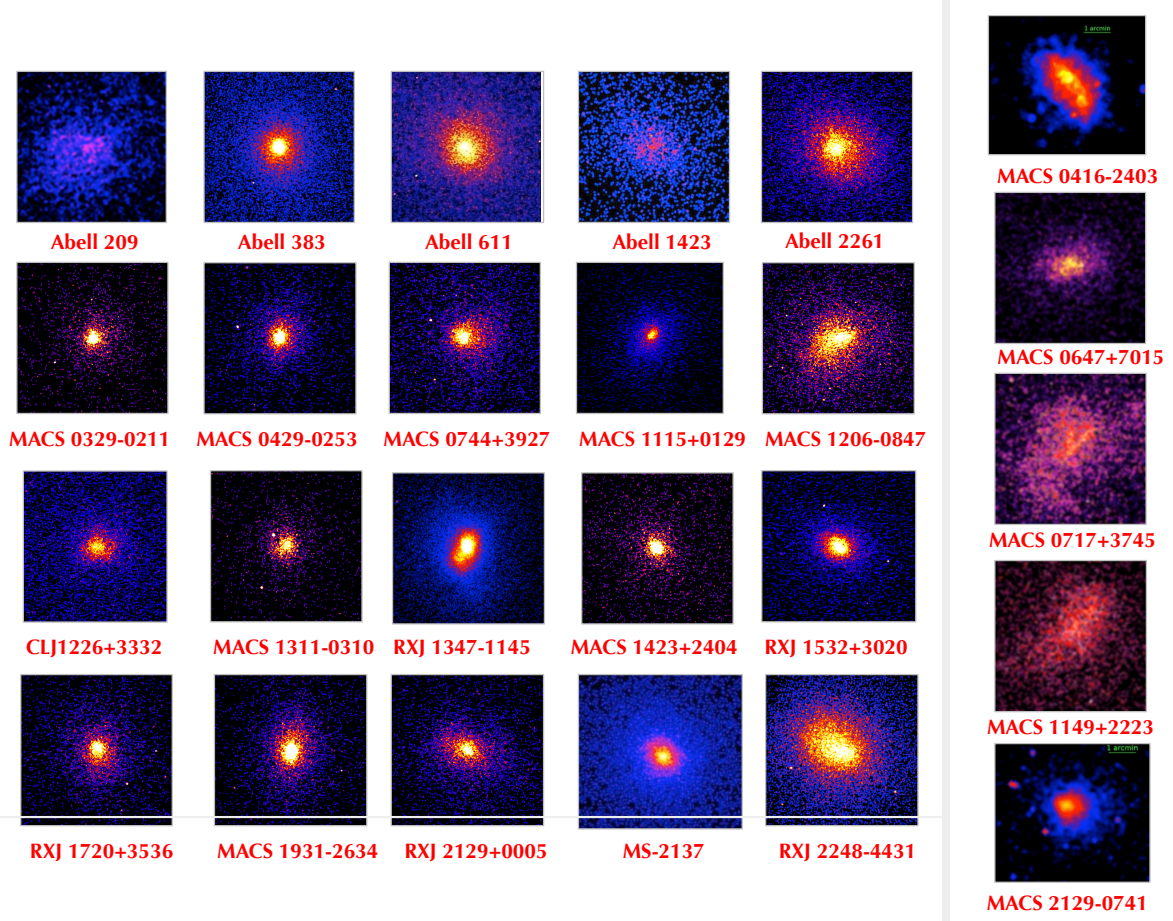


Figure 2.1. Chandra X-ray cut-out images centered on the 20 CLASH “relaxed” clusters, plus the X-ray images of the 5 strongly lensing systems (last column). The images are taken from [Postman et al. \(2012\)](#).

obey X-ray relaxation criteria, some of them show a somewhat ambiguous dynamical state. For 8 clusters out to 20 there is evidence of substructures in the X-ray surface brightness profiles. This may suggest that these 8 clusters are not completely dynamically relaxed. This is the case for Abell 209. In addition to these, other 5 clusters have been included in the survey due to their exceptional strength as gravitational lenses. They have been selected since they provide the highest potential for the discovery of very highly magnified ultra-high redshift galaxies. These clusters are not necessarily “relaxed”. In fact, at least two systems, MACSJ0717+3745 and MACSJ0416-2403, are merging systems. The CLASH clusters are selected to cover wide redshift ( $0.2 < z < 0.9$ ) and mass ( $5 - 30 \times 10^{14} M_{\odot}$ ) ranges.

Each CLASH cluster has been observed in 16 HST filters spanning 2.000 to 17.000 Å with WFC3/UVIS covering the near-ultraviolet, ACS the optical and WFC3/IR near-infrared spectrum. The exposure times are chosen primarily to achieve  $5\sigma$  limiting magnitude greater than 26 AB mag in each filter. Observations have been completed in 2013.

### 2.1.1 Supporting observations

All CLASH clusters have both X-ray and wide-field multi-band ground-based optical imaging. The X-ray imaging comes from Chandra/ACIS (Garmire, 2003). The ground-based optical images are available for 24 out of the 25 clusters, from the Subaru Observatory (and, in particular, performed with the SuprimeCam instrument Miyazaki et al. 1998). For 22 clusters, the images in at least three filters are available. Subaru multi-colour imaging is ideal for weak lensing studies, owing to its image quality, field of view and depth.

The CLASH cluster have also been observed in the mm-wave to map the Sunyaev-Zeldovich Effect (SZE). The SZE data come from the Bolocam instrument at the Caltech Submillimeter Observatory (Golwala et al., 2009) and Multiplexed SQUID/TES Array at Ninety Gigahertz (MUSTANG; Dicker et al., 2008) at the Robert C. Byrd Green Bank Telescope.

Infrared images are also available for most of the CLASH clusters from Spitzer Space Telescope (Werner et al., 2004), taken with the Infrared Array Camera (IRAC).

## 2.2 CLASH-VLT followup

Next to the CLASH HST panchromatic imaging project, and a number of multi-wavelength data covering a much larger area for each cluster, an ESO Large Programme (LP), hereafter CLASH-VLT, was approved to carry out an unprecedented spectroscopic campaign on the 14 southern CLASH clusters in the redshift range  $0.2 < z < 0.6$  with the VISIBLE Multi-Object Spectrograph (VIMOS) at the Very Large Telescope (VLT). The project was conceived to provide spectroscopic identification of large samples of cluster members and background lensed galaxies, such as giant arcs and multiple images. Specifically, the CLASH-VLT had 200 hours of multi-object spectroscopy with the following objectives:

1. Obtain spectroscopic confirmation of  $\sim 500$  cluster members in each cluster out to at least twice their virial radius. This goal was set, with the aid of kinematic data from cosmological simulations, to recover the dynamical mass profile with the same accuracy as the strong + weak lensing profiles.
2. Measure redshifts for over 200 lensed galaxies in the cluster cores, including several highly magnified galaxies out to  $z \sim 7$  (when Ly- $\alpha$  moves out of the VIMOS optical window). This provides confirmation of multiply imaged systems detected in the HST images and the angular diameter distances of lensed sources, which are crucial inputs for accurate strong lensing models. Additional targets include optical counterparts of Chandra X-ray sources in the cluster fields and host galaxies identified in the supernova programme, if they are bright enough.
3. Provide an unprecedented legacy dataset to investigate galaxy populations in a range of environments with the full set of multi-wavelength data.

At the time of writing the data acquisition is 95% complete.

The VIMOS low-resolution (LR) blue grism was primarily used in the CLASH-VLT program. When lensed sources with high photometric redshifts were present, the medium-resolution (MR) grism was selected instead. Eight to twelve VIMOS pointings were used for each cluster, spanning an area of 1520 square arcminutes, corresponding to 10 Mpc at the median redshift ( $\sim 0.4$ ) of the clusters, while keeping one quadrant locked onto the cluster core to increase the total exposure time on faint lensed sources. Additional key observations for this programme are archival

imaging data obtained with the Subaru Suprime-Cam for most clusters, with ESO Wide Field Imager (WFI) images for the southernmost target RXJ2248. Subaru multi-colour imaging is ideal for weak lensing studies, owing to its image quality, field of view and depth.

Subaru data have been also used for spectroscopic target selection, providing photometric catalogues for slit-mask design, after their coordinates are registered to the VIMOS pre-imaging astrometric system.

## 2.3 Spectroscopic dataset

Spectroscopic data are reduced with the VIMOS Interactive Pipeline and Graphical Interface (VIPGI) software (Scodeggio et al., 2005). Significant time had to be invested to recover the correct sky positions associated with each spectrum in an automated fashion, because the chances of misidentification with the standard VIPGI algorithm are not negligible in crowded cluster fields. To date, 75% of the data are fully reduced with measured redshifts and positions.

### 2.3.1 Spectroscopic members identification

Cluster membership for the galaxies with  $z$  has been established using different methods: the “Clean algorithm” for M1206 and the “Peak and Gap” method for A209. Below I will briefly describe these two methods.

#### Clean algorithm

This algorithm starts from a first guess of the cluster mass derived from a robust estimate of the cluster line-of-sight velocity dispersion  $\sigma_{los}$  via a scaling relation (for further details see Mamon et al., 2013, Appendix B). This mass guess is used to infer the concentration of the cluster mass profile, assumed to be NFW (Navarro et al., 1997a), from a theoretical mass concentration relation (Macciò et al., 2008). Given the mass and concentration of the cluster, and adopting the velocity anisotropy profile model of Mamon et al. (2010), a theoretical  $\sigma_{los}$ -profile is predicted and used to reject galaxies with rest-frame velocities outside  $\pm 2.7 \sigma_{los}(R)$  at any clustercentric distance  $R$ . The procedure is iterated until convergence. Biviano et al. (2013, see their appendix A) have shown that using the P+G method (see below) does not change the membership selection in a significant way.

### P+G method

This is a combination of the adaptive kernel method DEDICA (Pisani, 1993) and the “shifting gapper”, which uses both position and velocity information (Fadda et al., 1996). The first method identifies the main peak in the velocity distribution. Then, the P+G method considers galaxies into bins shifting along the distance from the cluster center and rejects those separated by more than a fixed value (typically  $800 \text{ km s}^{-1}$ ) from the central body of the velocity distribution. This method has the advantage of being independent of hypotheses about the dynamical status of the cluster

## 2.4 Photometric dataset

For the analyses presented in this thesis, photometric data from Subaru images for two clusters, M1206 and Abell 209, have been used. Details on the image data reduction can be found in Nonino et al. (2009).

### 2.4.1 Photometric catalogs

In this section, I will give brief summary on the catalog extraction process. The photometric catalogs were extracted using the software SExtractor (Bertin and Arnouts, 1996a) in conjunction with PSFEx (Bertin, 2011a, Annunziatella et al., 2013).

The catalogs are extracted in each of the 5 Subaru bands separately, then matched using STILTS (Taylor, 2006).

### Source extraction

Sources are detected in four steps: i) sky background modeling and subtraction, ii) image filtering, iii) thresholding and image segmentation, iv) merging and/or splitting of detections. Given the average size of the objects, in pixels, in our images, and in order to minimize the number of spurious detections, BACK.SIZE and BACK.FILTERSIZE are set to 256 and 4 respectively, for all fields and bands. To get accurate background values for the photometry, the background is also recomputed in an area centered around each considered object, setting BACKPHOTO.TYPE to LOCAL and the thickness of the background LOCAL annulus (BACKPHOTO.THICK) to 24. Once the sky background is subtracted, the image must be filtered. This

implies convolving the signal with a mask, shaped according to the characteristics that one wants to enhance in the image data. The filter that maximizes the completeness of the catalogs and minimizes the number of spurious objects is the Gaussian filter (with the size of the window depending on the seeing of the image). The detection process is mostly controlled by the thresholding parameters (DETECT\_THRESHOLD and ANALYSIS\_THRESHOLD). The choice of the threshold must be carefully considered. A too high threshold results in the loss of a high number of sources in the extracted catalogue, while a too low value leads to the detection of spurious objects. Hence, a compromise is needed by setting these parameters according to the image characteristics, the background rms, and also to the final scientific goal of the analysis. The catalogs have been extracted choosing to maximize the number of detected sources, while simultaneously keeping the number of spurious detections to a minimum. The final catalogs are visually inspected to avoid residual spurious detections and to verify the deblending parameters. Two or more very close objects can be detected as a unique connected region of pixels above threshold and, in order to correct for this effect, SExtractor adopts a deblending method based on a multi-thresholding process. Each extracted set of connected pixels is re-thresholded at  $N$  levels, linearly or exponentially spaced between the initial extraction threshold and the peak value. Also, here a compromise for the deblending parameter has to be found, since a too low value leads to a lack of separation between close sources, while a too high value leads to split extended faint sources (like spiral galaxies) in more components. Alternatively, it is possible to extract the catalog with a two-step approach by using different deblending and threshold parameters and to merge detections for extended sources or close pairs (e.g. [Rix et al., 2004](#); [Caldwell et al., 2008](#)). First, SExtractor is run in a so called cold mode tuned to properly detect and deblend the brightest and extended sources; then, in a second step, called “hot”, focused on the detection of faint ones. The two detections are then combined, by rejecting the faint sources whose position falls inside the cold source as determined by the Kron ellipse ([Kron 1980](#)).

### Aperture photometry and total magnitudes

Measurements of position, geometry, and photometric quantities are included in the final catalogs for all the detected and properly deblended sources. Among the photometric quantities calculated are: aperture magnitudes (MAG\_APER), measured in circular apertures of fixed diameters; isophotal magnitudes (MAG\_ISO), com-



puted by considering the threshold value as the lowest isophote and using two different elliptical apertures: the Kron (MAG\_AUTO, [Kron 1980](#)) and the Petrosian (MAG\_PETRO, Petrosian 1976) magnitudes, which are both estimated through an adaptive elliptical aperture. To describe the size of the sources we extract: the half flux radius, i.e. the FLUX\_RADIUS containing 50% of the total light and that containing 90% of the light. We also measured the PETRO\_RADIUS, defined as the point in the radial light profile at which the isophote at that radius is 20% of the average surface brightness within that radius, and the KRON\_RADIUS, which is the characteristic dimension of the ellipse used to calculate the KRON MAGNITUDE. The Kron and the Petrosian magnitudes are measured within elliptical apertures, whose semi-major and semi-minor axes are equal to A\_IMAGE and B\_IMAGE multiplied by the KRON\_RADIUS and PETRO\_RADIUS parameters, respectively. By using the PSFEx tool ([Bertin, 2011b](#)) it is possible to model the PSF of the images. Only non-saturated point sources with a SNR higher than 80 are considered. Spatial variations of the PSF are modelled with a third degree polynomial of the pixel coordinates. More details on the PSF modelling with the PSFEx tool can be found in [Bertin \(2011b\)](#); [Mohr et al. \(2012\)](#); [Bouy et al. \(2013\)](#). By using SExtractor combined with PSFEx, it is possible to obtain various estimates of the magnitude, in addition to those described above: (i) the PSF fitting (MAG\_PSF and the point source total magnitude MAG\_POINTSOURCE); (ii) the fit of a spheroidal component (MAG\_SPHEROID); (iii) the fit of a disc component (MAG\_DISK); and (iv) the sum of the bulge and the disc components, centered on the same position, convolved with the local PSF model (MAG\_MODEL). The model of the PSF is also helpful to get a more accurate star/galaxy classification.

### Star/Galaxy separation

The separation between extended and point-like sources is done by using a progressive approach analogous to that described in [Annunziatella et al. \(2013\)](#), using the following parameters provided by SExtractor: (i) the stellarity index (CLASS\_STAR); (ii) the half-light radius (FLUX\_RADIUS); (iii) the new SExtractor classifier SPREAD\_MODEL; (iv) the peak of the surface brightness above background ( $\mu_{max}$ ); (v) a final visual inspection for objects classified as galaxies but with borderline values of the stellarity index (CLASS\_STAR 0.9; see below). The stellarity index results from a supervised neural network that is trained to perform a star/galaxy classification. It assumes values between 0 and 1. In theory, SExtractor considers objects

with CLASS\_STAR equal to zero to be galaxies, and those with value equal to one as stars. In practice, stars are usually classified by selecting a CLASS\_STAR value above 0.9. This parameter performs reliable classification of bright sources. By using (FLUX\_RADIUS) as a measure of source concentration, we can extend the classification to fainter magnitudes. In order to be able to classify sources almost down to the completeness limit of the catalog a new SExtractor classifier can be used. This parameter, SPREAD\_MODEL, takes into account the difference between the model of the source and the model of the local PSF (Desai et al. 2012), to obtain a reliable star/galaxy classification for the faintest objects in our catalog. By construction, SPREAD\_MODEL is close to zero for point sources, positive for extended sources (galaxies), and negative for detections smaller than the PSF, such as cosmic rays. Finally, saturated stars can be selected by examining  $\mu_{max}$  as a function of the Kron magnitude. Since the  $R_C$  band is the deepest band of the survey, and the one conducted in the best seeing conditions, it is used for classification of sources in the cross-correlated catalogue of the four bands.

#### 2.4.2 Photometric members selection

Photometric redshifts ( $z_{phot}$ ) have been determined for all objects and in particular for those without the spectroscopic information. The  $z_{phot}$  have been obtained by a method based on neural networks. In particular, it was used the MultiLayer Perceptron (MLP, Rosenblatt 1957) with Quasi-Newton learning rule. The MLP architecture is one of the most typical feed-forward neural network model. The term feed-forward is used to identify basic behavior of such neural models, in which the impulse is propagated always in the same direction, e.g. from neuron input layer towards output layer, through one or more hidden layers (the network brain), by combining weighted sum of weights associated to all neurons (except the input layer). The MLP was used coupled with a particular learning rule, known as Quasi Newton Algorithm (QNA), i.e. the MLPQNA method (Brescia et al., 2013; Cavuoti et al., 2012). From a technical point of view, the MLPQNA differs from more traditional MLPs implementations in the way the optimal solution of the classification problem is found. This method has been applied to the whole data-set available for each cluster having a reliable  $BVR_CI_Cz$ -band magnitudes down to a magnitude limit of  $R_C = 25\ mag$  and  $R_C = 26\ mag$  for M1206 and A209, respectively, training the neural networks on the subsample of objects with spectroscopic redshifts. The spectroscopic sample was splitted in two subsets, using as the training set 80% of



the objects and as the validation set the remaining 20%. Using subsamples of objects with spectroscopically measured redshifts as training and validation sets makes the estimated  $z_{phot}$  insensitive to photometric systematic errors (due to zero points or aperture corrections). In this sense this method is more effective than classical methods based on Spectral Energy Distribution fitting (see Mercurio et al., in prep., for further details on our  $z_{phot}$  estimates). Cluster membership for the galaxies without  $z$ , but with  $z_{phot}$  has been obtained by investigation of the  $z_{phot}$  vs.  $z$  diagram, as described in [Biviano et al. \(2013\)](#). In this diagram, the sample of galaxies with spectroscopic redshifts is used to investigate the best strategy for the selection of members among the sample without spectroscopic redshift. In other words, the definition of cluster members with either the ‘Clean’ method or the ‘P+G’ method is used to define cuts in  $z_{phot}$  and in colors that maximize the inclusion of cluster members and minimize that of interlopers. The cuts in  $z_{phot}$  for membership selection have to be chosen to minimize the inclusion of foreground and background galaxies. On the other hand, trying to get rid of all foreground and background contamination would reject too many real members. In addition to the cuts in  $z_{phot}$ , in an effort to limit field contamination, one can also require colorcolor cuts, chosen by inspecting the location of the spectroscopic members in the colorcolor diagram.

### 2.4.3 Completeness and membership corrections

Unlike the spectroscopic selection of cluster members, the photometric selection is not secure. Two corrections need to be applied to the sample of cluster members. One takes into account the incompleteness of the sample with photometric redshift with respect to the photometric sample, since to obtain  $z_{phot}$ , we require that the galaxies have to be detected in all the five Subaru bands. The other takes into account possible discrepancies between  $z_{phot}$  and  $z_{spec}$  in the photometric selection of members, and we call it membership correction. In order to account for these corrections, we apply the following method.

The photometric completeness,  $C$ , is defined as the ratio between the number of galaxies with photometric redshift and the total number of galaxies in the  $R_C$  band. The completeness,  $C$ , has been evaluated for the whole sample and separately for red and blue galaxies, where the threshold value  $B - R_C = 1.5$  (calculated on the basis of aperture magnitudes within  $5''$ ) is used to discriminate between the two samples. This value for the color is chosen to match the limit in specific star formation rate (i.e., star formation rate per unit mass,  $sSFR \equiv SFR/M_*$ ) used to distinguish

between Passive and SF galaxies in our analysis (see Sect. 3.2 and 3.2).

To obtain the membership correction factor, we evaluate the completeness and the purity of the sample of galaxies classified as members based on their photometric redshift. We define the completeness as the ratio between the number of galaxies identified as members both spectroscopically and photometrically and the number of spectroscopic members  $C_M = N_{pm \cap zm} / N_{zm}$ . The purity is defined as the ratio between the number of photometric members that are confirmed also spectroscopically and the number of photometric members that have  $z_{spec}$ ,  $P = N_{pm \cap zm} / N_{pm \cap z}$ . The membership correction factor is defined as  $f_M \equiv P / C_M$ . The final correction factor we applied is given by the product  $f_C \cdot f_M$ .

## 2.5 Mass estimates - SED fitting technique

Fitting the spectral energy distributions (SEDs) of galaxies is a widely used technique that has matured significantly in the last decade. Model predictions and fitting procedures have improved significantly over this time, attempting to keep up with the vastly increased volume and quality of available data. Different physical processes occurring in galaxies all affect the shape of the spectrum, each dominating at different wavelengths. For example, ultraviolet, optical and near-infrared radiation from stars provides information on the past star formation history, chemical enrichment and attenuation by dust. Clues on the current star formation activity are provided by nebular emission lines produced by the gas heated by young stars. The mid- and far-infrared emission is related to the heating of dust grains in the interstellar medium (ISM) by stars of all ages. Detailed analysis of the SED of a galaxy can therefore, be used to obtain some constraints on stellar populations and ISM of galaxies. This, however, requires the consistent modelling of the emission by stars, gas and dust.

In this thesis, we use the SED fitting code MAGPHYS (da Cunha et al. 2008). This code compute the spectral evolution of stellar populations using the libraries of either Bruzual and Charlot (2003) or Bruzual & Charlot (2007), with a Chabrier (2003) stellar initial mass function and a metallicity value in the range  $0.02-2 Z_{\odot}$ . The difference between the two libraries of models is in the treatment of the thermally pulsating asymptotic giant branch stellar phase, which affects the NIR emission of stellar populations with an age of  $\sim 1$  Gyr. There is still considerable ongoing discussion

on the way to model this phase of stellar evolution (Maraston et al. 2006; Kriek et al. 2010). The attenuation of starlight by dust, is treated with the two-component model of Charlot and Fall (2000). With this model it is possible to compute the luminosity absorbed and re-emitted by dust in stellar birth clouds (i.e. giant molecular clouds) and in the ambient (i.e. diffuse) ISM in galaxies. Then, this luminosity is distributed across different wavelengths to compute infrared spectral energy distributions. The infrared emission from stellar birth clouds is described as the sum of three components: a component of polycyclic aromatic hydrocarbons (PAHs); a mid-infrared continuum which derives from the emission of hot grains at temperatures in the range 130 – 250 K; and a component of grains in thermal equilibrium with temperatures in the range 30 – 60 K. The relative contribution of these three components is fixed to reproduce the spectral shape of diffuse cirrus emission in the Milky Way. A component of cold grains in thermal equilibrium with temperatures in the range 15 – 25 K is also considered. The main parameter of this model is the total effective V-band absorption optical depth of the dust as seen by young stars inside birth clouds,  $\widehat{\tau}_V$ . This parameter is distributed according to a probability density function which is approximately uniform over the interval from 0 to 4 and drops exponentially to zero at  $\widehat{\tau}_V \sim 6$ . The spectral energy distribution is then obtained considering the history of the star formation rate (SFR) parametrized as a continuum model,  $SFR \propto e^{-\gamma t}$ , with superimposed random bursts. The timescale  $\gamma$  is distributed according to the probability density function  $p(\gamma) = 1 - \tanh(8\gamma - 6)$ , which is uniform between 0 and  $0.6 \text{ Gyr}^{-1}$  and drops exponentially to zero at  $1 \text{ Gyr}^{-1}$ . In this model, the age of the galaxy is a free parameter uniformly distributed over the interval from 0.1 to at most 13.5 Gyr. However, an upper limit for this value is provided by the age of the universe at the considered redshift.

With this model, MAGPHYS derives physical parameters such as star formation rate, stellar mass, dust content and dust properties, from combined ultraviolet, optical and infrared galaxy spectra, by applying a Bayesian approach.

In this thesis work, I used MAGPHYS (da Cunha et al. 2008) to derive stellar masses for all cluster member galaxies in M1206 and A209. I used both the Bruzual and Charlot (2003) and Bruzual & Charlot (2007) libraries and found no significant difference (on average) in the stellar mass estimates. Hence, for this thesis work I will refer to the masses obtained with Bruzual and Charlot (2003) models.

As an output of the SED fitting procedure, MAGPHYS provides both the parameters of the best-fit model and the marginalized probability distribution function (PDF) of each parameter. As the fiducial estimate of a given parameter, I adopted the median

value of the probability distribution, with lower and upper limits provided by the 16% and 84% percentiles of the same distribution. Using these limits, the typical  $1\sigma$  error on the  $M_\star$  estimates is  $\sim 0.15$  dex and  $\sim 0.07$  for galaxies at  $\bar{z} = 0.44$  and  $\bar{z} = 0.209$ .

An example of a SED fit is given in Fig. 2.2.

In order to check the reliability of the  $M_\star$  estimates, I used the data from the Ultra-

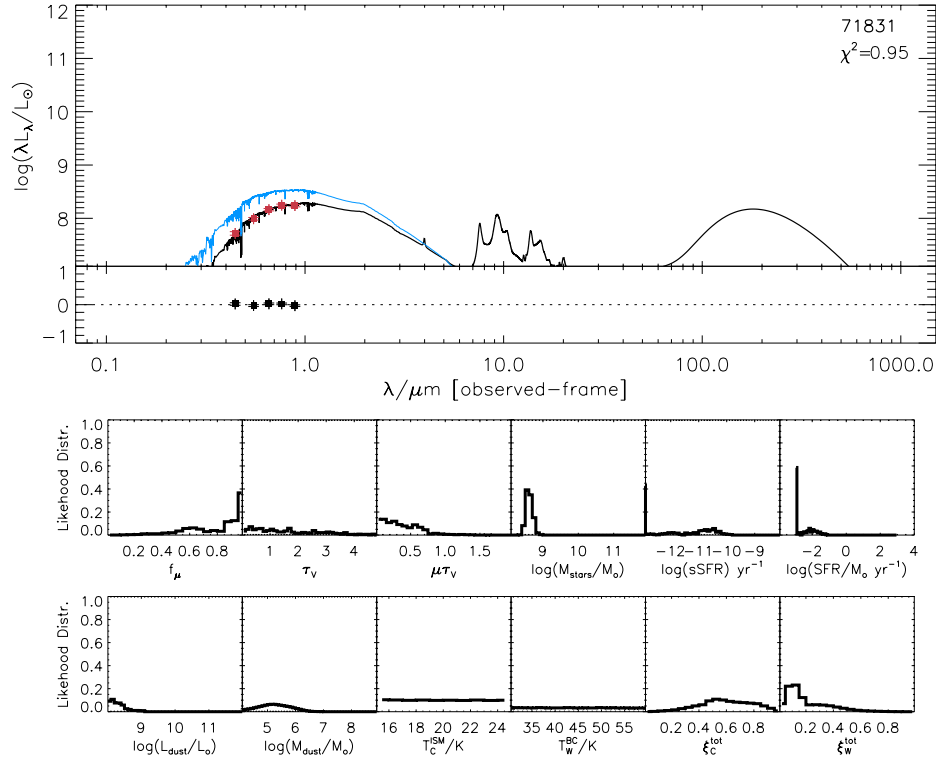


Figure 2.2. Example of a fit performed on a galaxy in the A209 cluster. The upper panel shows the attenuated and unattenuated SED, black and blue solid lines respectively. Red squares are the observed fluxes, while black squares represent the difference between the observed fluxes and those predicted by the models. Lower panels show the PDF distributions of the main parameters of the model.

Vista survey<sup>1</sup> (McCracken et al. 2013) which is an ultra-deep, near-infrared survey with the VISTA survey telescope of the European Southern Observatory. From the

<sup>1</sup><http://home.strw.leidenuniv.nl/~ultravista/>

UltraVista public catalog I selected only ‘USE = 1’ objects, i.e., objects classified as galaxies, with a K magnitude above the detection limit of 23.9, and with uncontaminated and accurate photometry (Muzzin et al. 2013b). I performed this test considering the sample at  $\bar{z} = 0.444$ , selecting only those galaxies with masses larger than the completeness limit of the sample at this redshift ( $10^{9.5} M_{\odot}$ , see Sect 3.2) and in the same photometric redshift range used for the cluster membership selection ( $0.38 \leq z_{phot} \leq 0.50$ , see Sect 3.2). UltraVista  $z_{phot}$  have been obtained with the EAZY code of Brammer et al. (2008). To separate the UltraVista sample into the passive and star-forming populations I used the separations provided by Muzzin et al. (2013a) in the UVJ diagram.

I compared the masses provided in the UltraVista data-base obtained using the FAST SED-fitting code of Kriek et al. (2009) with those obtained applying MAGPHYS on the UltraVista photometric catalog, using all of the available 30 bands, which cover the ultraviolet to mid-infrared,  $24 \mu m$ , spectral range. There was a good agreement between the two  $M_{\star}$  estimates, apart from a median shift  $\Delta M = \log(M/M_{\odot})_{MAGPHYS} - \log(M/M_{\odot})_{FAST} = -0.07$  independent from the galaxy type and mass. This comparison suggests that the  $M_{\star}$  estimates are not strongly dependent on the adopted SED-fitting algorithm, since the mass difference is well below the typical uncertainty in the individual  $M_{\star}$  estimates.

I also used the UltraVista dataset to check the effect of using only the optical bands in the SED fitting. In fact, for this thesis work I can use only the optical Subaru bands (BVR<sub>c</sub>Iz) over the whole cluster field both for M1206 and A209. Also in this case, I used the dataset related to the cluster M1206. For this test, I applied MAGPHYS to the selected UltraVISTA dataset once using all available bands, and another time using only the five optical Subaru bands. The  $M_{\star}$  estimates obtained using optical bands only are systematically higher than those obtained using all available bands, particularly for passive galaxies. The median value of the shift,  $\Delta M = \log(M/M_{\odot})_{all\ bands} - \log(M/M_{\odot})_{optical}$ , is -0.07 for star-forming galaxies and -0.23 for passive galaxies. The shift for the star-forming galaxies is small, well below the typical uncertainty in individual  $M_{\star}$  estimates. On the other hand, the shift in mass for the passive galaxies is not negligible.

The reason for the systematic shift in the  $M_{\star}$  estimates of passive galaxies is probably related to the fact that MAGPHYS, when run on its public library, tends to favor dusty star-forming models rather than passive modes, when they cannot be distinguished based on the available data.

I therefore run MAGPHYS again only on the sample of passive galaxies, this time us-

ing a library of templates heavily biased to fit old stellar populations with very little star formation (kindly provided by E. da Cunha). Using this library, the shift between the masses estimated using all UltraVISTA bands, and those estimated using only optical bands is reduced to  $-0.13$ . Since this is within the typical uncertainty in individual  $M_*$  estimates, the new mass estimates can be considered acceptable.

## 2.6 Structural parameters - Sérsic fit

To estimate the size of each cluster member down to the mass limit of the sample, I use the GALAPAGOS software. The main goal of GALAPAGOS is to obtain a Sérsic fit for all the sources detected in the image by SExtractor (Bertin and Arnouts, 1996b). The fits are performed by the GALFIT code (Peng et al. 2010a). Detailed explanations of how GALAPAGOS works is given in Barden et al. (2012). Here, I briefly describe only the steps that are crucial for this thesis work.

The main steps performed by GALAPAGOS are: i) detection of the sources by running SExtractor, ii) cut out of postage stamps for all detected objects, iii) estimate sky background and perform the Sérsic fit for all sources by running GALFIT.

The detection of the sources is performed by SExtractor in two-step runs: one so called “cold” tuned to properly detect and deblend only bright sources, and another called “hot”, focused on the detection of faint ones. The two detections are then combined, by rejecting the faint sources whose position falls inside the cold source as determined by the Kron ellipse (Kron 1980).

To reduce the computational time GALFIT needs to process an image, for each source in the original image GALAPAGOS creates a cut-out stamp. The extent of each postage stamp is determined by the size of the object as determined by SExtractor. The size of each stamp is given by the Kron radius estimated by SExtractor multiplied by an user defined scale factor. This factor has to be chosen to maximize the fitting area, to include as much flux of the central source and the closest neighbors as possible, and at the same time keep it to the minimum value, to speed up computation time of GALFIT. At this stage, GALAPAGOS also creates a sky map, a copy of the input images where the pixel values indicate the nature of the contained flux (either no flux, sky or source).

GALFIT performs the fit for every source in the catalogs, by using as input image the postage stamps previously created. The general light profile used for the fit of

each galaxy is the Sérsic model (see also Chapter 1.2).

$$\Sigma(R) = \Sigma_e \exp\{-\kappa[(R/R_e)^{1/n} - 1]\} \quad (2.1)$$

where  $R_e$  is the effective or half-light radius,  $\Sigma_e$  is the effective surface brightness,  $\Sigma(R)$  is the surface brightness as a function of radius  $R$ ,  $n$  is the Sérsic index and  $\kappa = \kappa(n)$  is a normalization constant. The starting parameters for the fits are the SExtractor estimate of source position ( $X\_IMAGE$ ,  $Y\_IMAGE$ ), the source total magnitude ( $MAG\_BEST$ ), its effective radius (function of  $FLUX\_RADIUS$ ), and its position angle ( $THETA\_IMAGE$ ). The output parameters from the fits and those obtained by SExtractor are then combined in a final catalog.





# MACS1206-0847

---

The results of this chapter are published in [Annunziatella et al. \(2014, A&A,571,A80\)](#).

## 3.1 Introduction

The distributions of galaxy luminosities and stellar masses ( $M_*$  hereafter), namely, the galaxy luminosity and stellar mass functions (SMF hereafter), are key observables for testing galaxy evolutionary models (e.g., [Macciò et al. 2010](#); [Menci et al. 2012](#)). The SMF allows for a more direct test of theoretical models than the luminosity function, since luminosities are more difficult to predict than  $M_*$  because of effects such as the age and metallicity of the stellar population, the dust content of the interstellar medium, etc. On the other hand, unlike luminosities,  $M_*$  are not direct observables, and can be determined only via multicolor and/or near infrared photometry. This explains why most studies of the galaxy SMF have been conducted only quite recently.

Hierarchical clustering models predict a mass distribution characterized by a cutoff mass  $M^*$  and well described by a power law at low masses ([Press and Schechter, 1974](#)). This result was then used by [Schechter \(1976\)](#) to derive an analytical expression of the luminosity function. This analytical expression is also used to describe the galaxy stellar mass function and is given in Eq. 3.1:

$$\Phi(\log M) = \ln(10) \Phi^* \left( \frac{M}{M^*} \right)^{1+\alpha} \exp \left( -\frac{M}{M^*} \right) d(\log M), \quad (3.1)$$

where  $\Phi^*$  is the normalization,  $\alpha$  is the low-mass end slope, and  $M^*$  corresponds to the exponential cutoff of the SMF at high masses.

Most determinations of the galaxy SMF (or of the near-infrared luminosity function, which is considered a proxy for the SMF) have been based on samples of field galaxies. The field galaxy SMF appears to have a flat slope down to  $10^9 M_\odot$ , up to  $z \sim 1$  (Fontana et al., 2006) and beyond (Stefanon and Marchesini, 2013; Sobral et al. 2014), although some authors provide evidence that the SMF steepens with  $z$  (Mortlock et al. 2011; Bielby et al. 2012; Huang et al. 2013). Ilbert et al. (2010) find that this steepening occurs at masses lower than a certain limit, which varies with  $z$ , and results from the combination of two single Schechter (1976) functions that characterize, separately, the red and blue SMF (Bolzonella et al. 2010; Ilbert et al. 2010; Pozzetti et al. 2010). The phenomenological model of Peng et al. (2010b), well described in Baldry et al. 2012) has interpreted the double Schechter function shape of the galaxy SMF in terms of ‘mass quenching’ and ‘environmental quenching’, which transform star-forming (SF) galaxies into passive. If a galaxy sSFR is independent of mass and the probability of ‘mass quenching’ is proportional to SFR, then the Schechter SMF of SF galaxies transforms into a steeper single Schechter SMF of passive (quenched) galaxies. Environmental quenching is supposed to be independent of mass, so it does not affect the overall shape of the SMF, but only its normalization, as SF (blue) galaxies are turned into passive (red) galaxies. The passive SMF appears as the combination of the single Schechter function originating from mass quenching and of another Schechter function originating from environmental quenching. This bimodality should be particularly apparent in high-density regions where the environmental quenching is most effective. Post-quenching mergers can then change the shape of the passive SMF by increasing the number of very massive galaxies relative to the less massive galaxies. This model makes specific predictions about the general evolution of the SMFs of SF and passive galaxies, which compare well with observations (Kauffmann et al., 2004; Bundy et al., 2005; Scoville et al., 2007; Drory and Alvarez, 2008; Scodeggio et al., 2009; Ilbert et al., 2010, 2013; Huang et al., 2013; Moustakas et al., 2013). The model also predicts the differential evolution of the relative number density of passive and SF galaxies in different environments, which is supported by observations (Bolzonella et al., 2010; Pozzetti et al., 2010). A consequence of the evolutionary model of Peng et al. (2010b) is that the SMF for passive galaxies should be environment dependent. Such a dependence is visible in a local sample of galaxies (based on SDSS data, Peng et al. 2010b), but not at higher redshift, apart from a slightly higher density of massive galaxies in denser regions (Bolzonella et al. 2010). That the predicted dependence is not observed at high redshifts could be because of the characteristics of the used samples, which are generally not complete at low-masses. To highlight possible environmental effects on the galaxy SMF one should compare the field galaxy SMF to that of cluster galaxies. Balogh et al. (2001) have found the SMF of non emission line galaxies to be steeper in clusters than in the field. On

the other hand, [Vulcani et al. \(2012, 2013\)](#) have found the field and cluster SMF not to be different, at least down to  $M_\star \sim 10^{10.2} M_\odot$ , not even when considering different galaxy populations separately. Their analysis is based on optical magnitudes and colors, while [Balogh et al. \(2001\)](#) use J-band magnitudes. Other studies of the near infrared luminosity functions of cluster and field galaxies found them to be statistically indistinguishable ([Lin and Mohr 2004](#); [Strazzullo et al. 2006](#); and [De Propriis and Christlein 2009](#)). [Giodini et al. \(2012\)](#) find no major difference between the SMF of field and group SF galaxies, at any redshift, and down to  $\sim 10^{8.5} M_\odot$ , except at the high-mass end, however, they do find significant differences in the SMF of passive galaxies in the field and low-mass groups, on one side, and in high-mass groups, on the other. Within clusters, there is no difference in the global SMFs evaluated within and outside the virial region ([Vulcani et al. 2013](#)), but [Calvi et al. \(2013\)](#) find the SMFs of different galaxy types change within different cluster environments. Different results might be caused by the different  $M_\star$  completeness limits reached by the different studies. [Merluzzi et al. \(2010\)](#) suggest that at low  $z$  the environmental dependence of the SMF becomes evident only for masses below  $\sim 10^9 M_\odot$ . At  $z \sim 1$  an environmental dependence of the SMF is already seen at the  $10^{10} M_\odot$  mass limit ([van der Burg et al., 2013](#)). This mass limit may in fact depend on redshift, as it corresponds to the mass below which the relative contribution of blue galaxies to the SMF becomes dominant [Davidzon et al. \(2013\)](#). In fact, red galaxies show a milder evolution with  $z$  than blue galaxies (at least for masses  $\geq 10^{11.4} M_\odot$  [Davidzon et al. 2013](#)) and they are more abundant in denser environments, at least until  $z \simeq 1.5$ . The SMF massive end, dominated by red galaxies, seems to be already in place at high  $z$  ([Kodama and Bower 2003](#); [Andreon 2013](#)) in clusters, and the characteristic magnitude of the near-infrared luminosity function of cluster galaxies evolves as predicted by models of passive stellar evolution ([Lin et al. 2006](#); [Strazzullo et al. 2006](#); [De Propriis et al. 2007](#); [Muzzin et al. 2007, 2008](#); [Capozzi et al. 2012](#); [Mancone et al. 2012](#)). [Mancone et al. \(2012\)](#) do not detect any evolution of the slope of the near-infrared luminosity function of clusters up to  $z \sim 1.5$ , but their result appears to contrast with the claimed evolution of the slope of the cluster SMF from  $z \sim 0$  to 0.5 by [Vulcani et al. \(2011\)](#). In this thesis, I studied the SMF of cluster galaxies and its dependence from the environment. In this Chapter, I will report the results obtained for the cluster at higher redshift MACS J1206.2-0847, discovered by [Ebeling et al. \(2009b, 2001a\)](#) at  $\bar{z} = 0.44$ . Passive and SF cluster members are considered separately, and the dependence of their SMFs on the local density and clustercentric radius is evaluated in a very wide radial range, 0 – 6 Mpc from the cluster center.

## 3.2 Main properties of M1206

M1206 was observed in 2012 as part of the CLASH-VLT followup (see Sect. 2.2) with VIMOS (Le Fèvre et al., 2003) at the ESO VLT, by using 12 masks (eight in low resolution and four in medium resolution), each with an exposure time of either 3 or  $4 \times 15$  minutes (10.7 hours in total). For this cluster, the spectroscopic dataset consisted in 3240 spectra, for which it has been quantified the reliability of the redshift determinations based on repeated measurements. For 2006 of the spectra, the estimated probability that they are correct is  $> 92\%$ , and for another 720 it is 75%. The remaining 514 lower quality redshifts are excluded from the dataset. Other 68 reliable redshifts from the literature (Lamareille et al., 2006; Jones et al., 2004; Ebeling et al., 2009a) and from IMACS-GISMO observations at the Magellan telescope (Dan Kelson, private communication) have been added to the sample. The final dataset contains 2749 objects with reliable redshift estimates, of which 2513 have  $z > 0$ . From repeated measurements, the estimated average error on the radial velocities is 75 (resp. 153)  $\text{km s}^{-1}$  for the spectra observed with the medium resolution (resp. low resolution) grism. The raw Suprime-Cam@Subaru data are retrieved from SMOKA<sup>1</sup> (Baba et al., 2002b) in the  $\text{BVR}_C I_C z'$  bands and processed as described in Umetsu et al. (2012). The aperture corrected magnitudes in each band have been obtained as explained in Sect. 2.4.2 and have been used to derive photometric redshifts,  $z_{\text{phot}}$ . This method is considered reliable down to  $R_c = 25.0$ . The RGB image of the cluster is shown in Fig. 3.1.

The main properties of this cluster are reported in Table 3.1.

Table 3.1. Main properties of the cluster MACS J1206.2-0847

Mean redshift	$0.43984 \pm 0.00015$
Velocity dispersion [ $\text{km s}^{-1}$ ]	$1087^{+53}_{-55}$
Virial radius $r_{200}$ [Mpc]	$1.96 \pm 0.11$
Virial mass $M_{200}$ [ $10^{15} M_{\odot}$ ]	$1.37 \pm 0.23$

Cluster membership for the galaxies with  $z$  has been established using the ‘Clean’ algorithm (see Sect. 2.3). Cluster membership for the galaxies without  $z$ , but with  $z_{\text{phot}}$  has been obtained by investigation of the  $z_{\text{phot}}$  vs.  $z$  diagram (shown in Fig. 3.2), as described in Sect. 2.4.2. As a compromise between these two extremes, of all galaxies without a spectroscopic redshift determination, only those with  $0.38 < z_{\text{phot}} < 0.50$  and within the following

<sup>1</sup><http://smoka.nao.ac.jp>



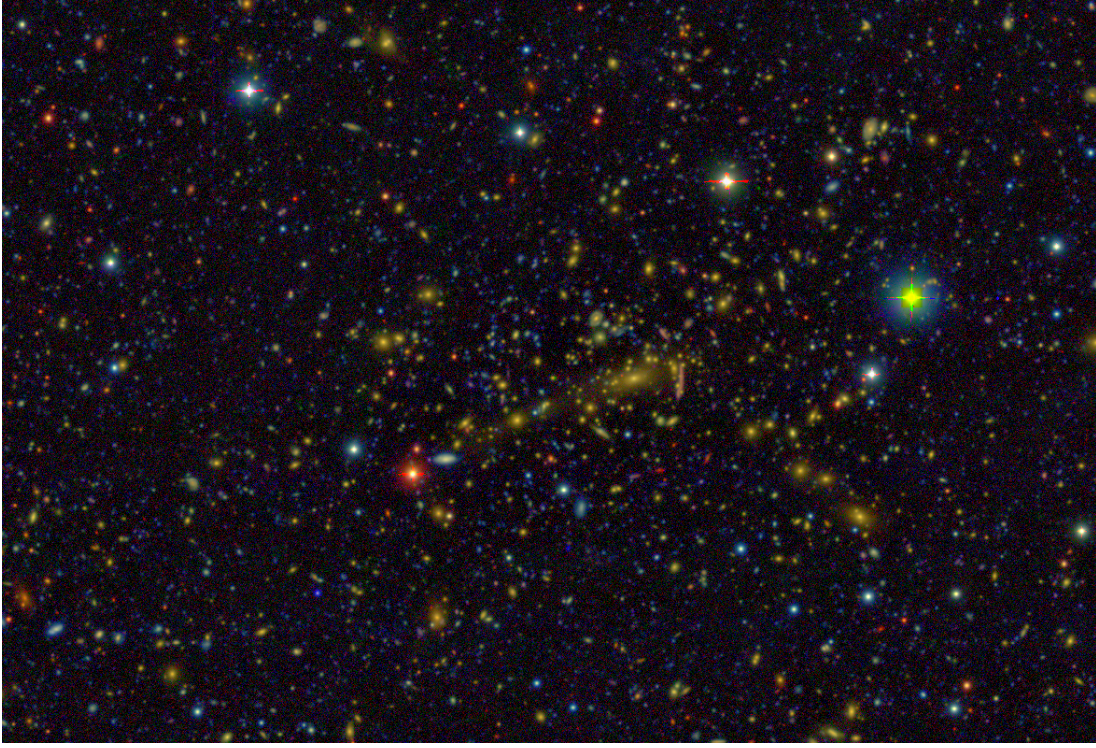


Figure 3.1. Color image of M1206 obtained by combining Subaru images in the  $R_C$ ,  $V$ ,  $B$  bands. The size of the image is  $\sim 6 \times 6$  arcmin, corresponding to  $\sim 2 \times 2$  Mpc at redshift 0.44.

$R_C - I_C$  vs.  $B - V$  color cuts are selected:

$$\begin{aligned} -0.09 + 0.52 (m_B - m_V) < m_R - m_I < 0.21 + 0.52 (m_B - m_V) \\ \text{for } 0.20 < m_B - m_V < 0.45, \end{aligned}$$

$$\begin{aligned} -0.09 + 0.52 (m_B - m_V) < m_R - m_I < 0.36 + 0.52 (m_B - m_V) \\ \text{for } 0.45 \leq m_B - m_V < 0.80, \end{aligned}$$

$$\begin{aligned} 0.01 + 0.52 (m_B - m_V) < m_R - m_I < 0.36 + 0.52 (m_B - m_V) \\ \text{for } 0.80 \leq m_B - m_V < 1.30. \end{aligned}$$

The final sample obtained by combining the samples of spectroscopically- and photometrically-selected members, contains 2468 members of which 590 are spectroscopically confirmed.

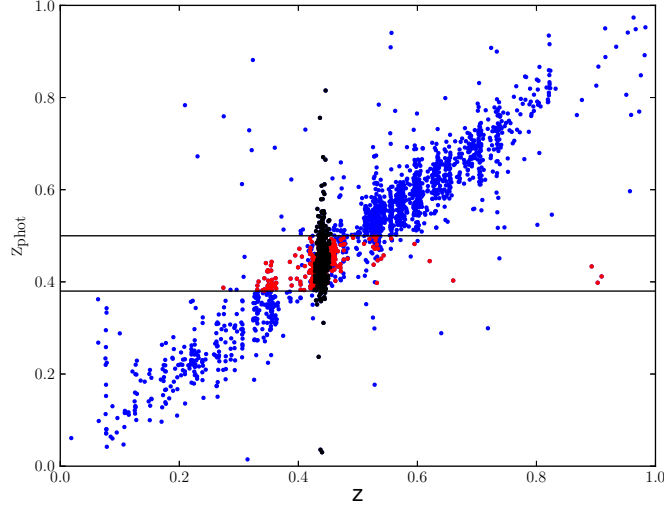


Figure 3.2. Photometric vs. spectroscopic redshifts for galaxies in the cluster field and in the magnitude range  $18 \leq R_C \leq 24$ . Black dots represent spectroscopically confirmed members. The two horizontal lines indicate the  $z_{phot}$  range chosen for membership selection of the galaxies without  $z$ . Within this range only galaxies with colors in the ranges defined above are selected as members. In this diagram these galaxies are indicated as red dots. Blue crosses are galaxies outside the spectroscopical and photometrical membership selections.

Stellar masses of cluster member galaxies have been obtained using the SED fitting technique performed by MAGPHYS. From the completeness limit in magnitude of the sample,  $R_C = 24$ , it is possible to derive the completeness limit in mass,  $10^{9.5} M_\odot$ , based on the relation between these two quantities shown in Fig. 3.3. The chosen completeness mass limit is that for the passive/red galaxies population, which guarantees that this sample is also complete for the population of SF/blue galaxies since they are intrinsically less massive than passive galaxies at a given magnitude. Down to this limiting  $M_\star$  there are 1363 cluster members, of which 462 are spectroscopically confirmed (i.e.,  $\sim 1/3$  of the total). In addition to  $M_\star$ , among all the parameters provided by the MAGPHYS procedure, the sSFR values are used to distinguish between SF and passive galaxies. Even if the sSFR estimates from optical SED fitting are not very accurate, they are sufficiently good to allow identification of the well-known bimodality in the galaxy distribution (see Sect. 1). This can be better appreciated by looking at the sSFR distribution of cluster galaxies, shown in Fig. 3.4. This distribution is clearly bimodal. Following [Lara-López et al. \(2010\)](#), and references therein) the sSFR value chosen to separate the populations of SF and passive galaxies is  $= 10^{-10} \text{ yr}^{-1}$ . This value

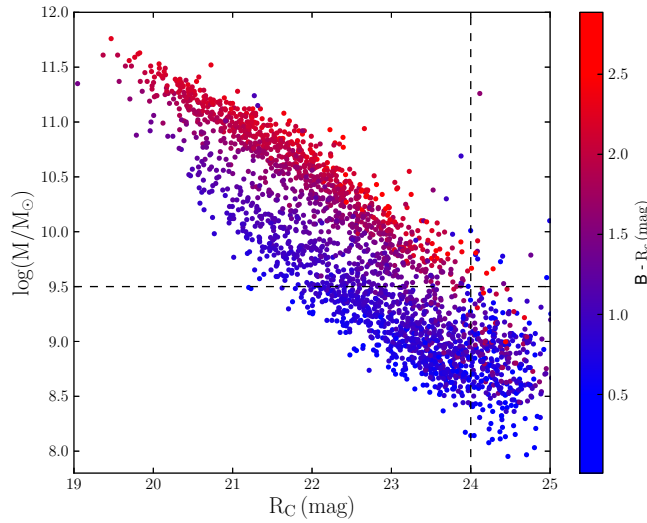


Figure 3.3. Galaxy stellar mass as function of  $R_C$  magnitude for cluster members. The points are color coded according to their  $B - R_C$  color. The vertical dashed line represents the completeness magnitude of this sample, and the horizontal dashed line represents the corresponding completeness mass.

also corresponds to a local minimum in the sSFR distribution. It is possible, however, that some truly passive galaxies are classified as dusty SF galaxies. To estimate how serious this misclassification might be, the sSFR distribution is fitted with two Gaussian functions (see Fig. 3.4). Misclassified passive galaxies are likely to lie in the high-sSFR tail of the Gaussian centered at low sSFR. The fraction of the area occupied by this Gaussian at  $\text{sSFR} > 10^{-10} \text{ yr}^{-1}$  is 0.5%, which corresponds to the fraction of passive galaxies misclassified as SF. Similarly, one can estimate that the fraction of SF galaxies incorrectly classified as passive is 4%. Given that these fractions are small, the sSFR estimates can be considered sufficiently good to separate the sample into the two populations of passive and SF galaxies. Even with the cuts in  $z_{\text{phot}}$  and color, the presence of interlopers is still evident from Fig. 3.2 (note the red dots with  $z$  very different from the cluster mean  $z$ ). The corrections that have to be applied to the sample of clusters members have been determined with the method described in Sect. 2.4.3. One is the correction for the incompleteness of the sample of galaxies with  $z_{\text{phot}}$ , which also contains all the galaxies in the spectroscopic sample.

Fig. 3.5 shows the completeness ( $C$ ), of the sample of galaxies with  $z_{\text{phot}}$ , in different magnitude bins, for red and blue galaxies separately, where a color selection ( $B - R_C = 1.5$ ) is applied to separate the two samples. This value corresponds to the sSFR value used to separate passive and SF members, and can therefore be used as a proxy for distinguishing

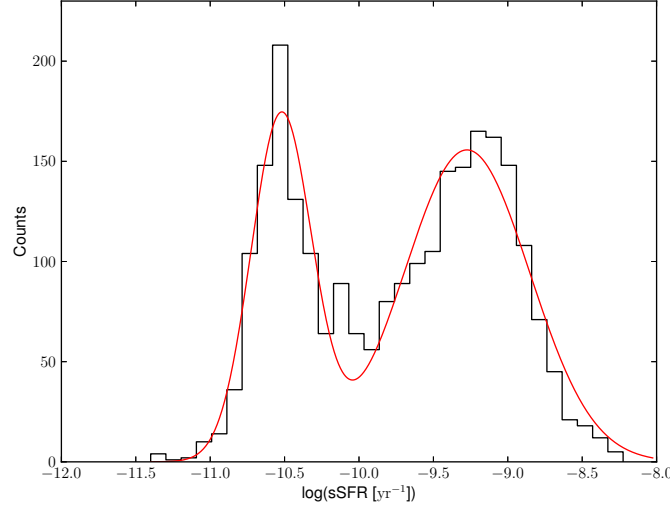


Figure 3.4. Distribution of the sSFR for the total sample of cluster galaxies. The red curve represents the best-fit to this distribution with two Gaussians.

these two populations when sSFR estimates are not available. In fact, sufficient photometric information is not available for all of the  $N_p$  galaxies to allow for a reliable sSFR estimate to be obtained from SED fitting. Completeness is  $> 90\%$  down to  $R_C = 23$ . In this magnitude range the variation of  $C$  with  $R_C$  is negligible and  $C$  is not significantly different for the red and blue samples. The constant value of  $C = 0.94$  is therefore adopted. In the magnitude range  $23 \leq R_C \leq 24$ , for blue galaxies the value of  $C$  remains unaltered, while for the red galaxies a magnitude-dependent correction is applied (using the values shown by the red dots in Fig. 3.5). Galaxies with  $R_C > 24$  are not considered in the analysis; The membership correction factor of the  $z_{phot}$  sample is shown in Fig. 3.6 as a function of mass and distance from the cluster center for red/passive and blue/SF galaxies, respectively. The large error-bars on blue galaxies, in particular at high masses, is related to the small number of objects in the last mass bins. There is no significant dependence of  $f_M$  from the galaxy  $M_*$  (see Fig. 3.6, left panel), but it does depend mildly on projected clustercentric distance,  $R$  (see Fig. 3.6, right panel). This dependence is similar for passive and SF galaxies, hence the same one evaluated for the passive sample is adopted also for the SF sample.



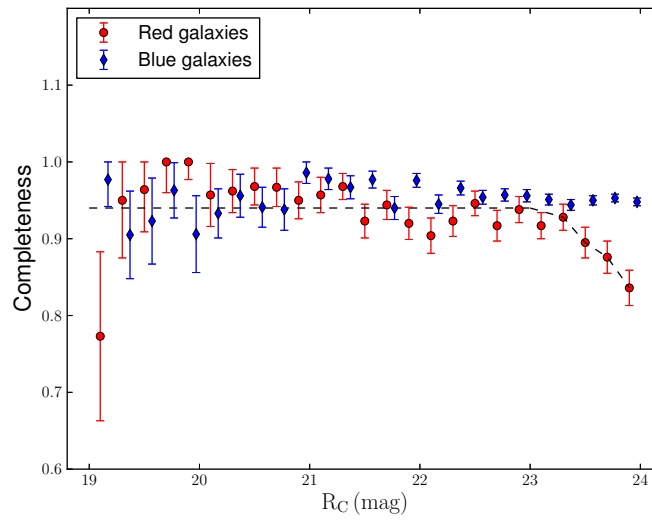


Figure 3.5. Completeness of the  $z_{phot}$  sample as a function of the  $R_C$  magnitude, separately for red ( $B - R_C \geq 1.5$ , red dots) and blue ( $B - R_C < 1.5$ , blue diamonds) galaxies. The dashed line represents the adopted completeness as a function of  $R_C$  for the sample of passive members, and, down to  $R_C = 23$ , for the sample of SF members also. For  $R_C > 23$ , the same completeness used for brighter SF members is adopted.

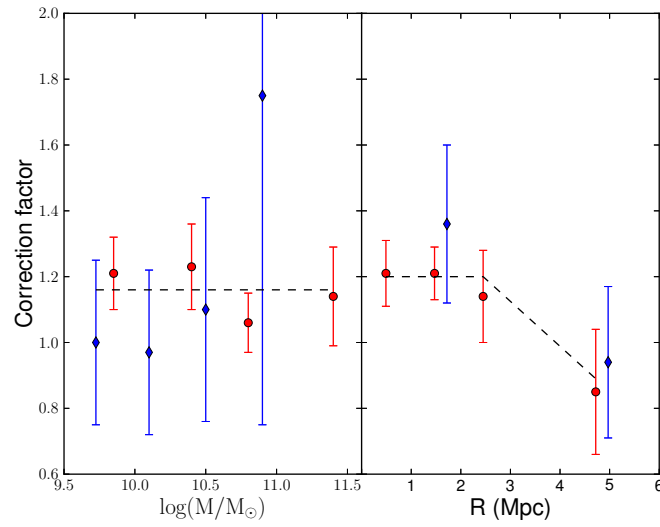


Figure 3.6. The membership correction factor  $f_M$  (see text) as a function of  $M_\star$  (left panel) and clustercentric radius  $R$  (right panel). The correction factor adopted is independent of  $M_\star$  and dependent on  $R$ . The same value is chosen for the samples of passive (red dots) and SF (blue diamonds) members.

### 3.3 The stellar mass function

The cluster SMF are obtained by counting the number of cluster members (defined in Sect. 3.2) per bin of  $M_*$ , and accounting for their weights (see Chapter. 2.4.3). The resulting  $M_*$  distribution is shown in Fig. 3.7 for all cluster members, and also, separately, for passive and SF cluster members. The errors on the galaxy counts are estimated with the bootstrap procedure (Efron and Tibshirani 1986). The SMFs are fitted with a [Schechter \(1976\)](#) function. The fits are performed down to the mass limit  $10^{9.5} M_\odot$ , using the maximum likelihood technique ([Malumuth and Kriss, 1986](#)). This technique has the advantage that no binning of the data is required. The normalization  $\Phi^*$  is not a free parameter, since it is constrained by the requirement that the integral of the fitting function over the mass range covered by observations equals the number of galaxies in the sample. Of course, this number must be corrected for completeness and membership contamination. Therefore, in the maximum likelihood fitting procedure, the product of the completeness and membership correction factors,  $f_C \cdot f_M$ , are used as weights for the individual values of  $M_*$ . Therefore, there are only two free parameters in the fit,  $\alpha$  and  $M^*$ , except when a double Schechter function is fitted to the data (in Sect. 3.3.1),

$$\Phi(\log M) = \ln(10) \Phi^* \times \left[ \left( \frac{M}{M^*} \right)^{1+\alpha} \exp \left( -\frac{M}{M^*} \right) + f_2 \left( \frac{M}{M_2^*} \right)^{1+\alpha_2} \exp \left( -\frac{M}{M_2^*} \right) \right] d(\log M). \quad (3.2)$$

In this case there are three additional free parameters,  $\alpha_2$  and  $M_2^*$ , and the ratio between the normalizations of the two Schechter functions,  $f_2 = \Phi_2^* / \Phi^*$ .

In the fits, in addition to the statistical errors, the errors on the stellar mass estimates have to be considered. These are evaluated by performing 100 Monte-Carlo simulations in which the mass of each galaxy is extracted randomly from a Gaussian distribution centered on the best-fit mass value, with a standard deviation equal to the error on the mass estimate. The errors on the stellar mass estimates provide only a minor contribution to the uncertainties on the best-fit Schechter function parameters, which are dominated by the statistical errors on the number counts.

The errors on the photometric completeness are not taken into account (see Fig. 3.5) since they are small. They would affect mostly the normalization of the SMF, while in most of the analyses I am only interested in comparing the shapes of different SMFs. The normalization of the SMF is only important when comparing the passive and SF samples (Sect. 3.3.1) and when comparing the SMF in the central cluster region to the mass in the intracluster light (ICL, see Sect. 3.5). Also, in these cases, the errors on the completeness can be neglected without a significant impact on the results.

The errors on the membership correction factor  $f_M$  (see Fig. 3.6) are significantly larger than those on the completeness. Their effect on the stellar mass function is estimated in the following way. First, different values of  $f_M$  are adopted for red (passive) and blue (SF) galaxies, given by their different means, rather than adopting the same value for both populations. Second, in the regions where  $f_M$  deviate from a constant, i.e., at  $R > r_{200}$ , the two extreme values of  $f_M$  given by  $f_M \pm \sigma_{f_M}$  are adopted, where  $\sigma_{f_M}$  is the error in the estimate of  $f_M$  at  $R > r_{200}$ . All the results of the analyses presented in the following sections do not change significantly when changing the membership correction factors as described above. Therefore, the uncertainties on  $f_M$  do not have a significant impact on the results. For the sake of clarity, the results presented in the following sections are based on the best estimates of  $f_M$ , i.e., those given in Sect. 3.2.

The statistical significance of the difference between any two SMFs can be assessed both parametrically, by comparing the best-fit parameters of the Schechter function, and non parametrically, via a Kolmogorov-Smirnov (K-S) test (e.g., Press et al. 1993). The K-S statistic quantifies a distance between the empirical distribution functions of two samples. The null distribution of this statistic is calculated under the null hypothesis that the samples are drawn from the same distribution. The two-sample K-S test is one of the most useful and general nonparametric methods for comparing two samples, as it is sensitive to differences in both location and shape of the empirical cumulative distribution functions of the two samples. For a meaningful comparison, to perform this test, a sample has to contain a minimum of ten objects. The K-S test compares the cumulative distributions and therefore it is only sensitive to differences in the shapes of the distributions, not in their normalizations. However, there are only two points in the analysis where the normalization of the SMF is important. One is in the comparison of the passive and SF populations (see Sect. 3.3.1), since different relative normalizations affect the mass value at which the two SMFs cross each other – a useful parameter to constrain theoretical models (see Sect. 3.5). Another point is the estimate of the mass that could have been stripped from galaxies and gone into the mass of the ICL (see Sect. 3.5). In other parts of the analysis, differences in the SMF normalization just reflect rather obvious dependencies of the number densities of galaxies (of different types) on the environments where they are located, e.g., the cluster is denser than the field by definition, and this over-density is higher among the population of passive galaxies by virtue of the well-known morphology-density relation (Dressler 1980). For the comparison of the SMFs of a given cluster galaxy population in different environments, the K-S test is particularly appropriate. For the same reason, to highlight differences in the SMFs, we only compare the shape parameters of the Schechter function best-fits,  $\alpha$  and  $M^*$ , and not the normalization parameter  $\Phi^*$ .

The parametric comparison naturally takes the completeness and membership corrections applied to the number counts into account. These corrections are also taken into ac-

Table 3.2. Best-fit Schechter function parameters

Galaxy type	$\Phi^*$	$\alpha$	$\log(M^*/M_\odot)$	$f_2$	$\alpha_2$	$\log(M_2^*/M_\odot)$
Passive	654	$-0.38 \pm 0.06$	$10.96 \pm 0.04$	–	–	–
SF	156	$-1.22 \pm 0.10$	$10.68 \pm 0.09$	–	–	–
All	751	$-0.39 \pm 0.18$	$10.94 \pm 0.16$	$0.65 \pm 0.20$	$-0.51 \pm 0.33$	$9.93 \pm 0.35$
All	541	$-0.85 \pm 0.04$	$11.09 \pm 0.04$	–	–	–

count in the K-S tests, since the correction factors are used as weights in the evaluation of the cumulative distributions whose maximum difference is used in the test to evaluate the statistical significance of the null hypothesis.

### 3.3.1 Different galaxy types

In Fig. 3.7, I show the SMFs of the passive, and separately, the SF galaxy populations along with their best-fitting Schechter functions<sup>2</sup>. The best-fit  $\alpha$  and  $M^*$  parameters and their  $1\sigma$  uncertainties are shown in Fig. 3.8 and listed in Table 3.2. When split into the two cluster populations of passive and SF galaxies, the SMF displays a strong, statistically significant dependence on galaxy type. In particular, the SMF of SF galaxies is increasing at the low-mass end, while the SMF of passive galaxies is decreasing. This difference is also confirmed by the K-S test, which gives a very low probability to the null hypothesis that the  $M_*$  distribution of SF and passive galaxies are drawn from the same population (see Table 3.4).

This type-dependence of the SMF is not only valid in general for the whole cluster, but also in different cluster regions, identified by their clustercentric distance or by their local galaxy number density in Sect. 3.3.2 and 3.3.2 (see Table 3.4).

In Fig. 3.7, it is also shown the sum of the two Schechter functions that describe the SMFs of passive and SF galaxies. A single Schechter function is also used to fit the SMF of all cluster galaxies together. The best-fit parameters are given in Table 3.2. According to the likelihood-ratio test (Meyer, 1975), the sum of the two Schechter functions provides a significantly better fit than the single Schechter function (with a probability of  $> 0.999$ ), after taking into account the difference in the number of free parameters (four vs. two).

The SMF of the whole galaxy population is also fitted with a double Schechter (eq. 3.2) and five free parameters, namely the  $\alpha$  and  $M^*$  of the two Schechter functions and their relative normalization. The best-fit parameters are listed in Table 3.2 along with their marginalized errors. The best-fit parameters of one of the two Schechter functions are very similar

<sup>2</sup>In this and the following figures, the data are binned only for the sake of displaying the results of the fits. No binning of the data is required in the fitting procedure.

to those of the Schechter function that provides the best-fit to the SMF of passive galaxies. On the other hand, the best-fit parameters of the other Schechter function are very different from those of the Schechter function that provides the best-fit to the SMF of SF galaxies. This means that while the best-fit with a double Schechter is optimal from a statistical point of view, it fails to correctly describe one of the two components of the cluster galaxy sample, that of SF galaxies. This is probably because of the fact that the sample of cluster galaxies is largely dominated by passive galaxies over most of the mass range covered by this analysis, and so it is difficult to correctly identify the minority component, that of SF galaxies. As a matter of fact, the uncertainties on the best-fit parameters of the double Schechter function are rather large.

Galaxy type	Environment	$\alpha$	$\log(M^*/M_\odot)$
SF	$R > r_{200}$	$-1.07 \pm 0.12$	$10.54 \pm 0.09$
SF	$R \leq r_{200}$	$-1.52 \pm 0.17$	$11.16 \pm 0.37$
Passive	$R > r_{200}$	$-0.43 \pm 0.09$	$10.99 \pm 0.05$
Passive	$R \leq r_{200}$	$-0.40 \pm 0.08$	$11.00 \pm 0.05$
Passive	Region 1	$-0.15 \pm 0.15$	$10.92 \pm 0.08$
Passive	Region 2	$-0.54 \pm 0.14$	$10.97 \pm 0.10$
Passive	Region 3	$-0.44 \pm 0.15$	$10.99 \pm 0.10$
Passive	Region 4	$-0.57 \pm 0.14$	$11.09 \pm 0.11$
Passive	Region (a)	$-0.13 \pm 0.16$	$10.93 \pm 0.08$
Passive	Region (b)	$-0.55 \pm 0.16$	$11.00 \pm 0.12$
Passive	Region (c)	$-0.41 \pm 0.11$	$10.95 \pm 0.07$
Passive	Region (d)	$-0.35 \pm 0.09$	$10.96 \pm 0.06$

Table 3.3. Best-fit Schechter function parameters for different environments

### 3.3.2 Different environments

To search for possible environmental dependences of the SMF, in this analysis I separated passive and SF galaxies, to disentangle possible type-specific environmental dependences of the SMF from the well-known environmental dependence of the galaxy population (Dressler 1980; Baldry et al. 2008 and references therein).

I considered two definitions of ‘environment’, one based on the distance from the cluster center, and another based on the local number density of cluster members. Of course, these definitions are not entirely independent, given the correlation between local density and radial distance (e.g. [Whitmore et al., 1993](#)). Using these two definitions nine cluster regions are defined, five at different distances from the cluster center, (four within  $r_{200}$ , labeled 1 to 4, and another one at  $R > r_{200}$ , see Sect. 3.3.2) and another four at different local densities (labeled (a) to (d), see Sect. 3.3.2).

The former of the two definitions environment assumes circular symmetry, but the cluster is significantly elongated in the plane of the sky ([Umetsu et al., 2012](#)). However, this assumption is dropped in the other definition of environment, as the regions (a) to (c) are elongated in the direction traced by the galaxy distribution (see Fig. 3.12), which is similar to the elongation direction of the brightest cluster galaxy (BCG) and of the total mass of the cluster as inferred from a weak lensing analysis by [Umetsu et al. \(2012, see their Figs. 1 and 11\)](#). As shown below, the results obtained in the analysis are essentially independent on the adopted definition of environment, hence the assumption of circular symmetry does not seem to be critical.

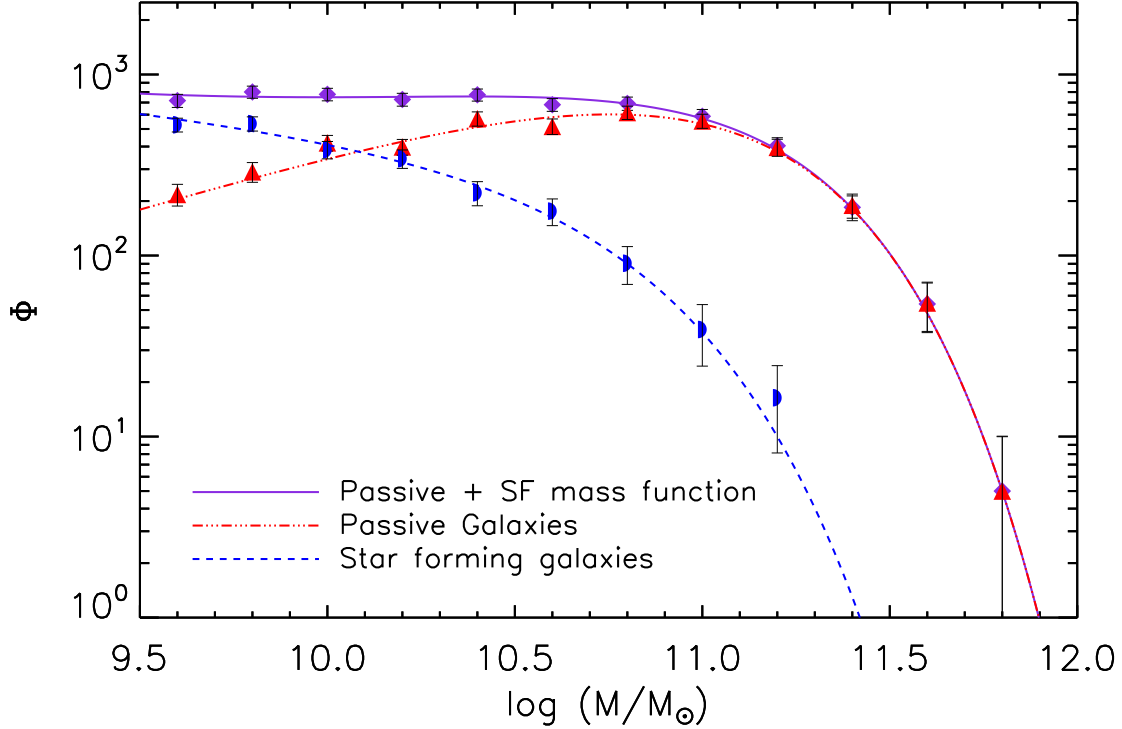


Figure 3.7. SMF for passive and SF cluster members (red triangles and blue half-circles, respectively) and their best-fit Schechter functions (red triple-dot-dashed and blue dashed lines). The sum of the two SMFs is shown as a solid violet line. Violet diamonds are the counts obtained by considering all cluster members. The points represent counts in bins of 0.2 dex in  $M_\star$  divided for the bin size, and the counts have been corrected for completeness and membership. The ( $1\sigma$ ) errors on the counts have been estimated via the bootstrap resampling procedure.



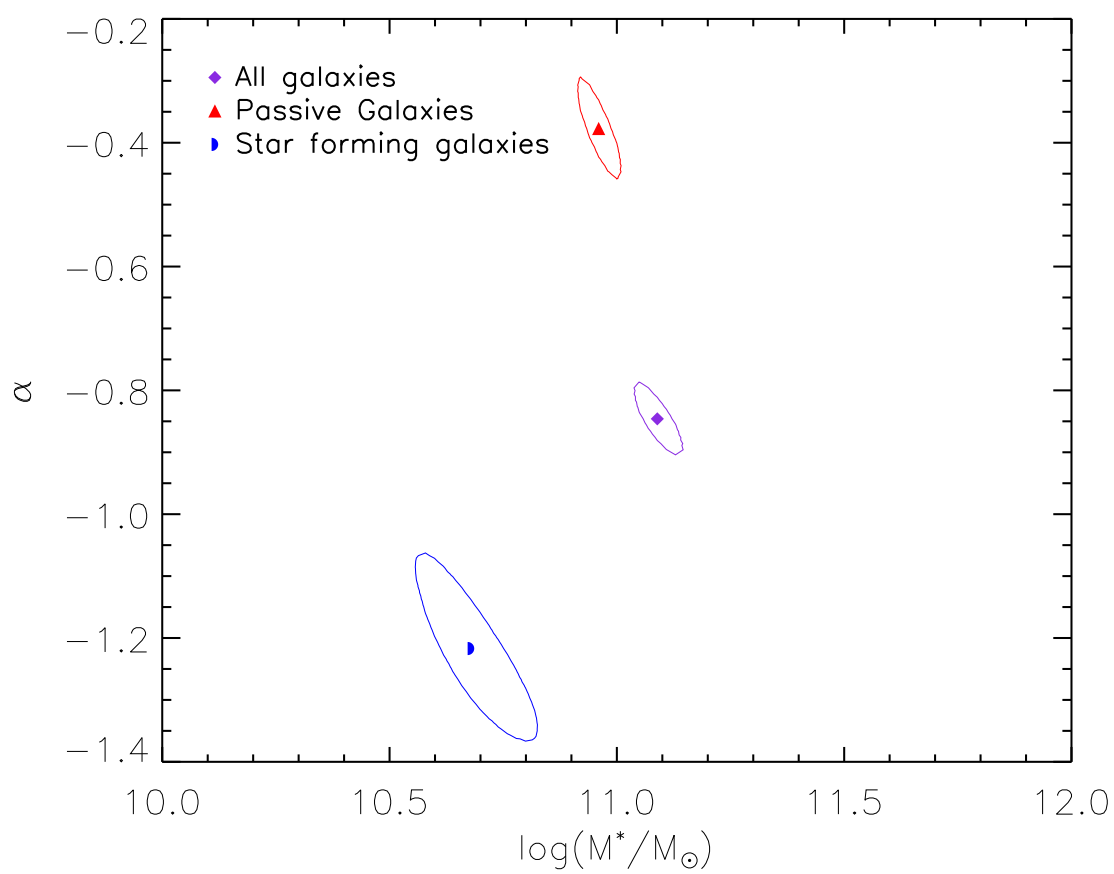


Figure 3.8. Best-fit Schechter parameters  $M^*$  and  $\alpha$  and  $1\sigma$  likelihood contours.

Table 3.4. Results of the K-S tests

Compared samples	N1, N2	Prob. (%)
Type dependence		
Passive vs. SF in the cluster	846, 517	< 0.01
Passive vs. SF in Region 2	120, 21	< 0.01
Passive vs. SF in Region 3	120, 31	< 0.01
Passive vs. SF in Region 4	102, 20	< 0.01
Passive vs. SF in Region (b)	96, 33	0.4
Passive vs. SF in Region (c)	199, 54	< 0.01
Passive vs. SF in Region (d)	328, 420	< 0.01
Environment dependence - SF galaxies		
SF within and outside $r_{200}$	78, 439	> 10
SF in Regions 2 and 3	31, 31	> 10
SF in Regions 3 and 4	31, 20	> 10
SF in Regions (b) and (c)	33, 54	> 10
SF in Regions (c) and (d)	54, 422	> 10
Environment dependence - passive galaxies		
Passive within and outside $r_{200}$	438, 408	> 10
Passive in Regions 1 and 2	120, 120	0.8
Passive in Regions 2 and 3	120, 102	> 10
Passive in Regions 3 and 4	102, 96	> 10
Passive in Regions (a) and (b)	100, 83	0.4
Passive in Regions (b) and (c)	83, 199	> 10
Passive in Regions (c) and (d)	199, 328	2

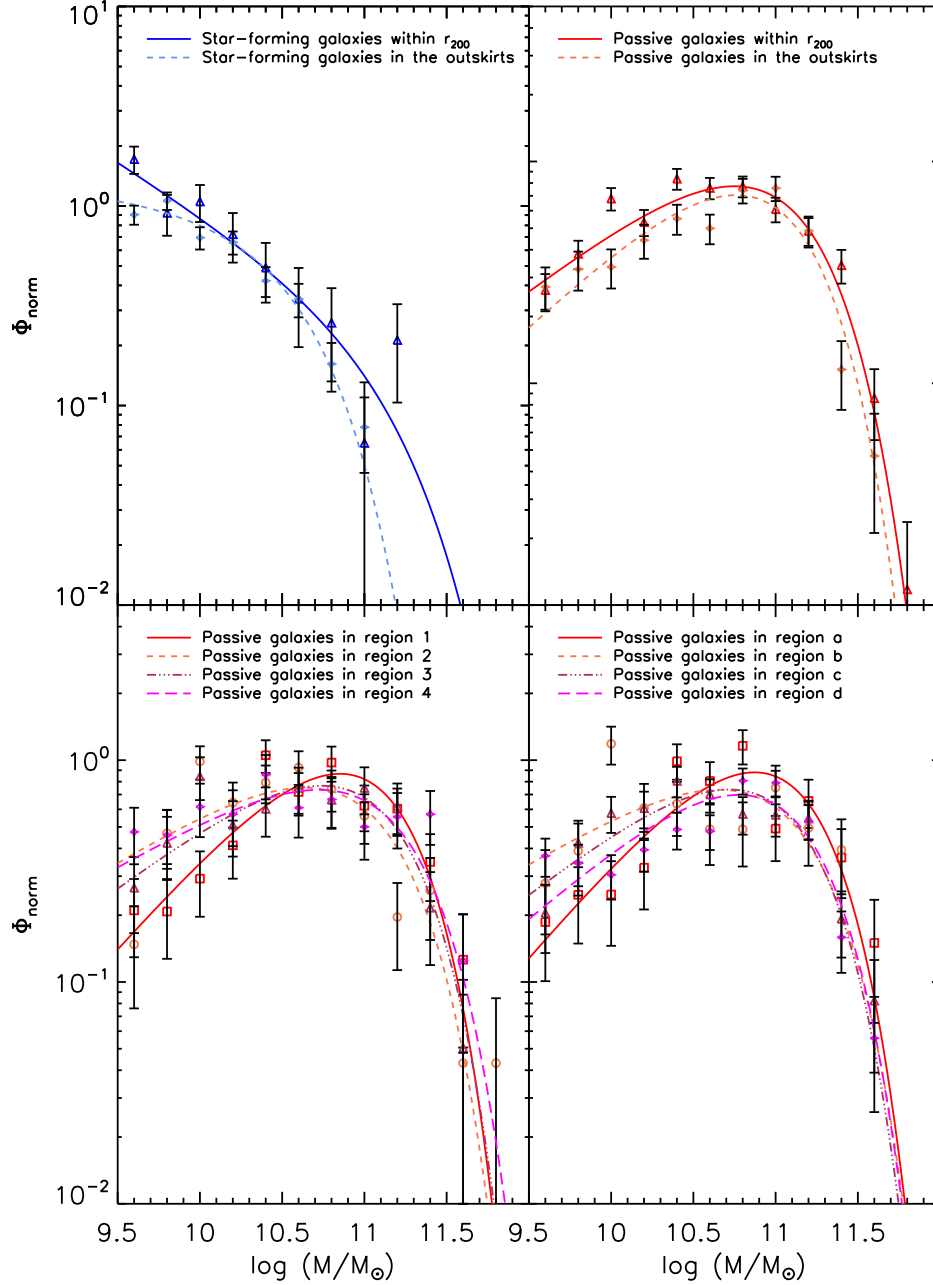


Figure 3.9. SMFs of SF and passive galaxies in different cluster regions and in the field. Upper left (resp. right) panel: SMFs of SF (resp. passive) cluster galaxies beyond and within  $r_{200}$ . Bottom left panel: SMFs of passive cluster galaxies in four different regions, defined by their distances from the cluster center (see text). Bottom right panel: SMFs of passive cluster galaxies in four different regions, defined by their local number densities. SMFs are normalized to the total number of galaxies contained in the respective samples.

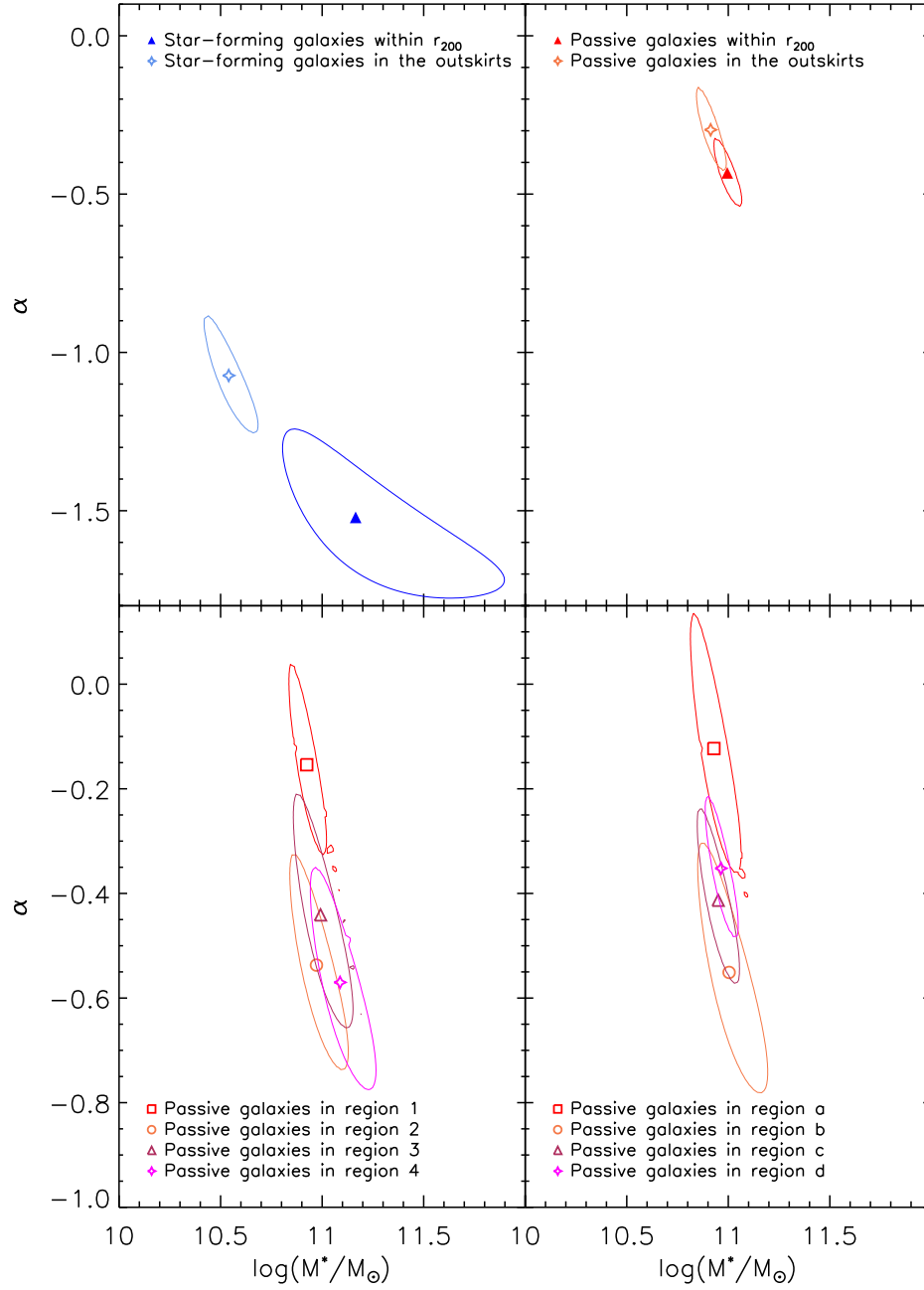


Figure 3.10. Best-fit Schechter parameters  $M^*$  and  $\alpha$  and  $1\sigma$  likelihood contours for the SMFs of SF and passive galaxies in different cluster regions and in the field. The panels correspond one-to-one to those of Fig. 3.9.

### Clustercentric radial dependence

The first definition of ‘environment’ considered in this analysis refers to the clustercentric distance. The cluster center is identified with the position of the BCG (see Table 3.1 and Biviano et al., 2013).

The first comparison is made between SMFs of passive and, separately, the SF cluster members, within and outside the virial radius,  $r_{200}$ .

These are shown in Fig. 3.9 (upper panels), and their best-fit Schechter function parameters are listed in Table 3.3 and shown in Fig. 3.10 (upper panels). The SMFs of cluster members within and outside the virial radius are not significantly different, neither for the passive nor for the SF galaxies. This is confirmed by the K-S test (see Table 3.4).

The SMF is then determined in four different regions within  $r_{200}$ , namely:

1.  $R/r_{200} \leq 0.25$ .
2.  $0.25 < R/r_{200} \leq 0.5$ .
3.  $0.5 < R/r_{200} \leq 0.75$ .
4.  $0.75 < R/r_{200} \leq 1$ .

The number of SF galaxies is not large enough to allow for Schechter function fits in all these regions and, in some cases, there are not enough galaxies in the subsamples to allow for K-S test comparisons of the  $M_*$  distributions. On the other hand, there is always a sufficiently large number of passive galaxies to allow for meaningful Schechter function fits in all the four regions. The SMFs for the passive galaxies in the four different regions are shown in Fig. 3.9 (bottom left panel), along with their best-fitting Schechter functions. The best-fit parameters are listed in Table 3.3 and shown in Fig. 3.10 (bottom left panel).

To highlight a possible radial dependence of the cluster SMF we compare the  $M_*$  distributions of cluster members in adjacent regions, using the K-S test, separately for SF and passive galaxies, whenever there are at least ten galaxies in each of the subsamples. The  $M_*$  distributions of the SF cluster galaxies in the different regions are not statistically different (see Table 3.4). On the other hand, the K-S tests indicate a significant difference of the  $M_*$  distributions of passive cluster members in Region 1 (the innermost one) and the adjacent Region 2. For no other adjacent regions does the K-S test highlight a significant difference from the SMFs of passive galaxies.

From Fig. 3.10 (bottom left panel) and Table 3.3 one can see that the difference of the SMFs in Regions 1 and 2 is reflected in a difference in the values of the best-fit Schechter parameter  $\alpha$ . Fig. 3.9 (bottom left panel) shows indeed a low-mass end drop in the SMF of passive galaxies in Region 1 more rapid than in the SMFs in other Regions.

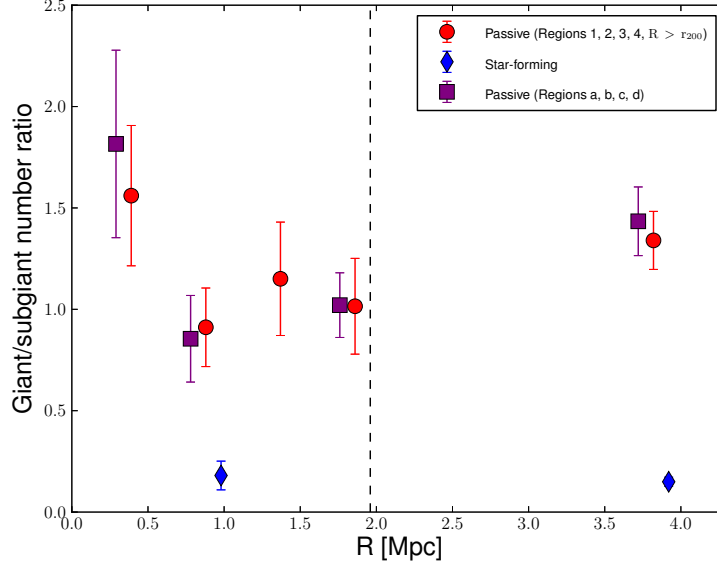


Figure 3.11. The number ratio of giant galaxies ( $\log M_*/M_\odot \geq 10.5$ ) and subgiant galaxies ( $\log M_*/M_\odot < 10.5$ ), GSNR, for different samples of passive galaxies (red dots: Regions 1–4 and  $R > r_{200}$ ; magenta squares: Regions (a)–(d)) and SF galaxies (blue diamonds: within and outside the virial radius). For Regions (a)–(d) the point abscissae are set at the average clustercentric radii of the galaxies in the subsamples selected on the base of local density. The vertical dashed line indicates the location of  $r_{200}$ .

From Fig. 3.10, one can notice that the SMFs of passive galaxies in Region 1 intersects those of passive galaxies in the other regions at  $\log(M_*/M_\odot) \sim 10.5$ . Since these SMFs are normalized by the total number of galaxies in their respective samples, this does not mean that in Region 1 there are more galaxies with  $\log(M_*/M_\odot) \sim 10.5$  than in other regions. This mass value only indicates where the relative ratio of the number of galaxies more massive and less massive than a given value is maximally different for the SMF in Region 1 and in the other regions. Therefore, this value is used to separate ‘giant’ from ‘subgiant’ galaxies and plot the giant/subgiant number ratio (GSNR hereafter) as a function of radial distance from the cluster center in Fig. 3.11. Note that the correction factors defined in Sect. 2.4.3 are used as weights to compute the GSNR. The GSNR of passive galaxies decreases rapidly from the center (Region 1) to  $R \sim 0.8$  Mpc, then gently increases again toward the cluster outskirts ( $R > 3.5$  Mpc) but without reaching the central value again. The GSNR of SF galaxies does

not seem to depend on radius and is systematically below that of passive galaxies at all radii.

### Density dependence

An alternative definition of ‘environment’ considered in this analysis is the local number density of cluster members. This density is defined by smoothing the projected distribution of galaxies with a two-dimensional Gaussian filter in an iterative way. Initial estimates of the densities are obtained by using a fixed ‘optimal’ (in the sense of [Silverman 1986](#)) characteristic width for the Gaussian filter. In the second iteration, the characteristic width of the Gaussian filter is locally modified by inversely scaling the ‘optimal’ width with the square root of the initial density estimates. In other words, an adaptive-kernel filtering of the galaxy spatial distribution is adopted, where the kernel is adapted in such a way as to be narrower where the density is higher.

The distribution of cluster members is shown in Fig. 3.12, where symbols are colored according to the local galaxy density.

Four regions of different mean projected galaxy density  $\Sigma$  (in units of  $\text{arcmin}^{-2}$ ) are identified:

- (a)  $\Sigma > 12.5$ .
- (b)  $5 < \Sigma \leq 12.5$ .
- (c)  $2.5 < \Sigma \leq 5$ .
- (d)  $\Sigma \leq 2.5$ .

From Fig. 3.12 one can note that Regions (a) and (b) approximately correspond to Regions 1 and 2 (defined in Sect. 3.3.2), while Region (c) corresponds roughly to Regions 3 and 4 with an extension beyond the virial radius. One obvious difference is that the regions defined by the value of  $\Sigma$  are more elongated than those defined by radius.

Since there are not enough SF galaxies to allow for meaningful Schechter fits to be performed in Regions (a) to (d), in Fig. 3.9 (bottom right panel) only the passive galaxy SMFs and their Schechter best fits are shown. The best-fit parameters are listed in Table 3.3 and shown in Fig. 3.10 (bottom right panel).

The K-S tests indicate that the SMF of SF galaxies is independent of local density (see Table 3.4). On the contrary, the SMF of passive galaxies does depend on local density. In fact, the K-S tests performed between  $M_*$  distributions in adjacent regions indicate a significant difference between Regions (a) and (b) (see Table 3.4). This difference is caused by the more rapid drop at the low-mass end of the SMF in Region (a) compared to the SMFs of other regions (Fig. 3.10, bottom right panel) and is reflected in a different value of the best-fitting parameter  $\alpha$  (see Table 3.3).

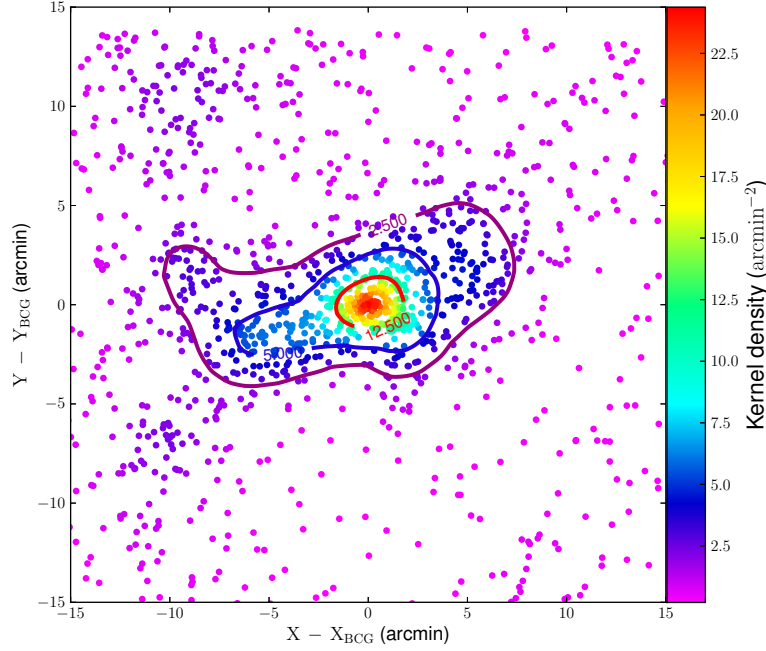


Figure 3.12. Spatial distribution of cluster members. The local number density is color coded as indicated by the bar at the right side of the plot. Coordinates are in arcmin with respect to the position of the BCG, see Table 3.1. Galaxies belonging to Regions (a), (b), (c), which are defined in Sect. 3.3.2, are those inside the red, blue, and purple solid lines, respectively. Galaxies belonging to Region (d) are the outer points.

In Fig. 3.11, it is evident that the radial trend of the GSNR of passive galaxies found in regions 1–4 is confirmed when considering regions (a)–(d).

### 3.4 The stellar mass density profile

The sample of 1363 cluster members with  $M_{\star} \geq 10^{9.5} M_{\odot}$  are used to determine the radial profiles of number and stellar mass density of this cluster,  $N(R)$  and  $\Sigma_{\star}(R)$ , respectively. These profiles are fitted in the region  $0.05 < R/r_{200} \leq 1$  (i.e., excluding the BCG) with a projected NFW (pNFW) model (Navarro et al., 1997a; Bartelmann, 1996) using a weighted maximum likelihood fitting technique. For the determination of  $N(R)$ , the same weights already used for the construction of the SMF, i.e., the product  $f_C \cdot f_M$  (see Sect. 2.4.3) are



applied. For the determination of  $\Sigma_*(R)$ , the weights used for the determination of  $N(R)$  are multiplied by the galaxy stellar masses,  $f_C \cdot f_M \cdot M_*$ . In Table 3.5, the values of the scale radii,  $r_s$ , of the best-fit models are listed. Note that the best-fit value for the  $r_s$  of  $N(R)$  is consistent with that estimated by (Biviano et al., 2013) on a slightly different sample.  $\Sigma_*(R)$  is significantly more concentrated than  $N(R)$ .

The two profiles and their best-fit models are shown in Fig. 3.13. The error bars in the figure have been estimated via a bootstrap procedure. The pNFW model provides a good fit to the number density profile (reduced  $\chi^2 = 1.4$ ), and a slightly worse fit to the stellar mass density profile (reduced  $\chi^2 = 2.2$ ).

Table 3.5. The NFW scale radii of the density profiles

Profile	$r_s$ (Mpc)
Galaxy number density	$0.80^{+0.05}_{-0.14}$
Stellar mass density	$0.52^{+0.06}_{-0.07}$
Total mass density	$0.34^{+0.06}_{-0.06}$

The two density profiles are deprojected using the Abel inversion, which assumes spherical symmetry (e.g. Binney and Tremaine, 1987). Before performing the numerical inversion, I smooth  $N(R)$  and  $\Sigma_*(R)$  with the LOWESS technique (e.g. Gebhardt et al., 1994). The needed extrapolation to infinity is done as in Biviano et al. (2013, eq. 10), by approximating infinity with  $R_\infty = 30$  Mpc and by checking that increasing this radius to larger values does not affect the result of the integral. I extrapolate the LOWESS smoothing of  $N(R)$  beyond the last observed radius,  $R_l$ , with the following function:

$$N(R) = \eta (R_\infty - R)^\zeta / R^\zeta, \quad (3.3)$$

with

$$\begin{aligned} \zeta &= [d \log n / d \log R]_{R_l} - \zeta R_l / (R_\infty - R_l), \\ \eta &= N(R_l) R_l^\zeta / (R_\infty - R_l)^\zeta. \end{aligned}$$

The only free parameter in the extrapolating function is the  $\zeta$  parameter. The deprojected stellar mass-to-number density profile ratio,  $\rho_*(r)/n(r)$ , is shown in the top panel of Fig. 3.14. The dashed lines represent  $1 \sigma$  confidence levels obtained by propagation of errors, where the fractional errors on the individual deprojected profiles are assumed to be those estimated

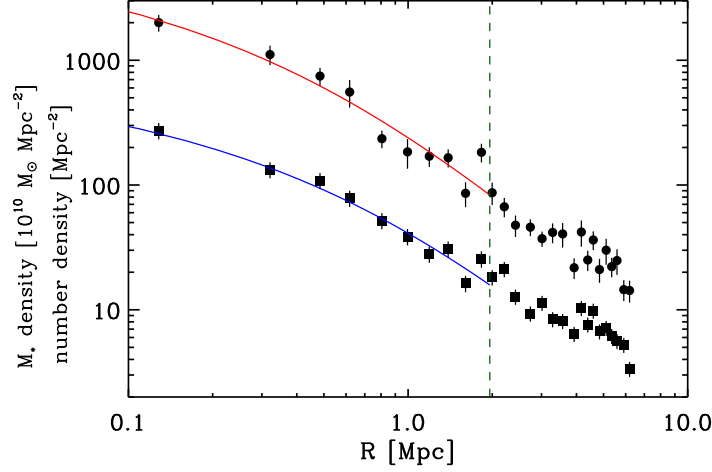


Figure 3.13. The stellar mass density profile (dots) and the number density profile (squares) and their best-fit projected NFW models (red and blue curves). The  $1\sigma$  errors are shown, and evaluated using a bootstrap procedure. Both densities are space densities. The vertical dashed green line indicates the location of  $r_{200}$ .

for the projected profiles (Fig. 3.13). The ratio  $\rho_*/n$  decreases by  $\sim 30\%$  from the center to  $r_{200}$ .

Both the relative concentration of the best-fit pNFW models of the two projected profiles and the ratio of the two deprojected profiles, indicate a mass segregation effect, i.e., galaxies are on average more massive (in stars) near the cluster center than at the cluster periphery. This is consistent with the trend in the GSNR which is higher in the central cluster region (see Fig. 3.11).

The total mass density profile,  $\rho_{tot}$ , is taken from the gravitational lensing analysis of [Umetsu et al. \(2012\)](#). Specifically, I consider their NFW best-fit model parametrization of this profile. The ratios  $\rho_{tot}/n$  and  $\rho_*/\rho_{tot}$  as a function of the 3D distance from the cluster center,  $r$ , are shown in the middle and bottom panels of Fig. 3.14. The distribution of total mass is more concentrated than both the distribution of galaxies (see also [Biviano et al., 2013](#)) and (but less significantly so) the distribution of stellar mass, the ratio of the stellar-to-total mass density increasing by  $\sim 20\%$  from the center to  $r_{200}$ . In other terms, the stellar mass fraction does depend on radius, but this dependence is not strong. This is consistent with the fact that the best-fit NFW model scale radius for the total mass density profile is only marginally different from that of the stellar mass density profile (see Table 3.5).

The median value of  $\rho_*/\rho_{tot}$  within  $r_{200}$  is slightly higher (but not significantly so) than

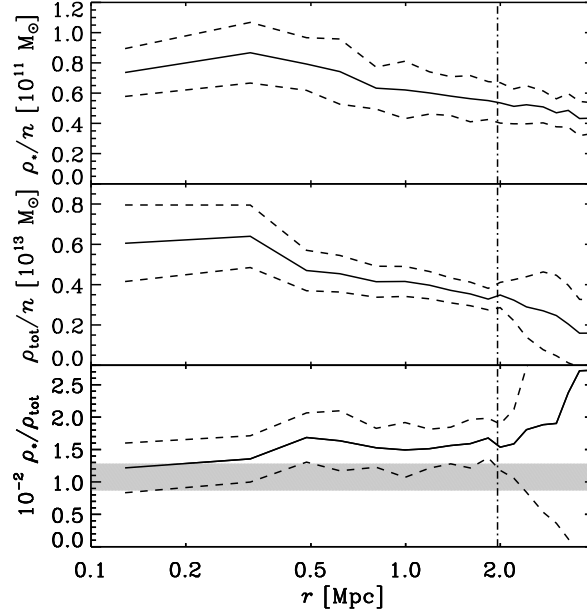


Figure 3.14. Top panel: the ratio of the stellar mass density and number density profiles. Middle panel: the ratio of the total mass density and number density profiles. Bottom panel: the ratio of the stellar mass density and total mass density profiles. Dashed lines indicate  $1\sigma$  confidence regions. All densities are volume densities. The vertical dash-dotted line indicates the location of  $r_{200}$ . The horizontal gray area indicates the cosmic value of the stellar mass fraction at the cluster mean redshift and its  $1\sigma$  uncertainty.

the (physical, not comoving) cosmic value of  $0.011 \pm 0.002$  at the cluster mean redshift, evaluated using the stellar mass density values of [Muzzin et al. \(2013a, their Table 2\)](#) and the adopted cosmological value for  $\Omega_M$ .

## 3.5 Discussion

I find a very strong dependence of the cluster SMF on the galaxy type. This dependence is found in the whole cluster, as well as in different cluster regions defined by their cluster-centric distance or by their local galaxy density. This dependence has been found previously in several studies (e.g. [Bolzonella et al., 2010](#)). The sum of the passive and SF SMFs gives

rise to a SMF that deviates from a simple Schechter beyond the  $M_*$  value where the two type SMFs cross each other (see Fig.13 in Peng et al., 2010b). Indeed, we find that the fit of the SMF of all galaxies by the sum of the two best-fit Schechter functions of the passive and SF populations, is significantly better than the fit by a single Schechter. At the redshift of M1206 ( $z=0.44$ ), the model of Peng et al. (2010b) predicts that the SMFs of passive and SF galaxies should cross at  $\log M_*/M_\odot \approx 10.1$  in dense environments, which is the value found for the SMF of M1206 (see Fig. 3.7). This value depends on the environment; in fact the crossing mass is  $\log M_*/M_\odot \approx 10.5$  (resp. 9.5) for the SMF of galaxies outside (resp. within)  $r_{200}$ , and smaller than that found in the field by Muzzin et al. (2013a, see their Fig.10). Hence, I confirm the prediction of Peng et al. (2010b) that the value above which passive galaxies dominate the SMF shifts to lower masses in denser regions.

The shape of the SMF of SF galaxies does not depend on the environment, although I cannot examine it within the densest cluster region for lack of statistics. This is also in line with predictions from the model of Peng et al. (2010b), and with other observations of field galaxy SMFs (e.g. Ilbert et al., 2010; Huang et al., 2013), and luminosity functions (e.g. Martinet et al., 2015).

There is little or no evidence of an environmental dependence of the shape of the SMF of passive galaxies outside the very central (densest) region. Peng et al. (2010b) do predict an environmental dependence and present evidence for it in a sample drawn from SDSS data, but other analyses have failed to detect such a dependence (e.g. Vulcani et al., 2012, 2013). Balogh et al. (2001) have found the SMF of passive galaxies to be steeper in clusters than in the field, as expected if mass quenching occurs earlier in denser environments at a given mass (Peng et al., 2010b), but Giodini et al. (2012) have found that the SMF of passive galaxies is steeper in the field than in groups of galaxies.

I do find a very significant change in the SMF of passive cluster galaxies in the very inner (and densest) region,  $R \leq 0.25 r_{200}$ , corresponding to  $\simeq 0.5$  Mpc (see Fig. 3.9, bottom left panel). This change corresponds to a very steep radial decrease in the number ratio of giant ( $M_*/M_\odot \geq 10^{10.5}$ ) to subgiant ( $10^{9.5} \leq M_*/M_\odot < 10^{10.5}$ ) galaxies (GSNR; see Fig. 3.11), from the center to  $\sim 0.8$  Mpc. Beyond this radius the GSNR increases but more gently toward the cluster outskirts. The GSNR of SF galaxies does not show a significant radial dependence, but the innermost region is not sampled by this dataset, for lack of a statistical significant number of SF galaxies.

The definition of ‘subgiants’ adopted in this Thesis is close to the definition of ‘dwarfs’ used by Sánchez-Janssen et al. (2008), i.e., galaxies 1.0 mag fainter than the characteristic magnitude in the  $r$ -band luminosity function. Their magnitude cut roughly corresponds to  $M_* \sim 10^{10.5} M_\odot$ . Using a large number of nearby clusters they find a clear increasing trend in the dwarf/giant number ratio with clustercentric radius, out to  $\sim 2 r_{200}$ , and they find this trend to be due to blue galaxies, while no trend is found for the red galaxies. Their results

are therefore completely at odds with the ones found in this Thesis. Since the cluster sample analyzed by [Sánchez-Janssen et al. \(2008\)](#) is at  $z < 0.1$ , this difference seems to suggest a rapid evolution of the GSNR, different for the different populations of cluster galaxies. Quenching will transform the SF galaxies in M1206 into passive galaxies, which could flatten the dependence of the passive GSNR with radius (see Fig. 3.11), making it more similar to the GSNR observed by [Sánchez-Janssen et al. \(2008\)](#) for red galaxies. It is however more difficult to suggest a scenario for why the GSNR of blue/SF galaxies should grow a radial dependence with time.

My results appear more consistent with the findings of [Popesso et al. \(2006b\)](#) and [Barkhouse et al. \(2009\)](#). [Popesso et al. \(2006b\)](#) find a lack of dwarf, red galaxies in the central cluster regions, and [Barkhouse et al. \(2009\)](#) find an increase in the number ratio of dwarf to giant red galaxies with clustercentric radius. In both studies there is no radial trend of the blue dwarf/giant ratio. The comparison with the presented results is not straightforward, however, as both studies are based on the analysis of luminosity rather than mass functions. Moreover, the definition of ‘subgiants’ adopted in the present work differ from their definition of ‘dwarfs’. In [Barkhouse et al. \(2009\)](#) dwarfs are galaxies that are 2.8 mag fainter than the characteristic magnitude in the  $R_C$ -band luminosity function, i.e., 1.12 dex below the value of  $M^*$  in our SMF, or  $M_\star \sim 10^{9.8} M_\odot$ . This limit is too close to the completeness limit of the sample and it cannot be adopted as the separation value to distinguish giant from subgiant (or dwarf) galaxies.

An interpretation of the GSNR trends can be given in terms of a scenario involving the processes of ram-pressure stripping ([Gunn and Gott, 1972](#)), harassment ([Moore et al., 1996, 1998](#)), and tidal destruction ([Merritt, 1984](#)). As a SF galaxy approaches the cluster center it is transformed into a passive galaxy by harassment and ram pressure. The SF galaxies are on average less massive than passive galaxies, and in addition, their masses may become even smaller as they are transformed to passive galaxies, e.g., by harassment. As a result, the number of passive galaxies increases with time especially at the low-mass end, and particularly so in the denser cluster regions where the transformation processes are more effective. This creates a decreasing trend of the passive galaxy GSNR from the cluster outskirts to its center. However, this trend might be reversed at very small radii because tidal mass stripping become so effective there that the low-mass galaxies are either totally destroyed or mass-stripped below the completeness limit of a given survey ( $10^{9.5} M_\odot$  in this case).

A detailed and perhaps dedicated analysis of semi-analytical models in the context of cosmological numerical simulations would be required to (dis)prove this scenario, and this is beyond the scope of this thesis. It is possible however refer to the simulation work of [Conselice \(2002\)](#) where the value  $\alpha$  of the luminosity function of cluster galaxies is first shown to increase (in absolute values) and then decrease, as the number of interactions among galaxies increases. The initial increase is due to tidal stripping, until the stripping becomes

so strong that stripped galaxies drop off the completeness limit of the given survey. The same non monotonous trend of  $\alpha$  with local galaxy density is observed in this analysis (see Sect. 3.3.2).

Further support to this scenario comes from the comparison of the amount of mass in the ICL and of the mass that is missing from subgiant galaxies in the SMF of the innermost region. The missing mass from subgiant galaxies is determined with the following equation:

$$\Delta M_{sub} \equiv \int_{10^{9.5} M_{\odot}}^{10^{10.5} M_{\odot}} m \Phi_a^*(m) dm - \int_{10^{9.5} M_{\odot}}^{10^{10.5} M_{\odot}} m \Phi_a(m) dm, \quad (3.4)$$

where  $\Phi_a$  is the SMF of passive galaxies in Region (a) not normalized, while  $\Phi_a^*$  is the SMF of passive galaxies if substituting the value of the slope with the best-fit value obtained for the SMF in Region (b). The integral is done between the completeness mass limit and the mass at which the SMFs of passive galaxies in Regions (a) and (b) intersect each other ( $\sim 10^{10.5} M_{\odot}$ ). The SMF of Region 1 shown in Fig. 3.9 has been normalized to the total number of galaxies contained in the subsample. In eq. 3.4 the non normalized SMF is used, with  $\Phi^* = 121$ . The lower limit of the integral corresponds to the completeness limit of the sample. The upper limit of the integral corresponds to the mass value where the normalized SMF of Region 1 intersects the normalized SMF of the adjacent Region 2 (see Fig. 3.9, bottom left panel). This mass value is also chosen to separate giant from subgiant galaxies.

The uncertainty on this difference is estimated by repeating this estimate with slopes fixed to the  $\alpha \pm d\alpha$  values of Region 2, where  $d\alpha$  is the error on  $\alpha$  (see Table 3.3). The value obtained,  $\Delta M_{sub} = 5.8_{-2.9}^{+3.3} \times 10^{11} M_{\odot}$ , can be compared with the estimate of ICL stellar mass in M1206,  $9.9 \pm 3.8 \times 10^{11} M_{\odot}$  (Presotto et al., 2014). These two values are consistent within  $\sim 1\sigma$ , within their admittedly large uncertainties. This estimate would not change by more than 30% if one would extrapolate the integral of eq. 3.4 to very low masses, and in any case the dominant contribution to the ICL is expected to come from intermediate-to-high mass galaxies (Murante et al., 2007a; Contini et al., 2014a). This comparison is consistent with a scenario where the missing subgiant galaxies in the innermost cluster regions have lost part of their stellar mass into a diffuse intracluster component due to interactions with other cluster members or with the tidal cluster field. With a very similar approach Giallongo et al. (2014) come to the same conclusions about the nature of the ICL in another  $z \sim 0.4$  cluster.

The radial dependence of the GSNR is also reflected in the decreasing stellar mass-to-number density profile ratio (see Fig. 3.11). On average, among galaxies with  $M_{*} \geq 10^{9.5} M_{\odot}$  those near the cluster center are  $\sim 30\%$  more massive than those near the cluster virial radius. This is not because of the presence of the central BCG, which was excluded from the analysis when the density profiles are determined. This finding is consistent with the mild mass segregation found in groups by Ziparo et al. (2013), and with the mass segregation found in clusters at  $z \sim 1$  by van der Burg et al. (2013). In particular, the ratio of the best-fit

concentrations of the stellar mass density and number density profile found by [van der Burg et al. \(2013\)](#),  $1.4 \pm 0.4$ , is fully consistent with the ratio obtained for M1206,  $1.6 \pm 0.4$ . [van der Burg et al. \(2013\)](#) attribute this mass segregation to dynamical friction, which should have occurred before  $z \sim 1$ , with little if any further evolution thereafter. However, mass segregation can also be the result of tidal stripping in the central cluster region, affecting galaxies in different ways depending on their mass. Since galaxies of lower mass are more affected by tidal stripping, they lose mass and drop off the completeness limit of  $10^{9.5} M_{\odot}$  in this dataset.

To discriminate between dynamical friction and tidal stripping as the driving process of mass segregation in M1206, we should turn our attention to the total mass density profile. The total mass density profile is more concentrated than the galaxy number density profile, as already found by [Biviano et al. \(2013\)](#), as well as in many other clusters (e.g. [Biviano and Girardi, 2003](#); [Lin et al., 2004](#); [Biviano and Poggianti, 2009](#)). However, in M1206 the total mass density profile is more concentrated than the stellar mass distribution, which is an entirely new result. Should dynamical friction be responsible for the observed mass segregation we would expect the total mass density profile to be less concentrated than the stellar mass density profile, as the diffuse dark matter component should gain energy at the expense of the subhalos (e.g. [Del Popolo, 2012](#)). Instead, I find the opposite. This suggests that the observed mass segregation is not due to dynamical friction in M1206, but to tidal disruption of the less massive galaxies. Since most of the stellar mass is in the most massive galaxies, while most of the galaxies are low-mass galaxies, this process affects the number density profile much more severely than the stellar mass density profile.

The radial dependence of the stellar-to-total mass ratio is very mild. This mild dependence is consistent with the results of [Biviano and Salucci \(2006, see their Table 1\)](#), obtained using a sample of 59 nearby clusters (fully described in [Biviano et al., 2002](#)), and [Bahcall and Kulier \(2014, see their Fig.9\)](#), obtained using a sample of  $z < 0.3$  clusters. [Bahcall and Kulier \(2014\)](#) find that the stellar mass fraction is roughly constant out to  $\sim 40 r_{200}$ . Their result are confirmed in M1206 out to  $\sim r_{200}$ ; beyond that radius the error bars in this analysis become very large (see Fig. 3.11). Their determination of the average cluster stellar mass fraction also agrees very well with the cosmic value, while in this work the determination is consistent, but slightly above, the cosmic value.





# Abell 209

---

The results of this chapter are in press in [Annunziatella et al. \(2015, arxiv=1510.05659\)](#).

## 4.1 Introduction

As already said in Chapter 1, when galaxies are accreted into a cluster, they can be subjected to different environmental processes which can halt their star formation and, sometimes also change their morphology. Hence, the properties that are most likely to be influenced by these processes, beside the star formation rate of a galaxy, are: stellar mass, size, and morphological type. The study of the distribution of these properties and the correlation existing among them and with their environment gives information on the relative importance of the processes that affect their evolution. In Chapter 3, I already discussed the influence of environmental processes on the galaxy SMF by reviewing literature results and presenting those obtained for the CLASH cluster M1206 at  $\bar{z} = 0.44$ . In this chapter, I want to analyze the effect of the environment on the SMF of galaxies in another CLASH cluster, A209, at  $\bar{z} = 0.21$ . The analysis of the SMF was performed for two reasons: to check whether the results found for the dynamically relaxed cluster M1206 holds also for a cluster with evidence of substructures ([Mercurio et al., 2003](#)) and, to study possible redshift evolution effects comparing the results obtained in the two clusters, which are separated by  $\sim 2$  Gyr in cosmic time.

Another way to constrain the effect of different environmental processes on the evolution of galaxies is to analyze the distribution of galaxies sizes and the relation with the stellar mass.

It is known that different types of galaxies, namely early types (ETGs) and late types show different dependencies between size and stellar mass (Shen et al., 2003). In particular, the mass-size relation of ETGs is steeper than the one found for late type galaxies. However, how environmental processes can affect the distribution of galaxy sizes is still uncertain. Semi-analytic models predict that galaxies in more massive halos tend to have larger sizes than galaxies in lower mass halos, at fixed stellar mass and redshift (Shankar et al., 2013). Unfortunately, observational studies carried out at different redshifts lead to controversial results. At low redshift, Maltby et al. (2010) identified only a weak dependence of the size-mass relation on local galaxy environments for low mass spiral galaxies. They found that low mass spiral galaxies ( $\log(M/M_\odot) < 10.0$ ) had a mean effective radius 15-20% larger than that of similar spirals in the cluster. In the local Universe, Valentinuzzi et al. (2010) detected a higher fraction of super dense galaxies in clusters than in the field. This result was then confirmed also in Poggianti et al. (2013), who also claimed that at fixed stellar mass, cluster ETGs are slightly smaller than field ones. On the other hand, at higher redshift ( $0.2 < z < 1.1$ ), Huertas-Company et al. (2013) found no dependence of the size-mass relation of passive ETGs on environments ranging from field to groups. In this redshift range, Cooper et al. (2012), focusing only on the high-mass tail of the passive galaxies distribution, found that galaxies in the densest environment have effective radii 25 % larger than those at the lower end of the density distribution. Finally, Lani et al. (2013) found that passive galaxies in denser environments are significantly larger at a given stellar mass in the redshift range  $1 < z_{phot} < 2$ . The reason behind these differences has still to be understood, and might come from different sample selections, different methods used to determine galaxy sizes, differences in the way environment is measured and/or low statistics at high redshift. Many of the physical processes that can affect the properties of cluster galaxies are likely to be related to their orbits. Galaxies on radial orbits, characterized by small pericenters, can experience denser environments than galaxies on more tangential orbits. This can lead to their more rapid destruction (Taylor and Babul, 2004). It has been suggested by Solanes et al. (2001) that among Virgo cluster galaxies, those with evidence of gas stripping are on more radial orbits than the others.

The cluster A209 is at lower redshift with respect to M1206. For this reason, it was possible to carry out a more extensive analysis starting from the same kind of dataset. In particular, I derived the map of the intra-cluster light and study some properties of the ICL in A209, I performed the analysis of the orbits of passive galaxies and finally I analyzed the mass-size relation of passive galaxies in two regions of the cluster. As for the cluster M1206 I also derived the stellar mass density and number density profiles and compared with the total mass density profile obtained from an independent lensing analysis (Merten et al., 2014).

## 4.2 The A209 data sample

The main properties of A209 are listed in Table 4.1.

Mean redshift	$0.2090 \pm 0.0004$
Velocity dispersion [ $\text{km s}^{-1}$ ]	$1320^{+64}_{-67}$
Virial radius $r_{200}$ [Mpc]	$2.13 \pm 0.05$

Table 4.1. Main properties of the cluster Abell 209. The radius corresponds to the radius of a sphere whose mass overdensity is 200 times the critical density at the cluster redshift. The value of the redshift is taken from [Mercurio et al. \(2003\)](#). The velocity dispersion is calculated on our dataset (Sartoris et al. in prep.), while the virial radius is taken from [Merten et al. \(2014\)](#).

The RGB image of the cluster is shown in Fig. 4.1.

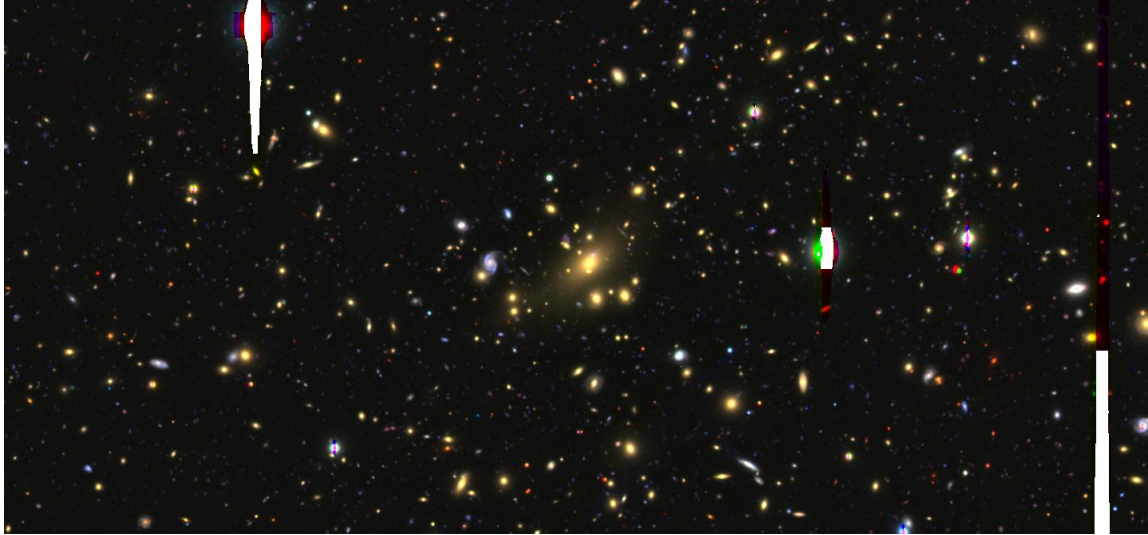


Figure 4.1. Color image of A209 obtained by combining Subaru images in the  $z$ ,  $i_p$ ,  $B$  bands. The size of the image is  $9 \times 4$  arcmin, corresponding to  $2 \times 1$  Mpc at redshift 0.21.

For this cluster, a total of 11 LR-Blue masks were acquired with VLT/VIMOS, as part of the CLASH-VLT, using four separate pointings, each with a different quadrant centered on the cluster core. The LR-Blue masks cover the spectral range 370-670 nm with a resolving power  $R = 180$ , for a total exposure time of 10.5h. Spectra are classified according to the reliability of the redshift (see [Biviano et al. 2013](#)) in: secure (QF = 3; 1946 objects) with a probability of  $>99.99\%$ , based on emission-lines (QF = 9; 110 objects) with a probability of  $\sim 92\%$ , and likely (QF = 2; 492 objects) with  $\sim 75\%$  probability.

Membership for objects with spectroscopic redshift is assigned according to the peak+gap (P+G) method (see Chapter 2).

The final spectroscopic dataset consists of 2548 reliable redshifts, observed as part of CLASH-VLT, in addition to 110 taken from [Mercurio et al. \(2003\)](#) and [Mercurio et al. \(2008\)](#). In total, 1116 are confirmed members.

Photometric data were obtained with the Subaru/Suprime-Cam from SMOKA ([Baba et al., 2002a](#)) covering a  $30' \times 30'$  field of view, with total exposure times of 2400 s, 1800 s, 2400 s, 1320 s and 4800 s in the B, V,  $R_c$ ,  $I_p$  and z band, respectively. The typical seeing in the final sky-subtracted images varies from 0.486 arcsec in the R band up to 0.77 in the B band with a pixel scale of 0.2 arcsec. Photometric redshift are estimated for all galaxies that have been detected in all the observed bands following the method explained in Chapter 2.4.2.

To determine if galaxies with  $z_{phot}$  can be classified as members, I investigate the diagram shown in Fig. 4.3. The objects with spectroscopic redshift are used to find the best selection criteria to identify cluster member galaxies. I select as cluster members those galaxies with  $0.175 < z_{phot} < 0.272$  (see horizontal lines in Fig. 4.3). With these cuts in  $z_{phot}$  92% of the spectroscopic members are classified correctly, minimizing the number of interlopers. The sample of photometrically selected members contains 1805 galaxies down to the magnitude limit  $R_c = 24.0$  mag. The selection of members based on photometric redshifts is not as reliable as that based on spectroscopic redshifts. I take this into account as explained in Chapter 2.4.2. The sample needs to be corrected for two different factors. One is the incompleteness of the sample with photometric redshift with respect to the photometric sample, since to obtain  $z_{phot}$ , it is required that the galaxies have to be detected in all the five Subaru bands. The other takes into account possible discrepancies between  $z_{phot}$  and  $z_{spec}$  in the photometric selection of members, and I call it membership correction. In order to account for these corrections, I follow the method presented in Sect 2.4.3. The photometric completeness,  $C$ , is approximately constant,  $\geq 80\%$ , down to  $R_c \leq 24$  mag independently from magnitude or galaxy type. Therefore, I adopt a constant mean value  $C = 0.81$  and a correction factor,  $f_C = 1/C = 1.23$ .

In Fig. 4.4 it is shown the dependence of the membership correction factor  $f_M$ , from galaxy type, magnitude and distance from the cluster center. The correction factor depends on galaxy type, while it is independent from both magnitude and clustercentric distance. Two

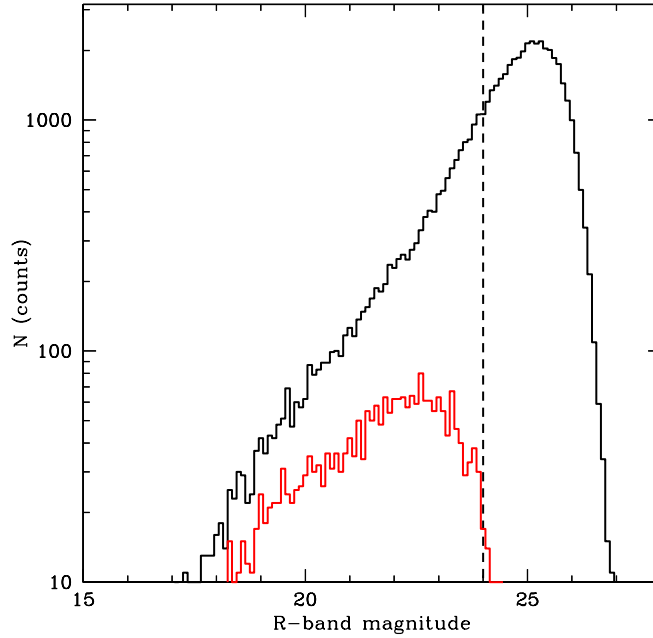


Figure 4.2. Histogram of the  $R_c$ -band magnitude of the 51166 objects in the photometric (black line) sample and of the 2622 sources with reliable redshifts (red line).

different values have been used for red and blue galaxies in the entire magnitude and radial range,  $f_M = 0.9$  and  $0.75$ , respectively. The final correction factor applied is  $f_C \cdot f_M$  ( $\sim 1.12$  and  $0.94$  for passive and SF galaxies, respectively).

Stellar masses of cluster member galaxies have been obtained using the SED fitting technique performed by MAGPHYS. Galaxies have been divided in Passive and SF according to the value of their sSFR, as in Chapter 3. The limiting magnitude of  $R_C = 24$  mag corresponds roughly to a completeness limit of  $10^{8.6} M_\odot$  for passive galaxies, according to the mass vs  $R_C$  relation of Fig. 4.5. The mass limit for SF galaxies would be lower. However, the same value for passive and SF galaxies is chosen in order to be consistent when comparing the SMF of different galaxy types. With this mass limit, the final sample consists of 1916 galaxies, of which more than half are spectroscopically confirmed members.

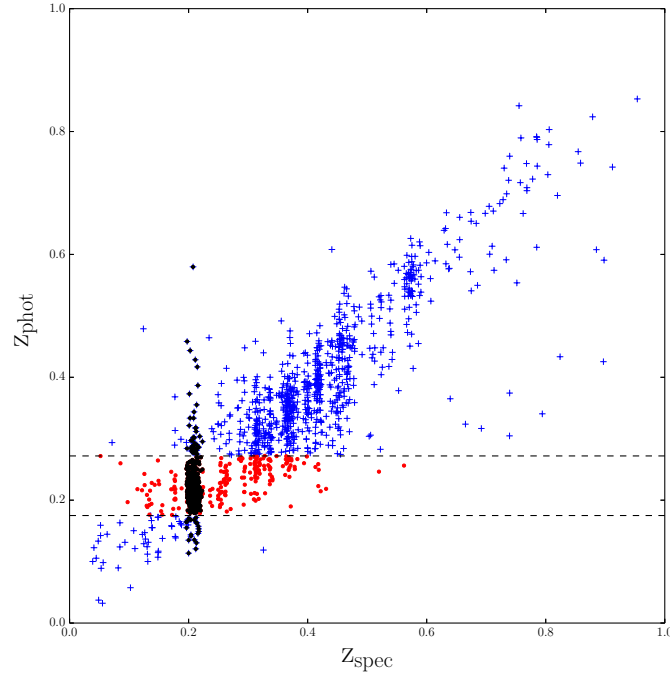


Figure 4.3. Photometric vs. spectroscopic redshifts for galaxies in the cluster field and in the magnitude range  $18 \leq R_C \leq 24$  mag. Black dots are spectroscopically confirmed members. The two dashed lines represent the chosen criteria in photometric redshifts to classify the cluster members. Galaxies within this range of photometric redshift are colored in red. Galaxies with  $z_{phot}$  in this range and without spectroscopic information are classified as members. Blue crosses are galaxies outside both the spectroscopic and photometric selections.

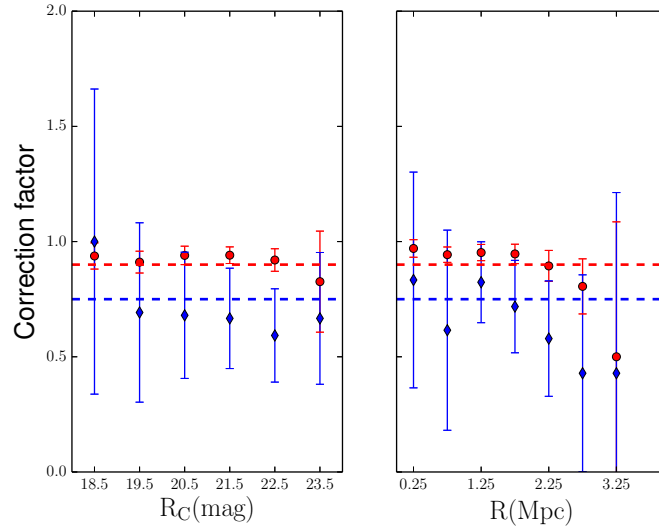


Figure 4.4. Correction factor ( $f_M$ ) for membership selection as a function of  $R_C$  magnitude (left panel) and clustercentric distance (right panel), for red (dots) and blue (diamonds) galaxies.

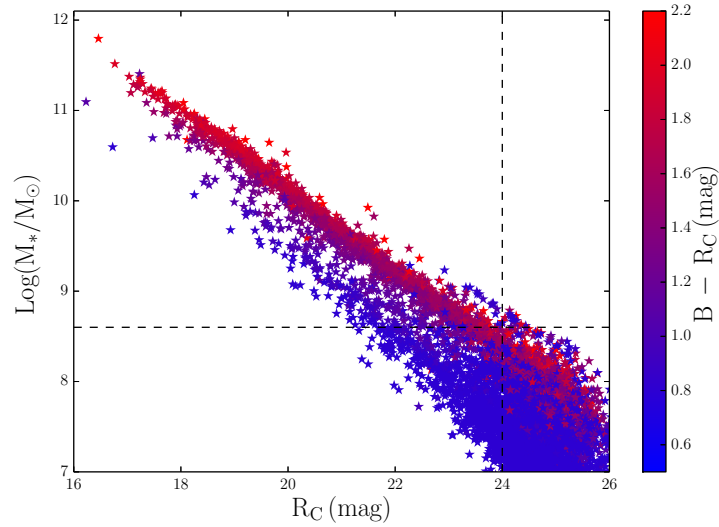


Figure 4.5. Relation between the stellar mass and the  $R_C$  magnitude. The points are color coded according to the  $B - R_C$  color. Dashed vertical and horizontal lines are the magnitude and mass limits, respectively.

## 4.3 The stellar mass function

The SMF of cluster members is obtained by considering the number of galaxies in each stellar mass bin weighted for the completeness and the membership correction factors. The errors on the counts are estimated with the bootstrap procedure (Efron and Tibshirani 1986). The  $M_*$  distributions are then fitted with a Schechter function (see Eq. 3.1) down to the mass limit  $10^{8.6} M_\odot$  using the maximum likelihood technique. In these fits each galaxy has a weight equal to the product  $f_C \cdot f_M$  defined in Sect. 2.4.3. Also in this case, I have checked that the contribution of the errors on the stellar mass value is smaller than the statistical errors associated to each of the parameters of the SMF. The correction factor in Fig. 4.4, as shown, is independent from magnitude or radial distance. Therefore, the errors on this factor would influence only the normalization of the SMF. The only two cases in which I take into account the normalizations are when studying the total SMF (Sect. 4.3.1) and when estimating the contribution of galaxies of different mass to the ICL (Sect. 4.4.2). To estimate the contribution of the errors in these two cases, I repeat the calculations using  $f_M \pm \Delta f_M$ . The obtained results are statistically consistent with those obtained using  $f_M$ . Thus, for this analysis I do not consider the errors on the membership correction factor. The cumulative SMF for all galaxies in A209 is given in Fig. 4.6 (violet line).

Since I want to compare only the shape of the SMF of different samples, I renormalize the SMFs by dividing them by the total number of objects in each sample (except in Fig. 4.6). In order to establish if two SMFs are statistically different I compare the shape parameters ( $\alpha$  and  $M^*$ ) without taking into account the normalization values. To highlight the difference between two SMFs, I also perform the K-S test (see also Sect. 3.3).

Table 4.2. Best-fit Schechter function parameters

Galaxy type	$\alpha$	$\log(M^*/M_\odot)$
Passive	$-1.09 \pm 0.02$	$11.10 \pm 0.05$
SF	$-1.63 \pm 0.03$	$11.02 \pm 0.30$
All	$-1.17 \pm 0.02$	$11.15 \pm 0.05$

### 4.3.1 Different galaxy types

The SMFs of separately SF and passive cluster member galaxies are shown in Fig. 4.6. The best-fit values of  $\alpha$  and  $M^*$  with their  $1\sigma$  errors are listed in Table 4.2 and shown in Fig. 4.7. The uncertainties are obtained by marginalizing over the normalization parameter. The SMFs of, separately, SF and passive cluster members are adequately fitted by a single



Schechter function. In order to assess the goodness of the fits, I compare the mass distribution of galaxies in the considered sample with the best-fit Schechter function using the K-S test. I perform this test for all the SMFs considered in this paper, except for the SMF of all cluster members, always obtaining P-values  $> 10\%$ . Therefore, the null hypothesis that the observed and model distributions are statistically identical can not be rejected. The SMF of passive and SF cluster members is given by the sum of the SMFs of separately SF and passive galaxies. The dependence of the SMF on galaxy type is statistically significant. This is evident from the comparison of the shape of the two SMFs but also from the results of the K-S test (see Table 4.4). The difference between the mass distribution of passive and SF galaxies holds not only when considering the whole cluster, but also in different cluster regions. From Fig. 4.6 one can see that the passive SMF dominates over the SF one at all masses down to the completeness limit in A209. In Sect. 3.3, I found that the two SMFs of SF and passive galaxies for the cluster M1206 at  $z \sim 0.44$  crossed at the value  $M_{\text{cross}} \sim 10^{10.1} M_{\odot}$ , if considering the whole cluster region, and  $M_{\text{cross}} \sim 10^{9.5} M_{\odot}$ , if the analysis was restricted to the virial region of the cluster. The difference between what happens in the two clusters can be partially explained by the Butcher-Oemler effect (Butcher and Oemler 1978), according to which galaxy clusters at intermediate redshift contain a larger fraction of blue galaxies than lower redshift ones. On the other hand, there is a striking difference between the slope of the SMF of passive galaxies in A209 and the one found for passive galaxies in M1206 ( $\alpha_{\text{passive M1206}} = -0.38 \pm 0.06$ ). I did check that this difference in slope is not due to the different completeness limit that are reached in the two cases. The difference between the SMF of passive galaxies in the two clusters at different redshifts is qualitatively in agreement with the results shown in Rudnick et al. (2009). In their paper, the authors found that the luminosity functions of passive galaxies showed a strong evolution with redshift in terms of an increase of faint galaxies relative to bright ones towards lower redshifts. Another feature of the passive galaxy SMF is the dip visible in the galaxy counts at  $\sim 10^{10.1} M_{\odot}$ . The presence of this dip was also found in the luminosity function of red-sequence galaxies of this cluster (Mercurio et al. 2003) at the magnitude in the R band  $\sim 19.8 \text{ mag}$  which corresponds (according to the fit in Eq. 4.1) to our mass value. This dip is probably an indication that there are two populations of passive galaxies, one of lower masses probably originated from the quenching of SF galaxies, and another of higher masses. To verify this I fit a double Schechter to our data in Sect. 4.3.3.

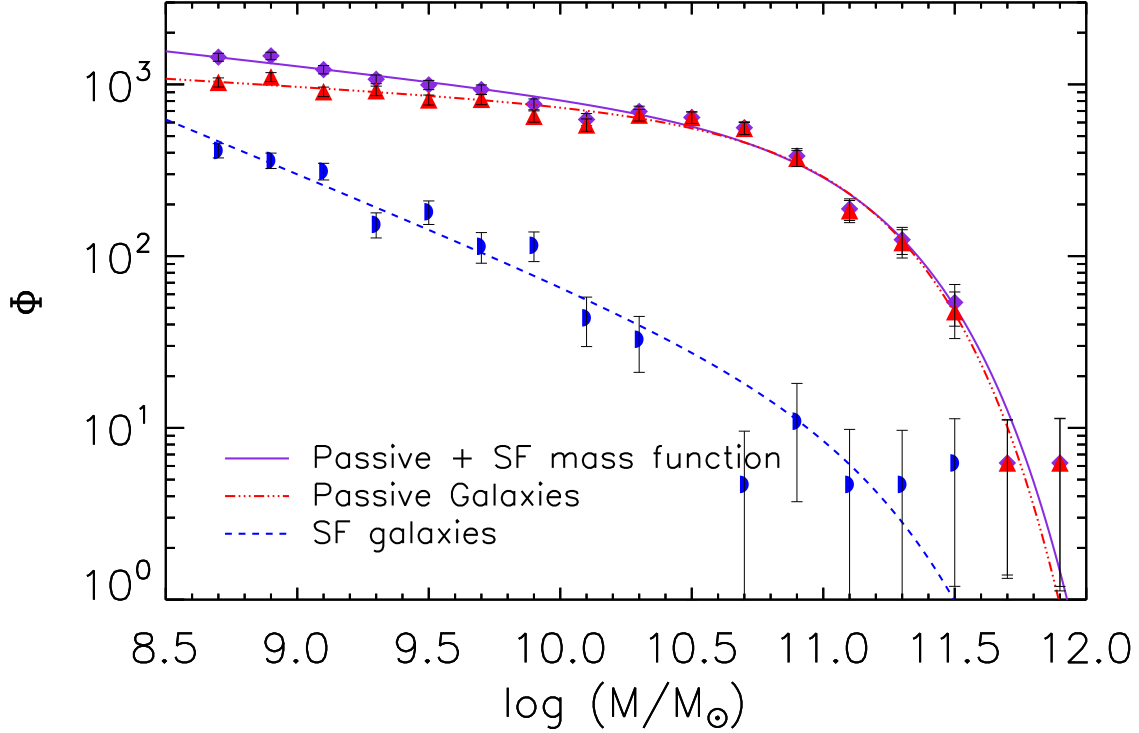


Figure 4.6. SMFs of SF and passive cluster member galaxies. The best-fit Schechter functions are shown with the blue dashed line for SF galaxies and red triple-dot-dashed line for passive galaxies, while the number counts (divided for the bin size) are the blue demi-circles and red triangles, respectively. Violet diamonds are the counts obtained for all cluster members and the violet solid line represents the sum of the two SMFs. Counts are evaluated in bins of 0.2 dex in  $M_*$ . The  $1\sigma$  errors on the counts have been estimated via the bootstrap resampling procedure.

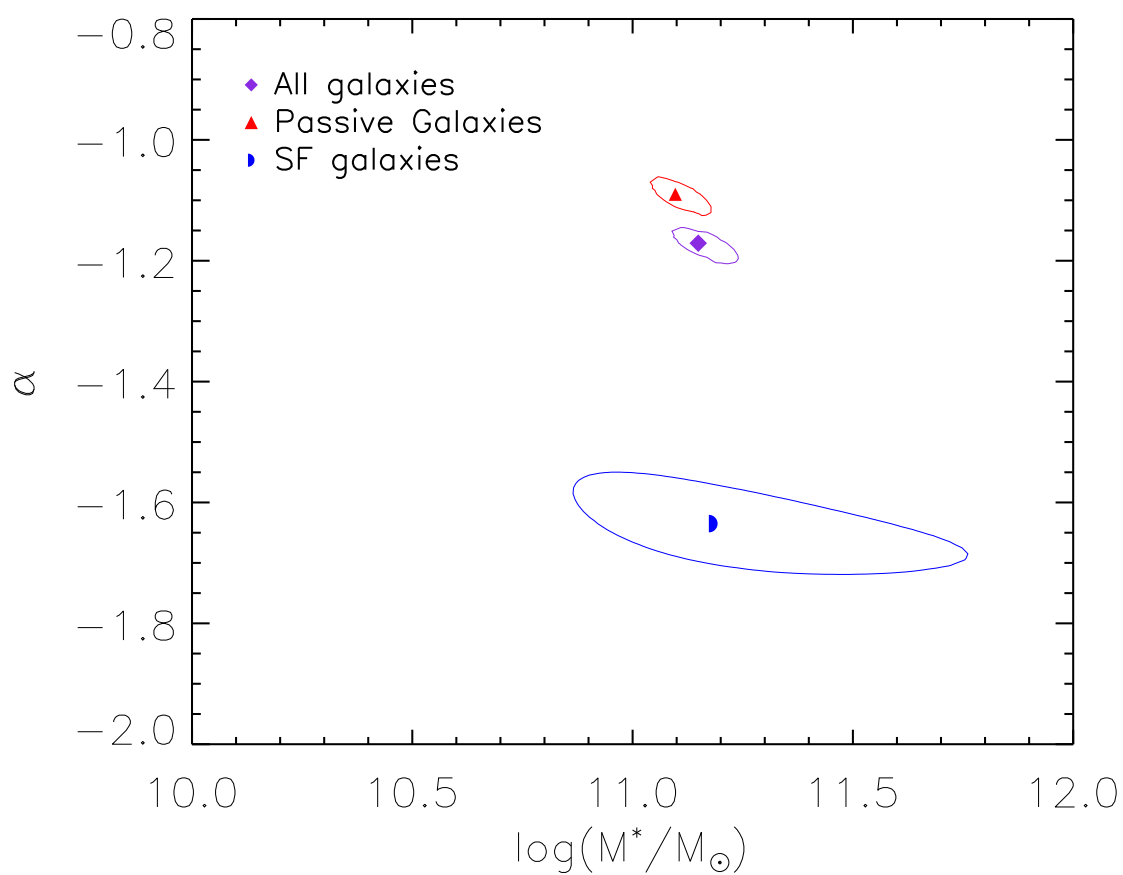


Figure 4.7. Best-fit values of the Schechter parameters  $\alpha$  and  $M^*$  with their 1  $\sigma$  likelihood contours.

Table 4.3. Best-fit Schechter function parameters for different environments

Galaxy type	Environment	$\alpha$	$\log(M^*/M_\odot)$
SF	$R > r_{200}$	$-1.58 \pm 0.08$	$10.95 \pm 0.30$
SF	$R \leq r_{200}$	$-1.69 \pm 0.07$	$11.42 \pm 0.45$
Passive	$R > r_{200}$	$-1.09 \pm 0.04$	$11.09 \pm 0.09$
Passive	$R \leq r_{200}$	$-1.09 \pm 0.02$	$11.10 \pm 0.05$
Passive	Region (a)	$-1.01 \pm 0.06$	$11.21 \pm 0.12$
Passive	Region (b)	$-1.09 \pm 0.04$	$11.09 \pm 0.08$
Passive	Region (c)	$-1.10 \pm 0.03$	$11.09 \pm 0.08$
Passive	Region (d)	$-1.10 \pm 0.03$	$11.03 \pm 0.07$

#### 4.3.2 Effects of global and local environments

To investigate the environmental dependences of the SMF, I consider separately SF and passive galaxies. In this way one can exclude the effects of the dependence of galaxy population from environment (Dressler 1980).

First I consider the SMFs of SF and passive galaxies inside the virial radius of the cluster ( $r_{200}$ ) and outside (out to  $\sim 1.7 r_{200}$ ). The SMFs and their best-fit Schechter parameters are shown in Fig. 4.8 and Fig. 4.9. The SMFs of SF galaxies inside and outside the virial radius are statistically indistinguishable (see the results of the K-S test in Table 4.4). The same result holds for passive galaxies, too.

The ‘environment’ is defined in units of the local density (number of galaxies per  $\text{arcmin}^{-2}$ ). I decided to use this definition of environment instead of the radial distance from the BCG (as in Chapter 3) since A209 is an elongated, dynamically not fully relaxed cluster (Fig. 4.10) and the regions identified by local density follow the cluster elongation, at variance with those identified by clustercentric radius.

The local density is obtained with a kernel density function, where the projected distribution of the galaxies is smoothed with a Gaussian kernel in an iterative way. Fig. 4.10 shows the distribution of galaxies in the cluster. The points are color coded according to the value of the local density ( $\Sigma$ ). I define four different regions according to their number density (in terms of galaxies per  $\text{arcmin}^{-2}$ ):

- (a)  $\Sigma > 9.0$ .

Table 4.4. Results of the K-S tests

Compared samples	N1, N2	Prob. (%)
Type dependence		
Passive vs. SF in the cluster	1580, 336	< 0.01
Passive vs. SF in Region (b)	425, 34	< 0.01
Passive vs. SF in Region (c)	488, 75	< 0.01
Passive vs. SF in Region (d)	75, 219	< 0.01
Environment dependence - SF galaxies		
SF within and outside $r_{200}$	161, 175	> 10
SF in Regions (b) and (c)	34, 75	> 10
SF in Regions (c) and (d)	75, 219	> 10
Environment dependence - passive galaxies		
Passive within and outside $r_{200}$	438, 408	> 10
Passive in Regions (a) and (b)	160, 425	8
Passive in Regions (b) and (c)	425, 488	> 10
Passive in Regions (c) and (d)	488, 57	> 10

(b)  $4.5 < \Sigma \leq 9.0$ .

(c)  $1.8 < \Sigma \leq 4.5$ .

(d)  $\Sigma \leq 1.8$ .

From Fig. 4.10 one can see that regions identified by  $\Sigma$  are not spherically symmetric. Another peculiar characteristic is that Region (a) is not centered on the BCG and that Regions (b) and (c) incorporate also a group in the N-NE direction. Mercurio et al. (2003) found that the center of the cluster was coincident with the position of the BCG. However, they used a sample of brighter spectroscopically confirmed member galaxies. Their magnitude limit ( $R < 22$  mag) roughly corresponds to a mass limit  $> 10^{9.5} M_{\odot}$  (see Fig. 4.5). If the analysis is limited to this sample of galaxies the center is coincident with the position of the BCG and

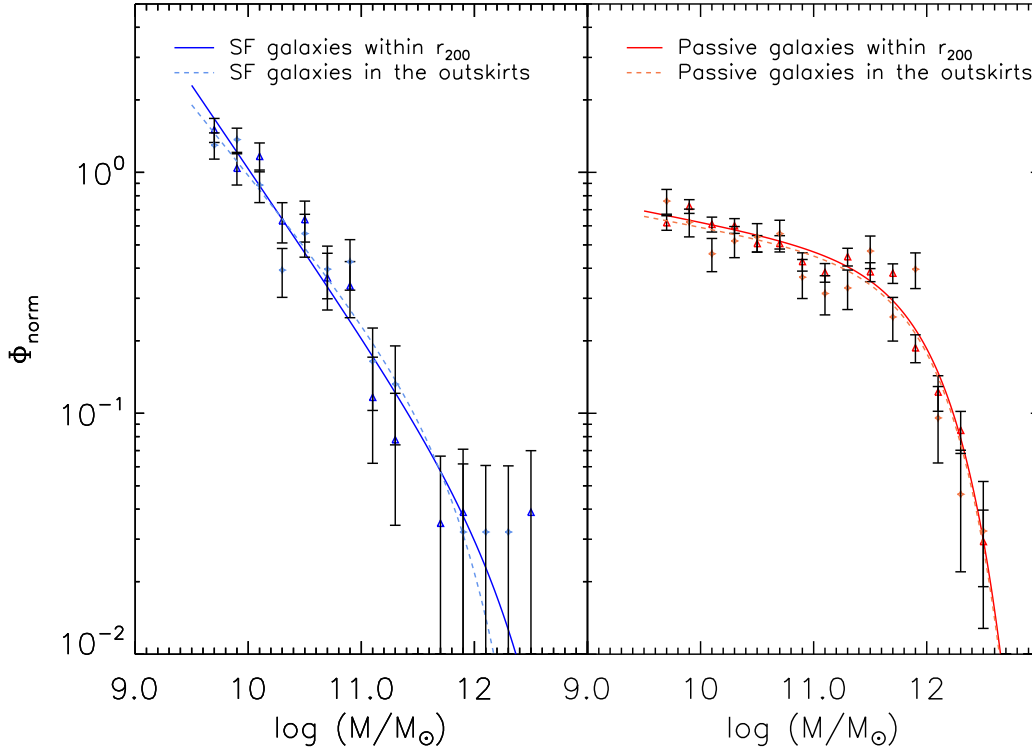


Figure 4.8. SMFs of SF (left) and passive (right) galaxies inside and outside the virial radius of the cluster. The SMFs are normalized to the total number of galaxies in each sample.

the region at high density in the NW direction disappears. In other terms the morphological appearance of the cluster changes according to the limiting magnitude of the sample.

The group in the N-NE direction contains very few cluster spectroscopic members. For this reason, after I checked that its presence does not affect the SMF of galaxies in different regions, I removed it from my analysis.

Fig. 4.11 shows the SMF of passive galaxies in Regions (a) to (d), and their best-fit parameters are reported in Fig. 4.12 and in Table 4.3. From Figs. 4.11 and 4.12 one can see that the SMF of passive galaxies depends on the local density. The environment has two effects on the SMF of passive galaxies in the densest region of the cluster: there is a higher number of high-mass galaxies than in less dense regions (that corresponds to a higher value of  $M^*$ ) but there is also a drop at the low-mass end of the SMF.

I applied the K-S test to the  $M_*$  distributions of separately SF and passive galaxies in adjacent

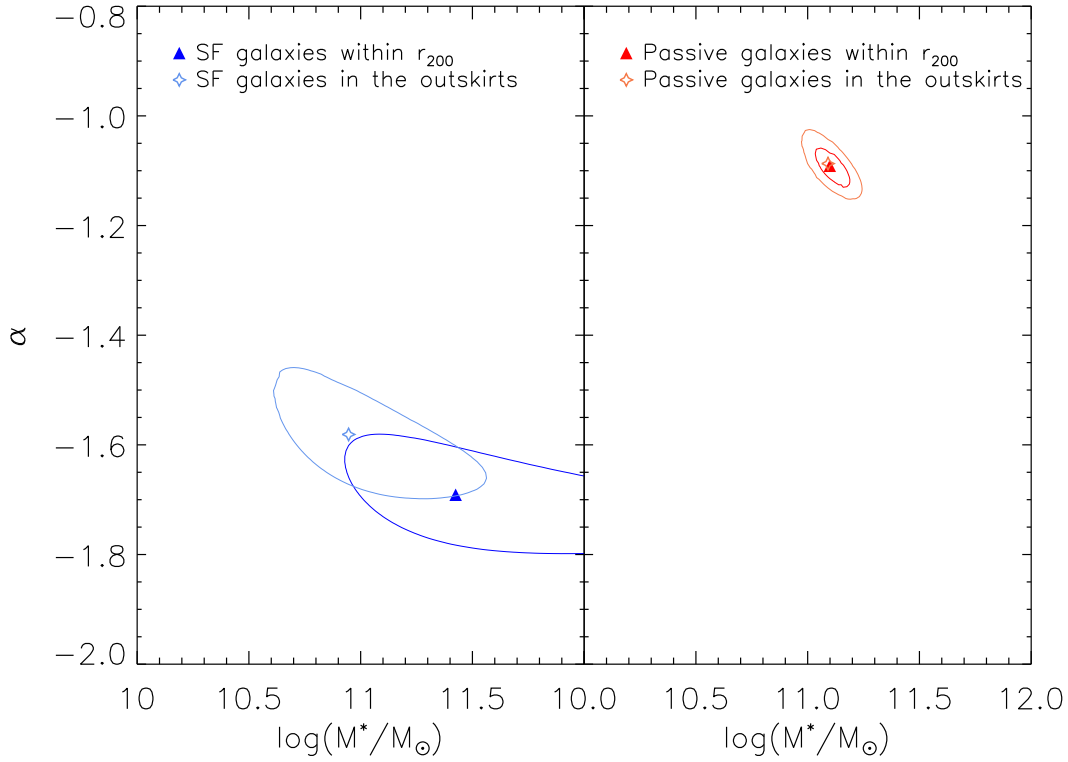


Figure 4.9. As in Fig. 4.7: best-fit Schechter parameters  $M^*$  and  $\alpha$  with their  $1\sigma$  contour in different regions of the cluster

regions. According to the results of the K-S test, in Regions (a) to (d) the  $M_*$  distributions of both SF and passive galaxies are not statistically different. However, this can be related to the fact that low-mass galaxies statistically dominate the samples. If I repeat the test restricting it to the galaxies with  $M_* > 10^{9.5} M_\odot$ , I find a significant difference between the mass distribution of passive galaxies in Regions (a) and (b).

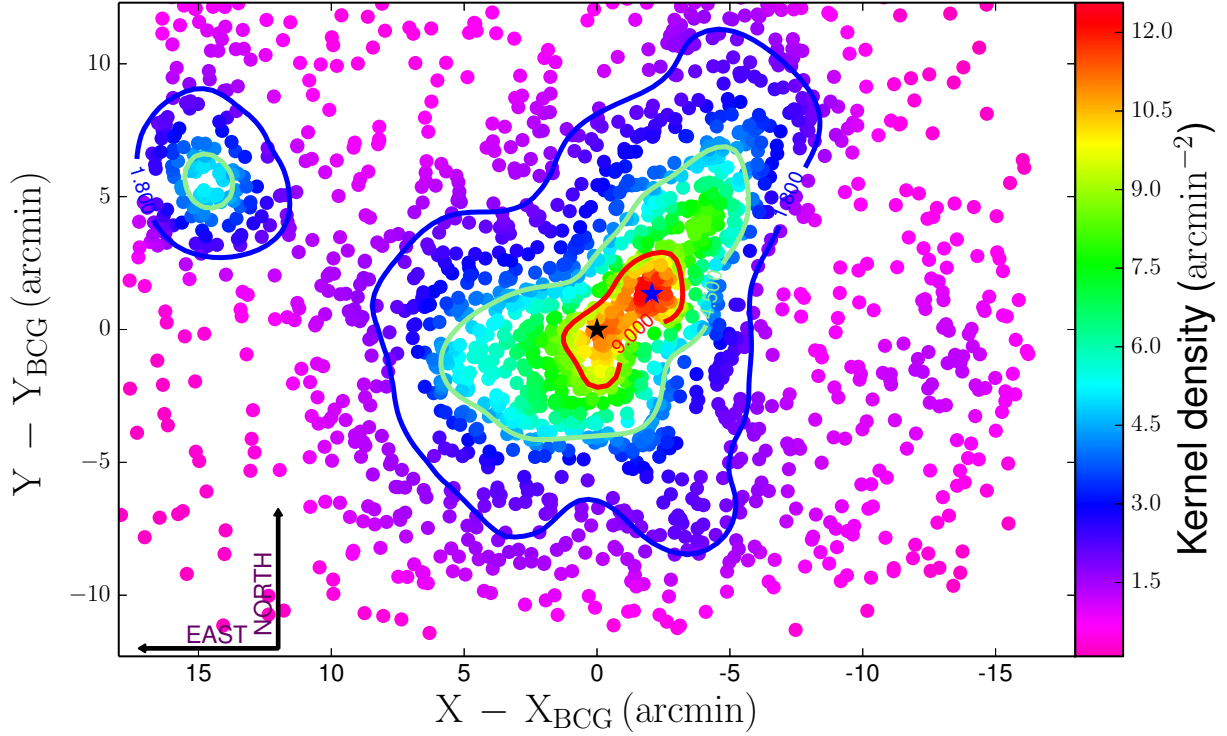


Figure 4.10. Spatial distribution of cluster members down to the stellar mass limit. The points are colored according to the local number density. Coordinates are referred to the position of the BCG (black star). Red, light-green and blue lines identify galaxies belonging to Regions (a), (b) and (c). Points outside the contours belong to Region (d). The blue star represents the position of the highest density peak. 1 arcmin corresponds to 0.21 Mpc at the cluster distance.



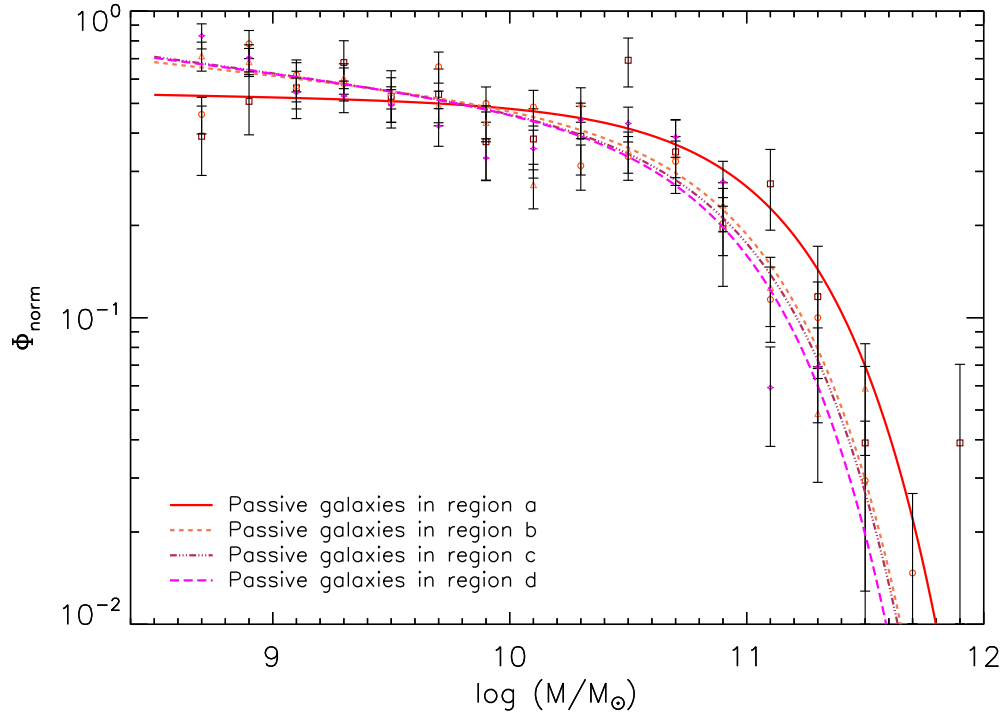


Figure 4.11. SMFs of passive galaxies in different density regions. The SMFs are normalized to the total number of galaxies in each sample. Red circles, orange triangles, maroon squares and magenta diamonds are number counts in Region (a) to (d).

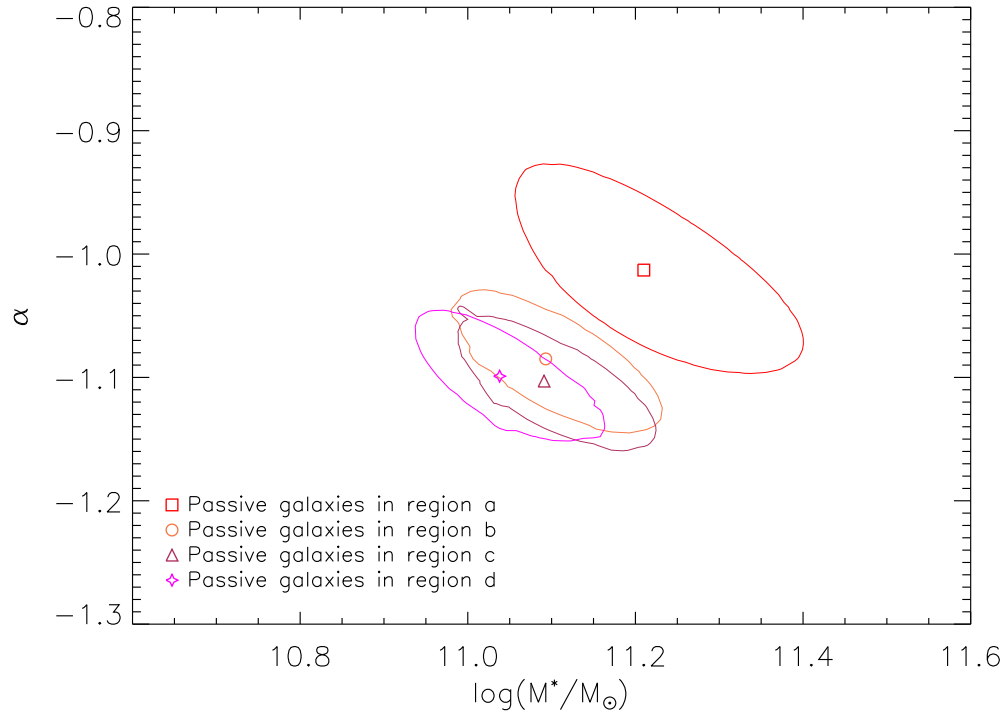


Figure 4.12. As in Fig. 4.7: best-fit Schechter parameters  $M^*$  and  $\alpha$  with their  $1\sigma$  contour in different density regions of the cluster.

### 4.3.3 Double Schechter

Even if the single Schechter is statistically an acceptable fit to all the SMFs presented in this paper, the dip existing in the number counts of passive galaxies in all environment and the upturn in the number counts at the low-mass end visible in the low density regions seem to indicate that perhaps a double Schechter function is more suitable to describe the SMF of this galaxy population. For this reason I fit a double Schechter function to the SMF of passive galaxies in all the environments. The double Schechter function used has four free parameters as in Eq. 3.2. Compared to the single Schechter function there are two additional free parameters: the slope of the second component  $\alpha_2$ , and the ratio between the normalizations of the two functions,  $f_2 = \Phi_2^*/\Phi^*$ . I consider the same  $M^*$  for the two functions to minimize the number of free parameters and to follow the approach already used for the study of the SMF of field galaxies (Mortlock et al., 2015; Baldry et al., 2012). Fig. 4.13 shows the double Schechter fit to the SMF of passive galaxies within and outside the virial radius of the cluster, while Fig. 4.14 shows the double Schechter fit in Regions (a) to (d). The best-fit values of the parameters are listed in Tab. 4.5. From both Fig. 4.14 and Tab. 4.5, one can note that in the most dense region of the cluster the slope of the two Schechter functions are statistically indistinguishable, meaning that a double Schechter function does not provide an improved fit with respect to a single one. The evidence of two populations of passive galaxies becomes stronger when moving to outer and less dense regions of the cluster. This is also shown by the increase of the difference between the two slopes of the Schechter functions. The second component in the SMF of passive galaxies is hypothesized in the model of Peng et al. (2010b), as a result of the environmental quenching of SF galaxies. The fact that the second component is stronger in the outer regions could mean that the environmental processes responsible for the quenching are most effective in external regions of the cluster or that in the center these mechanisms are so strong to completely destroy this population of galaxies.

Fig. 4.15 shows the parameters of the SMF of passive galaxies as a function of the local density of the cluster. The lower of panel Fig. 4.15 shows also the ratio between the number of giant and subgiant galaxies (GSNR) as a function of the environment. I divide the giant and subgiant galaxies using a mass threshold of  $10^{10.0} M_\odot$ , i.e. the mass value at which the SMFs of passive galaxies in region (a) and (b) intersect. The trend in the GSNR shows that in region (a) the ratio between the number of giant and subgiant galaxies is higher than in less dense regions. This trend is consistent with the one found in M1206.

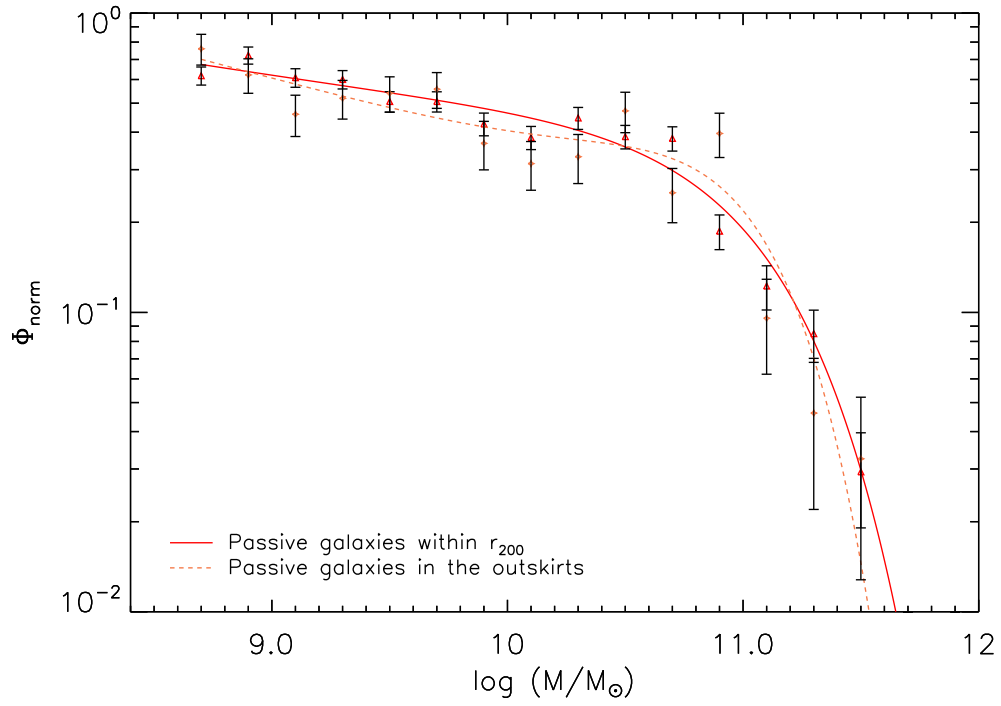


Figure 4.13. SMF of passive cluster member galaxies within and outside  $r_{200}$ . The red solid and orange dashed lines are the best-fit double Schechter functions. The points and the relative errorbars have the same meaning as in Fig. 4.8 (right panel)

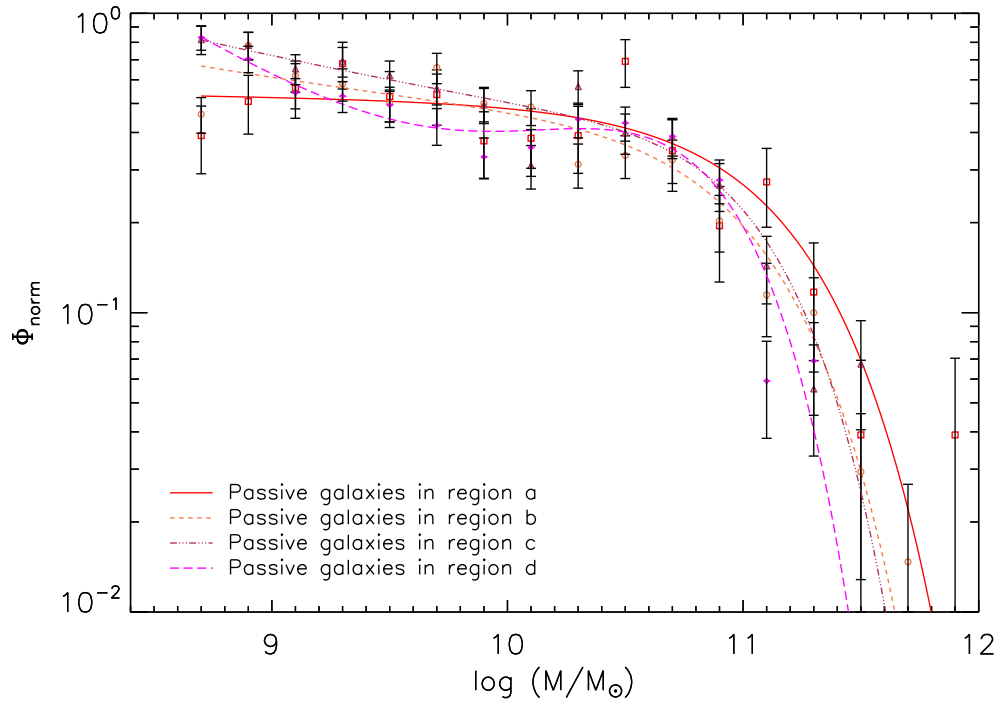


Figure 4.14. SMFs of passive cluster member galaxies in Regions (a) to (d). The lines are the best-fit double Schechter functions. The points and the relative errorbars have the same meaning as in Fig. 4.11.

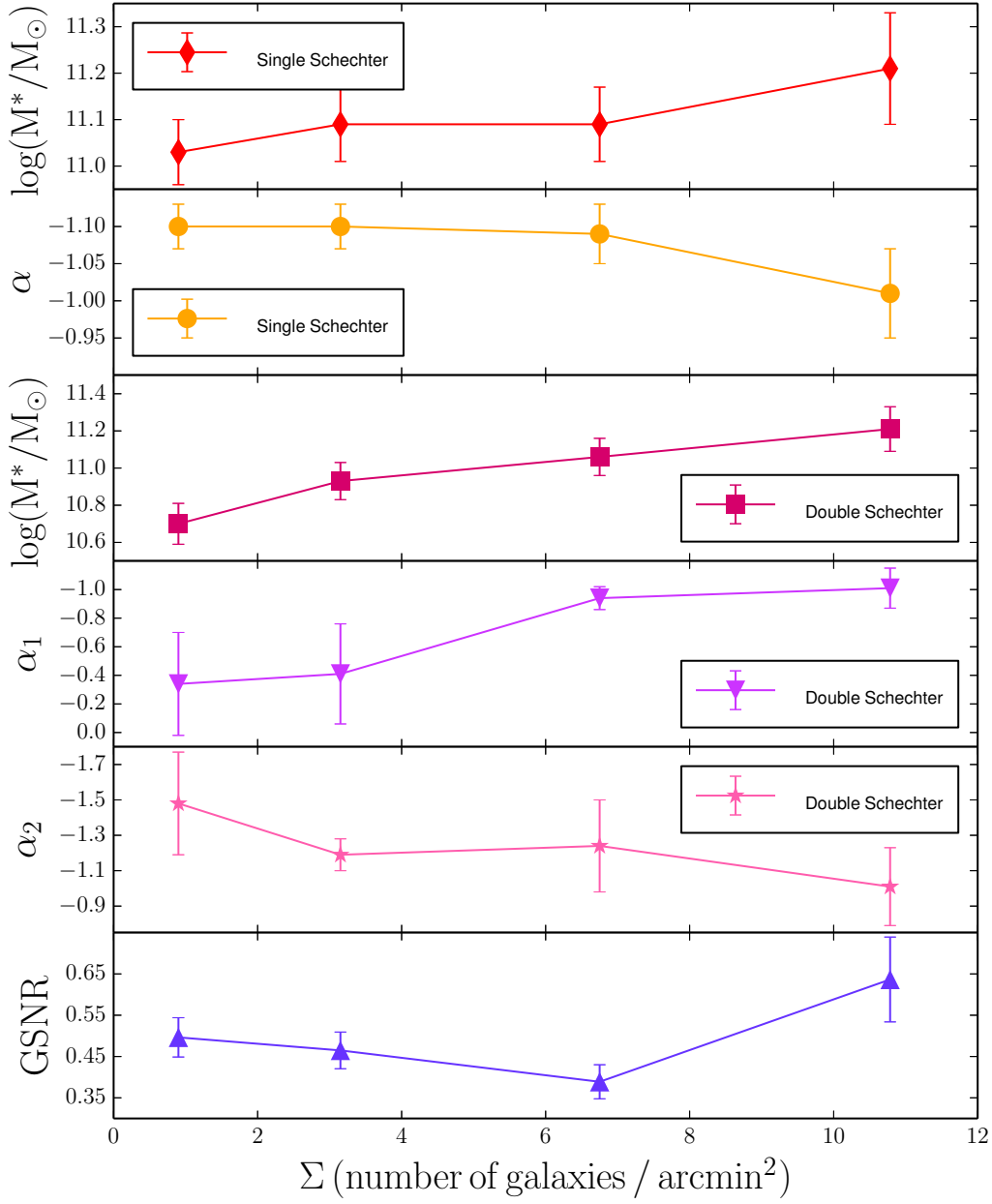


Figure 4.15. From top to bottom: best-fit parameters of the single Schechter (panels 1-2) and of the double Schechter functions (panels 3-5) for passive galaxies and the GSNR (panel 6) as a function of the cluster local number density. Regions (d) to (a) from left to right.

Table 4.5. Best-fit parameters of the double Schechter function of passive galaxies in all environments.

Environment	$\alpha$	$\log(M^*/M_\odot)$	$f_2$	$\alpha_2$
Passive	$-0.61 \pm 0.25$	$10.96 \pm 0.08$	$0.76 \pm 0.25$	$-1.18 \pm 0.23$
$r \leq r_{200}$	$-0.93 \pm 0.27$	$11.08 \pm 0.07$	$0.76 \pm 0.33$	$-1.18 \pm 0.28$
$r > r_{200}$	$-0.05 \pm 0.34$	$10.77 \pm 0.10$	$0.44 \pm 0.25$	$-1.21 \pm 0.10$
Region (a)	$-1.01 \pm 0.14$	$11.21 \pm 0.12$	$0.65 \pm 0.41$	$-1.01 \pm 0.22$
Region (b)	$-0.94 \pm 0.08$	$11.06 \pm 0.10$	$0.34 \pm 0.35$	$-1.24 \pm 0.26$
Region (c)	$-0.41 \pm 0.35$	$10.93 \pm 0.10$	$0.81 \pm 0.32$	$-1.19 \pm 0.09$
Region (d)	$-0.34 \pm 0.36$	$10.70 \pm 0.11$	$0.10 \pm 0.23$	$-1.48 \pm 0.29$

## 4.4 The Intra-cluster light

In the cluster M1206, I found that the SMF of passive galaxies in the innermost and most dense region of the cluster declines at the low-mass end (see Sect. 3.3.2). I suggested that this steeper drop could be explained by the tidal stripping of subgiant galaxies ( $M_\star < 10^{10.5} M_\odot$ ). In our scenario, the material stripped by these galaxies could contribute to the ICL. To check if this hypothesis holds also in this cluster I need to obtain an ICL map and an estimate of the ICL color and mass.

The “intra-cluster light” (ICL) is a diffuse component which is thought to originate from stars bound to the cluster potential that are tidally stripped from the outer regions of galaxies that interact with the BCG or other cluster members (Murante et al. 2007a, Contini et al. 2014a). Some properties of the ICL, such as the radial profile, the color, and presence of substructure are strictly linked to the accretion history and dynamical evolution of galaxy clusters. For example, the presence of tidal arcs can give information on the assembly history of the cluster. If the ICL is formed before the cluster has undergone virialization, the bulk of the ICL will be smooth with few faint tidal arcs. According to theoretical models these features are the result of recent interaction among galaxies with the cluster potential (Rudick et al. 2009). The color can also give some hints on which are the main progenitor galaxies of the ICL. Even if the ICL can shed light on many mechanisms occurring in galaxy clusters, it has proved very hard to study it due to its very faint surface brightness, i.e.  $\sim 1\%$  of the sky brightness. Furthermore, the detection of the ICL at high redshift is made even more difficult by the surface brightness dimming, that scales with redshift as  $(1+z)^4$ .

To obtain the ICL map I follow the method developed by Presotto et al. (2014). In the following sections, I summarize the main aspects of this method.

#### 4.4.1 ICL detection method

There is no consensus on the method for the detection of the ICL. Ideally, one should subtract the light contribution from all galaxies in the cluster including the BCG. However, it is not always possible to perfectly fit the light distribution of each galaxy. For this reason, in many works the galaxies are masked down to a certain limit in surface brightness. The approach I use is a hybrid method which first fits a Sérsic profile to each galaxy and subtracts the best-fit model whenever it is possible, then it masks all the pixels with high residuals. I apply this method to analyze the  $R_c$  image of the cluster. Since the region interested by the ICL is  $\sim 500 \text{ kpc}$  around the BCG, I limit this analysis to a squared image of size  $\sim 1 \text{ Mpc}$  centered on the BCG. I use an automated procedure which relies on GALAPAGOS, GALtoICL presented in [Presotto et al. \(2014\)](#). This procedure merges the stamps created by GALAPAGOS to form a global model image which is later subtracted to the original one to obtain a residual image called BCG+ICL map. The sources that have high residuals are identified by comparing the distribution of the residuals with the distribution of the pixel values of a sky region. The pixels whose values deviate at different  $\sigma$  levels from the sky (1, 2, 3, 4, 5  $\sigma_{sky}$ ) are flagged and associated to the corresponding source. These pixels can be masked or one can decide to manually re-fit the sources to which they belong. Before the BCG+ICL map is created one can also decide to manually add masks (for example in case of stellar spikes).

Fig. 4.16, shows the  $R_c$  image of A209 (first panel), the global model image (second panel) and the BCG+ICL map with pixels at  $1 \sigma_{sky}$  level (third panel). I could check if the subtraction of the light from the sources was done in an efficient way by counting the percentage of masked pixels. In this case this percentage varies from 7% to 10% if I mask at  $5 \sigma_{sky}$  or  $1 \sigma_{sky}$ .

#### 4.4.2 ICL properties

To estimate the  $B - R_c$  color of the BCG+ICL map I take as a benchmark the global model in the  $R_c$  band. From this I obtain a model for the B band by changing the zeropoint and fitting only the magnitudes of the objects. Then, I subtract this model from the B-band image of the cluster to get the B band BCG+ICL map. At this point, I degrade the BCG+ICL map in the  $R_c$  band to the PSF of the B band by convolving it with a Gaussian function whose  $\sigma$  is the difference between the two PSFs and from this I subtract the B band BCG+ICL map. The  $B - R_c$  color of the BCG+ICL is  $\sim 2.1 \text{ mag}$  at the position of the BCG while it drops to  $1.2 \text{ mag}$  at a distance from the BCG of  $\sim 110 \text{ kpc}$ . In this radial range, the color of the BCG+ICL remains in the color range of the passive cluster members (see Fig. 4.5).

The surface brightness profile of BCG+ICL deviates from a single Sérsic profile ([Presotto](#)



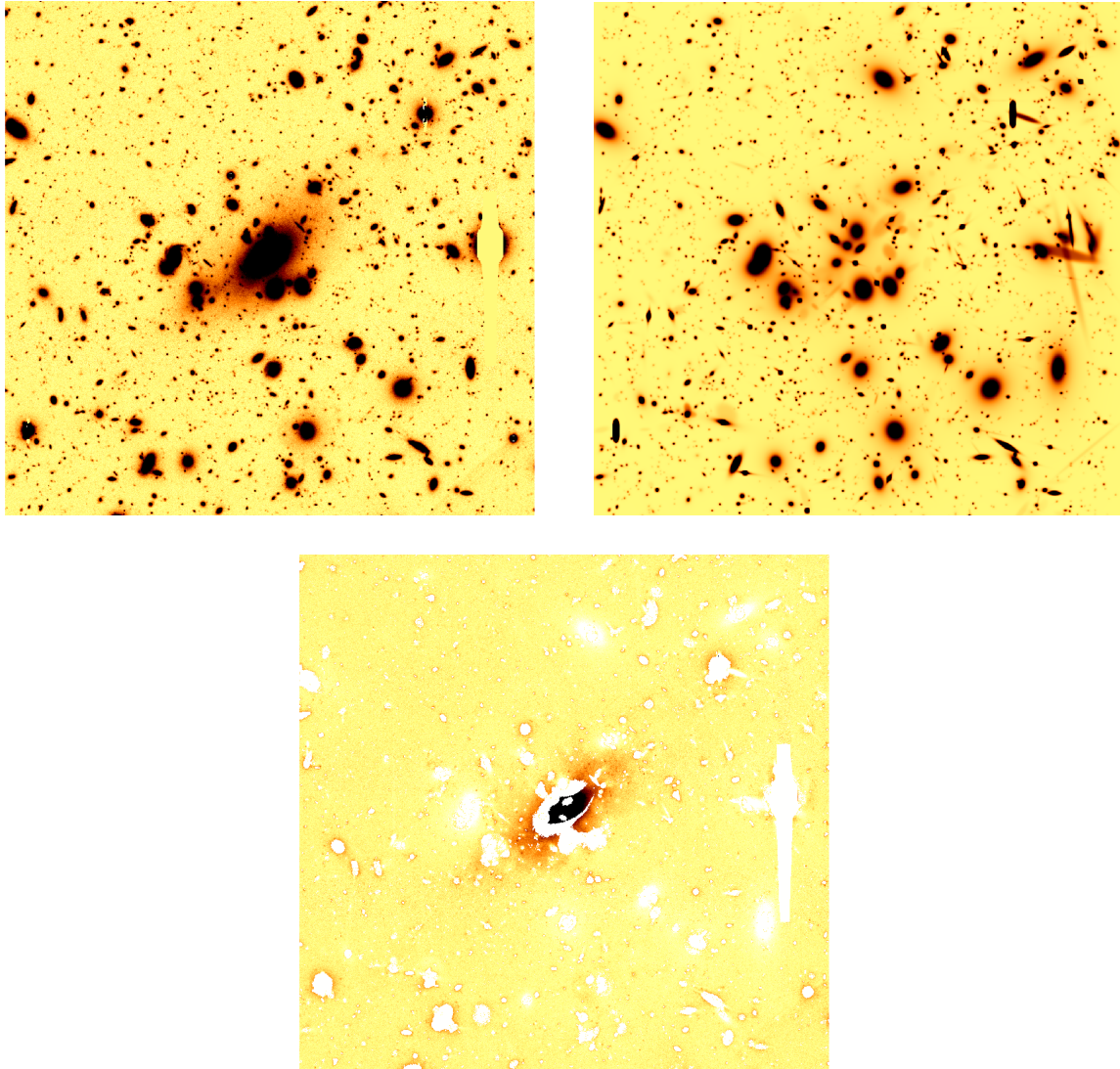


Figure 4.16. SuprimeCam image in the Rc band of A209 (top left panel), the global model image (top right panel) and the BCG+ICL map with pixels at  $1\sigma_{sky}$  level (bottom panel). The images are  $\sim 5$  arcmin for each side corresponding to 1 Mpc at the cluster redshift.

et al. 2014). For this reason I fit the BCG+ICL light profile with a sum of multiple components. Moustakas et al. (in prep.) model the surface brightness profile of the BCGs of each CLASH cluster. They find that, contrary to the other BCGs in the sample, the light profile of the BCG of A209 deviates from a single Sérsic profile. They perform the fits in all HST bandpasses and assume an universal value of  $n$  and  $r_e$ . I choose to fit the BCG+ICL profile with three components: two components for the BCGs with the effective radius ( $r_e$ ) and the Sérsic index fixed to the values found in Moustakas et al., and another one for the ICL. The best-fit parameters for the three component are listed in Tab 4.6. The reduced  $\chi^2$  of the fit is 1.535.

Component	$r_e$ ( $h_{70}^{-1} \text{ kpc}$ )	$n$	$mag_{tot}$ (AB mag)
1 (BCG)	0.86	0.5	20.07
2 (BCG)	44.28	3.07	16.15
3 (ICL)	120	1.51	16.57

Table 4.6. Best-fit parameters of the three component of the Sérsic fit of the BCG+ICL.

I used the magnitude value obtained from the fit to estimate the ICL mass. the stellar masses of red cluster member galaxies which are in the subsample image analyzed with GALAPAGOS and their total Rc magnitude provided by GALFIT:

$$\log(M/M_{\odot}) = (18.41 \pm 0.07) - (0.41 \pm 0.02) \times Rc_{totmag}. \quad (4.1)$$

Using this relation with the total Rc magnitudes obtained from the multicomponent Sérsic fit, I estimate  $M_{ICL} = (2.9 \pm 0.7) \times 10^{11} M_{\odot}$  and  $M_{BCG} = (6.2 \pm 1.2) \times 10^{11} M_{\odot}$ . The mass of the BCG obtained in this way is identical to the mass obtained applying MAGPHYS, i.e.  $6.2 \pm 1.2 \times 10^{11} M_{\odot}$ .

To check if the ICL can form from tidal stripping of subgiants galaxies (i.e. galaxies with  $M_{\star} < 10^{10.0} M_{\odot}$ ), I have to evaluate the missing mass from subgiant galaxies in Region (a). I use Equation 3.4, by substituting the extremes of the integral with the mass limit that is reached in this case ( $\sim 10^{8.6} M_{\odot}$ ) and the value at which the SMFs of passive galaxies in Regions (a) and (b) intersect each other ( $\sim 10^{10.0} M_{\odot}$ ). The upper and lower error on  $\Delta M_{sub}$  are estimated by repeating the evaluation of Eq. 3.4 and fixing the slope to  $\alpha \pm \delta\alpha$ . The value of  $\Delta M_{sub}$  is  $1.4_{-0.7}^{+0.5} \times 10^{11} M_{\odot}$ . The value of  $\Delta M_{sub}$  is formally in agreement with  $M_{ICL}$  within  $1\sigma$ . A similar agreement between  $\Delta M_{sub}$  and  $M_{ICL}$  was also found in M1206.

Breaking the integral in Eq. 3.4 I can estimate the contribution to  $\Delta M_{sub}$  coming from galaxies in different mass ranges: the main contribution is given by galaxies in the mass range  $10^{9.5} < M_{\star} < 10^{10.0} M_{\odot}$  (60%), galaxies in the mass range  $10^{9.0} < M_{\star} < 10^{9.5} M_{\odot}$  contribute for  $\sim 30\%$ , while galaxies in the range  $10^{8.6} < M_{\star} < 10^{9.0} M_{\odot}$  only for 10%. This suggests that the ICL could originate from stripping of stars from subgiant galaxies in the mass range  $10^{9.0} < M_{\star} < 10^{10.0} M_{\odot}$ . On the contrary, this result seems to rule out that the disruption of dwarf galaxies is the main channel for the formation of ICL, in agreement with the predictions from semi-analytical models (Contini et al. 2014a). The result presented here is also consistent with recent findings from observational works. In detail, DeMaio et al. (2015), use a subsample of CLASH clusters at  $0.44 \leq z \leq 0.57$  to determine the color gradients and total luminosity of the ICL. Their main conclusion is that the ICL originates from the tidal destruction of  $0.2L^*$  galaxies (which corresponds to galaxies of  $\sim 10^{10.0} M_{\odot}$ ). In a completely independent way, Longobardi et al. (2015) assess that the Planetary Nebulae in the Intra-cluster medium of Virgo cluster can be associated to galaxy progenitor of mass around four times the mass of the Large Magellanic Cloud ( $\sim 10^{9.5} M_{\odot}$ ).

## 4.5 Orbits of passive galaxies

To investigate further the evolution of galaxies in A209, I carry out the dynamical analysis of the orbits of passive galaxies. The mass profile of A209 has been determined from gravitational lensing by Merten et al. (2014). Parametrized with a NFW profile (Navarro et al., 1997a), it is characterized by a concentration  $c_{200} = 3.3 \pm 0.9$  and a mass  $M_{200} = (1.4 \pm 0.1) 10^{15} M_{\odot}$ . These values correspond to a NFW scale and virial radius of  $r_{-2} = 0.6 \pm 0.2$  Mpc and  $r_{200} = 2.1 \pm 0.05$  Mpc, respectively. Given this mass profile, it is possible to invert the Jeans equation for the dynamical equilibrium (Binney and Tremaine, 1987) to determine the orbits of different populations of cluster galaxies (Binney and Mamon, 1982). The orbits are described by the velocity anisotropy profile

$$\beta(r) = 1 - \frac{\sigma_{\theta}^2(r) + \sigma_{\phi}^2(r)}{2\sigma_r^2(r)} = 1 - \frac{\sigma_{\theta}^2(r)}{\sigma_r^2(r)}, \quad (4.2)$$

where  $\sigma_{\theta}, \sigma_{\phi}$  are the two tangential components, and  $\sigma_r$  the radial component, of the velocity dispersion, and the last equivalence is valid when both the density and the velocity structures of the cluster are invariant under rotations about its center, i.e. the cluster does not rotate.

I determine  $\beta(r)$  by solving the equations in Solanes and Salvador-Solé (1990), with the technique of Biviano et al. (2013). The error bars are determined by a bootstrap procedure, running the inversion on 100 extractions from the original data set.

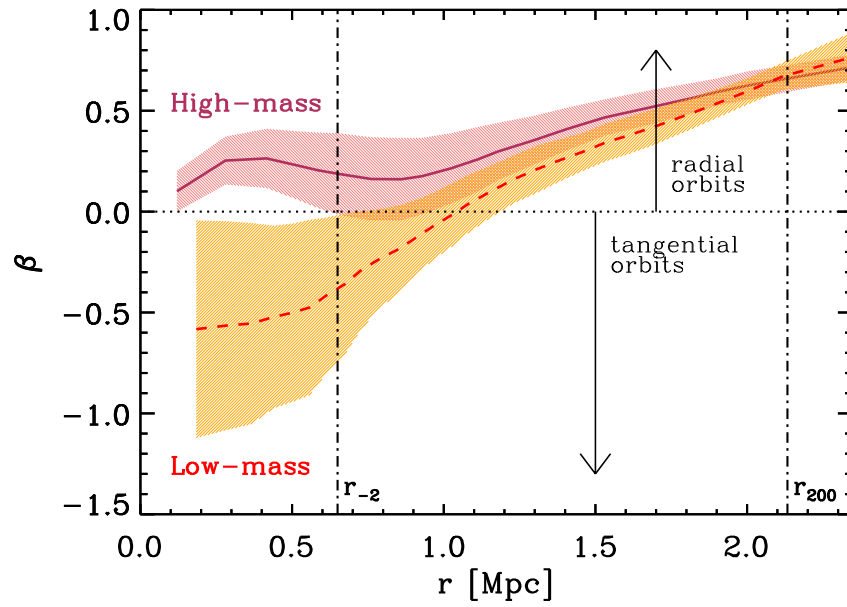


Figure 4.17. The maroon solid and red dashed curves represent the velocity anisotropy profiles  $\beta(r)$  of the high- and low- $M_\star$  subsamples of passive cluster galaxies (above and below  $10^{10.0} M_\odot$ ). The shaded regions represents the corresponding 68% confidence levels. The vertical lines indicate the positions of  $r_{-2}$  (dashed) and  $r_{200}$  (dash-dotted).

I determine  $\beta(r)$  separately for two subsamples of passive galaxies, with  $M_\star < 10^{10.0} M_\odot$ , and, respectively,  $M_\star \geq 10^{10.0} M_\odot$ . The results are shown in Fig. 4.17, the solid/dashed curves corresponding to the high-/low-mass subsample, respectively. The two profiles look similar at radii  $r > r_{-2}$ , but they differ in the inner region. The  $\beta(r)$  of high-mass galaxies is similar to that seen in other clusters (e.g. Biviano et al., 2013) and also in simulated halos (e.g. Munari et al., 2013). The  $\beta(r)$  profile of low-mass galaxies indicates tangential orbits within  $r_{-2}$ . This might occur as a result of selective destruction of low-mass galaxies on radial orbits near the cluster center. Radial orbits are characterized by small pericenters and only the more massive galaxies might be able to survive the very hostile and dense environment of the central cluster region. Low-mass galaxies which manage to escape destruction (e.g. by tidal forces) near the cluster center might be those that avoid passing very close to the cluster center by moving on slightly tangential orbits.

## 4.6 Mass-size relation

To estimate the size of each cluster member down to the mass limit of the sample, I use the GALAPAGOS software described in Sect. 4.4.1 applied to the R-band image. The size of each galaxy is identified by the effective radius of the single Sérsic fit performed by GALAPAGOS. The core of Abell 209 was observed with HST, as part of the CLASH program, in 16 broadband filters from UV to near-IR, using WFC3/UVIS, ACS/WFC, and WFC3/IR. Moreover two parallel fields  $\sim 1.28$  Mpc far from the cluster core were observed with ACS/WFC and WFC3/IR with filters F850LP and F160, respectively. The images were reduced using standard techniques, and then co-aligned and combined using drizzle algorithms to a pixel scale of 0.065 arcsec (for details, see Koekemoer et al. 2007, 2011). In order to check for the reliability of the sizes I applied GALAPAGOS also on the HST image of the cluster in the F850LP band. The median difference in the estimation of the size for those galaxies in both the Subaru and the HST field is 0.06 arcsec (0.2 kpc).

For the analysis of the size distribution, I use the photometric sample of galaxies defined as passive ( $sSFR < 10^{-10} \text{ yr}^{-1}$ ) and early-type ( $n_{\text{Sérsic}} > 2.5$ , Shen et al. 2003). In order to assess the goodness of the photometric classification in passive and SF galaxies on the basis of their  $sSFR$  and in early- and late-type on the basis of their Sérsic index, I take advantage of the spectroscopic sample. I divide the galaxies of the spectroscopic sample in different spectral classes using the method described in Girardi et al. (2015). Following this classification, I divide the Emission Line Galaxies (ELGs) in weak (wELG), medium (mELG), strong (sELG) and very strong (vsELG), according to the EW[OII]. Non-emission line galaxies are divided in post-starburst, if they have  $\text{EW}[\text{H}\delta] > 3\text{\AA}$  (HDS), and in Passive (hereafter PAS). In this classification I consider only galaxies with  $S/N > 5$  for each pixel in the region of the

spectrum around the  $H\delta$  line. At the mass limit of  $10^{8.6} M_{\odot}$  I have the spectroscopic classification for 741 galaxies. This spectroscopic classification is used to assess the goodness of the photometric classification in passive and SF galaxies on the basis of their sSFR (see Sect. 4.2). Among the different spectroscopic classes, 99.4% of passive galaxies have sSFR  $< 10^{-10} \text{ yr}^{-1}$ , hence identified as passive also photometrically, and 92% of the galaxies with equivalent width of the [OII] emission line  $\geq 15 \text{ \AA}$ , are classified as SF on the basis of their sSFR ( $> 10^{-10} \text{ yr}^{-1}$ ). The other ELGs are classified partially as SF and partially as passive with a mean sSFR of  $\sim 10^{-10.5} \text{ yr}^{-1}$  for wELGs and  $\sim 10^{-10.1} \text{ yr}^{-1}$  for mELGs. In first approximation, one can safely use the sSFR value to discriminate between SF and passive galaxies. The spectroscopic sample is also used to test the morphological classification in early- and late-type galaxies on the basis of their Sérsic index ( $n > 2.5$  for early-type galaxies, hereafter ETGs). Of the total sample of galaxies with spectroscopic classification, 568 are ETGs ( $n > 2.5$ ). Among them, 78% are PAS galaxies, 12.5% are wELGs and 7% are HDS galaxies. Following the approach already used for the orbital analysis, I divide the sample in low and high-mass galaxies with a threshold value  $10^{10} M_{\odot}$ , and, then, I further split these two sub-samples inside and outside  $r_{-2}$ , to investigate possible environmental effects on the mass-size relation. Fig. 4.18 shows the stacked spectra of ETGs belonging to the four sub-samples defined above, which appear rather similar. By using the software pPXF (Cappellari and Emsellem 2004) and MILES models (Vazdekis et al. 2010) I obtain that galaxies host old stellar populations with ages in the range  $8.0 \pm 1.0 \text{ Gyr}$  in the four bins. Galaxies with  $M > 10^{10} M_{\odot}$  are consistent with solar metallicities, whereas low-mass galaxies with sub-solar metallicities. In order to use a sample with as little contamination as possible, I choose to use for the mass-size analysis the photometric sample of passive (according to their sSFR) and early-type galaxies. Firstly, I fit the following linear relation to our data:

$$\log(Re [\text{kpc}]) = a + b \times \log(M/M_{\odot}), \quad (4.3)$$

separately for low-mass and high mass sub-samples. The fits are performed using the python code *lts\_linefit.py* (Cappellari et al., 2013). This code performs robust linear fit to data with errors in both variables. The results of the fits are shown in Fig. 4.19. I compare the results obtained for the high-mass sample with the mass-size relation for galaxies in the field provided in two different works (Shen et al. 2003 and van der Wel et al. 2014b), respectively magenta and cyan line in the lower panel of Fig. 4.19. van der Wel et al. (2014b) divide their sample of field data into early- and late-type galaxies according to their rest-frame colors. Their selection corresponds to our classification in passive and SF galaxies according to the sSFR. The best-fit parameters of the mass-size relation provided here are in agreement at  $1\sigma$  level with those in van der Wel et al. (2014b) for ETGs at similar redshift. In this analysis I am not using circularized radii, defined as:

$$Re_{\text{circ}} = Re \times \sqrt{q}, \quad (4.4)$$



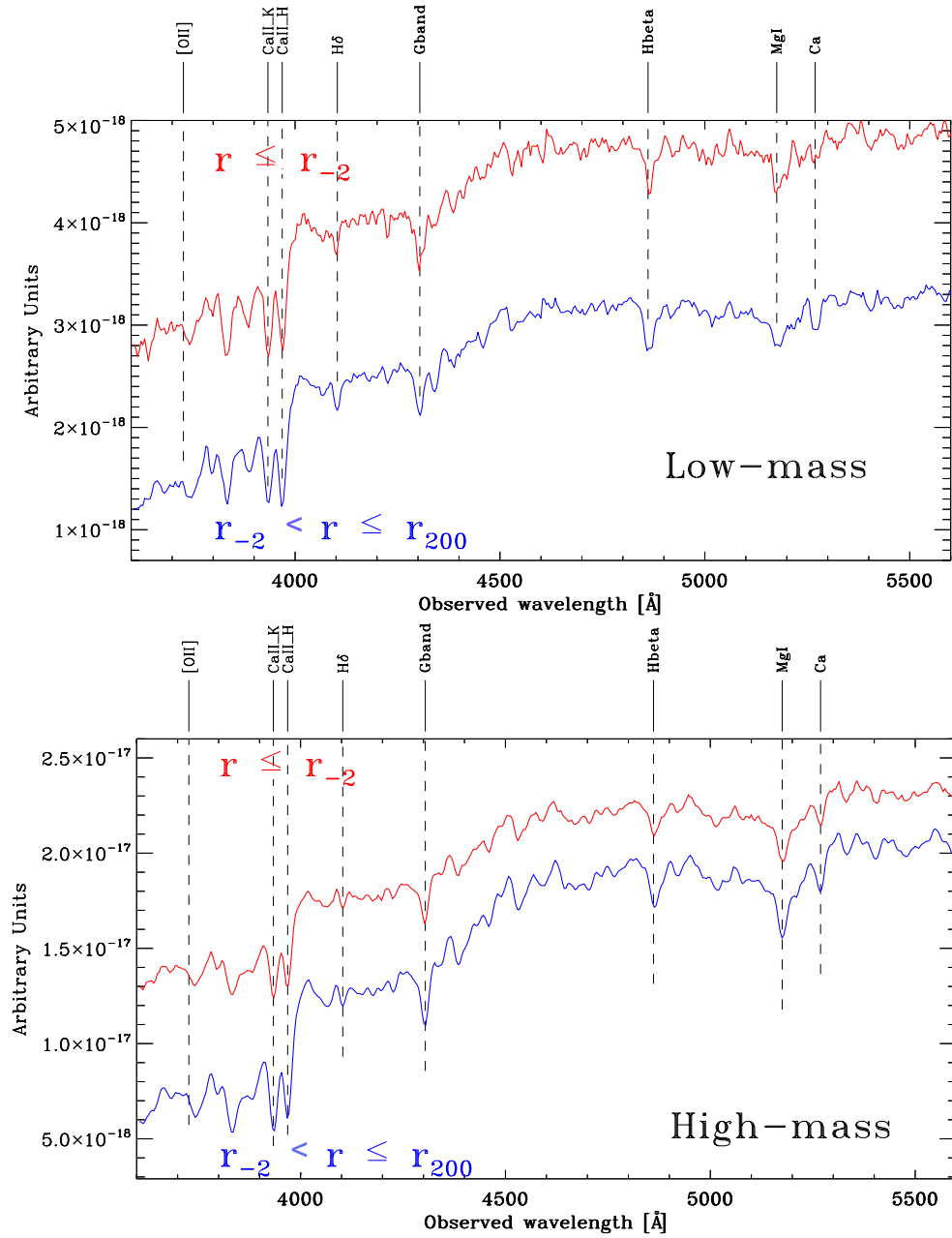


Figure 4.18. Stacked spectra of ETGs for low-mass ( $\leq 10^{10.0} M_{\odot}$ , upper panel) and high-mass ( $> 10^{10.0} M_{\odot}$ , lower panel) galaxies in the internal (red) and external (blue)  $r_{-2} = 0.65$  Mpc.

where  $Re$  is the effective radius and  $q$  is the axis ratio of the single Sérsic fit performed by GALAPAGOS, to better compare our results with those of [van der Wel et al. \(2014b\)](#). However, performing the fit using the circularized radii changes very little the values of the parameters ( $a_{circ} = -8.1 \pm 0.7$ ,  $b_{circ} = 0.79 \pm 0.07$ ).

The slope of the relation between stellar mass and galaxy size is very different in the two range of stellar mass. In particular, for low-mass galaxies the slope of the relation is flatter than for high-mass galaxies, in agreement also with the suggestions from [van der Wel et al. \(2014b\)](#). Moreover, the value of the slope obtained for low-mass passive and ETGs is in agreement (within  $1\sigma$ ) with the slope of the mass-size relation presented for late-type galaxies in [van der Wel et al. \(2014b\)](#) (see upper panel of Fig. 4.19).

In order to investigate the effect of the environment on the mass-size relation, I consider separately the galaxies inside and outside  $r_{-2}$  (defined in Sect. 4.5), analyzing the distribution of the residuals with respect to the two relations obtained for low-mass and high-mass galaxies. The distribution of the residuals of low-mass galaxies within  $r_{-2}$  is centered on negative values. The median value of  $\Delta Re \equiv \log(Re) - \log(Re_{bf})$  is  $-0.12 \pm 0.05$ . For low-mass galaxies with  $r_{-2} \leq r \leq r_{200}$ , instead,  $\Delta Re = 0.10 \pm 0.03$ . In order to statistically assess this discrepancy I apply the K-S test to the distributions of the residuals of low-mass galaxies within and outside  $r_{-2}$ . The resulting K-S probability is 0.4% which implies that the two distributions are statistically different. This result seems to indicate that at fixed stellar mass the size of low-mass galaxies in the center of the cluster are smaller than in more external regions.

The same test applied to the sample of high-mass galaxies confirms that the distribution of galaxy sizes are indistinguishable in the two regions.

The fact that the slope of the mass-size relation of low-mass passive early-type galaxies is consistent with that derived by [van der Wel et al. \(2014b\)](#) for field star-forming galaxies is compatible with the scenario that low mass galaxies originate from quenching of late-type galaxies. The quenching mechanism could be responsible not only for the truncation of the star formation but also for a change in the morphology of the object. The interpretation of the environmental dependence of the mass-size relation is more puzzling. According to the analysis of the orbits, low-mass galaxies tend to have tangential orbits, hence avoiding the cluster center (coincident with the position of the BCG). A possible scenario could be that when low-mass galaxies pass very close to the cluster center, they are destroyed or stripped below the mass limit. However, galaxies that are not close enough to the BCG to be destroyed still undergo tidal interactions that could reduce their size.



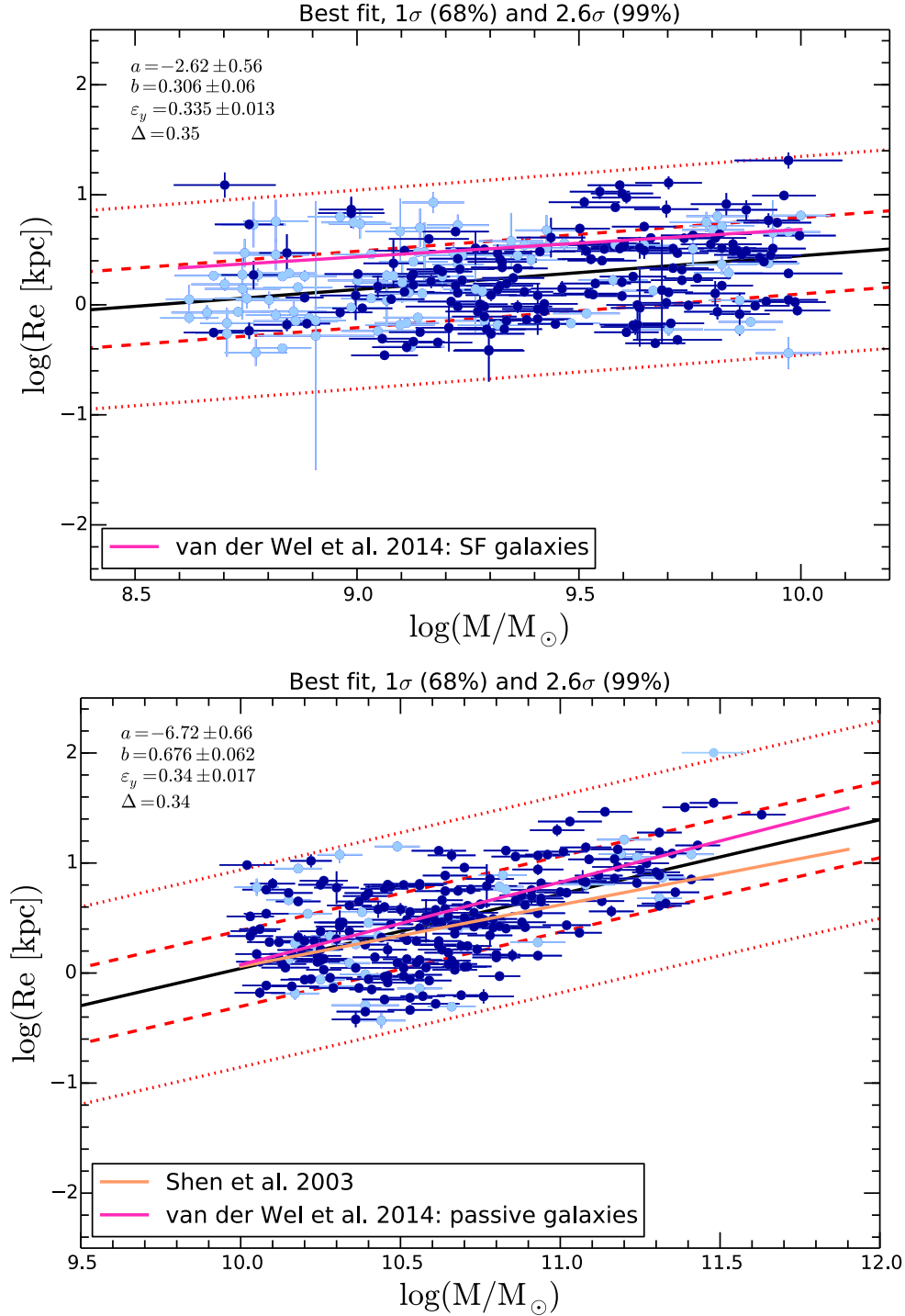


Figure 4.19. Best-fit of the mass-size relation in Eq. 4.3 for early-type passive low-mass galaxies ( $M_\star \leq 10^{10} M_\odot$ ) (upper panel) and high-mass galaxies ( $M_\star > 10^{10} M_\odot$ ). The best-fit values of the two parameters  $a$  and  $b$  with their  $1\sigma$  uncertainty, are reported on the two panels. Dark blue points identify spectroscopic members, while light blue point are photometric members.

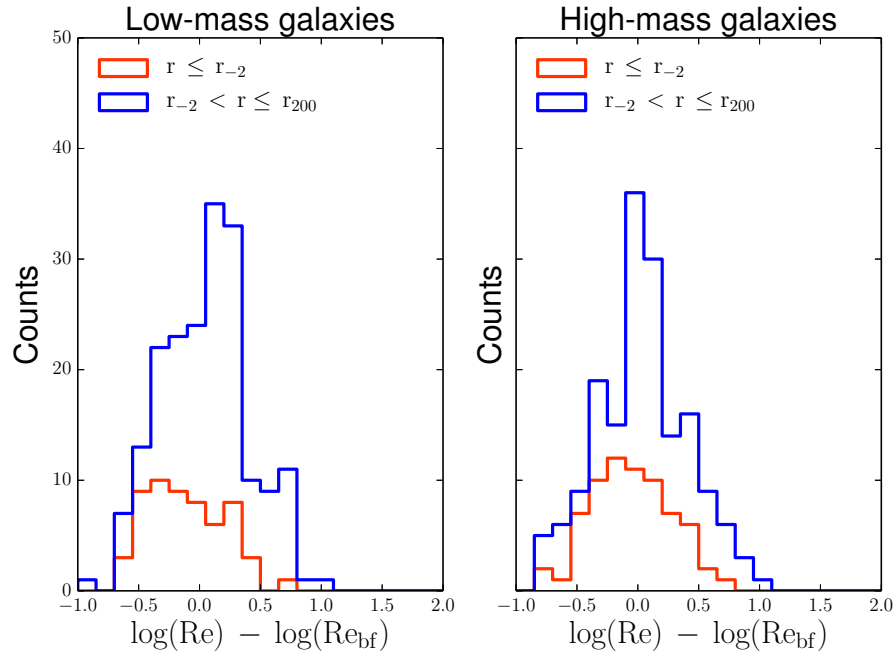


Figure 4.20. Distribution of effective radius residuals with respect to the best-fit relation (Eq. 4.3) for low-mass (left panel) and high-mass (right panel) galaxies in the internal (red) and external (blue) region of the cluster.

## 4.7 The stellar mass density profile

To investigate further the environmental processes active in this cluster, I study also the number density, and the stellar and total mass density profiles. I use the sample of 1916 member galaxies with  $M_{\star} \geq 10^{8.6} M_{\odot}$  to determine the number density ( $N(R)$ ) and the stellar mass density ( $\Sigma_{\star}(R)$ ) radial profiles. For the determination of the number density profile, I use the same weights used for the SMF and described in Sect. 2.4.3, while for the determination of  $\Sigma_{\star}(R)$  these weights are multiplied by the galaxy stellar masses.

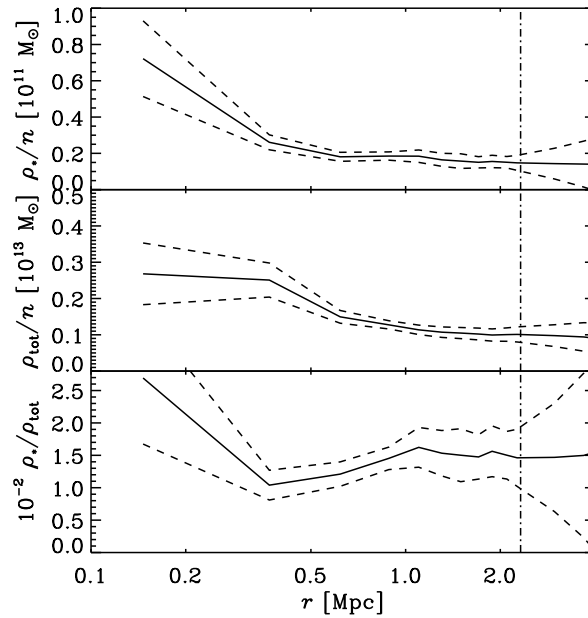


Figure 4.21. Top panel: the ratio of the deprojected stellar mass density and number density profiles. Middle panel: the ratio of the total mass density and number density profiles. Bottom panel: the ratio of the stellar mass density and total mass density profiles. Dashed lines indicate  $1\sigma$  confidence regions. All densities are volume densities. The vertical dash-dotted line is the value of  $r_{200}$ .

To best compare the two density profiles, I deproject them with an Abel inversion (Binney and Tremaine 1987). This technique makes the assumption of spherical symmetry. For the inversion I use a smoothed version of the profiles obtained with the LOWESS technique (e.g. Gebhardt et al., 1994), where the extrapolation to infinity is done following Biviano et al. (2013, eq. 10). The first panel of Fig. 4.21 shows the ratio between the deprojected

mass density profile and the number density profile. The  $1\sigma$  confidence levels are obtained by propagation of errors and are represented by the dashed line assuming that the errors on the deprojected profiles are the same as for the projected profiles. The ratio shows a significant peak in the central region of the cluster. This is a striking evidence of a mass segregation effect, meaning that in the central region of the cluster the mean galaxy mass is higher than at larger radii. This is due to the presence of a dozen galaxies, all with masses above  $10^{10} M_{\odot}$ , within  $0.1 Mpc$  from the BCG and is in agreement with the environmental dependence of the SMF.

An indication of the processes that are responsible for this mass segregation can be obtained comparing the mass density profile and the number density profile to the total density profile. For the total density profile ( $\rho_{tot}$ ), I consider the estimate obtained from the gravitational lensing analysis in [Merten et al. \(2014\)](#). The second and third panels of Fig. 4.21 show the ratios  $\rho_{tot}/n$  and  $\rho_{*}/\rho_{tot}$  as function of the 3D clustercentric distance  $r$ . The total mass density is less concentrated than the distribution of galaxies, in agreement with what I found for M1206, and significantly less concentrated than the stellar mass density.

## 4.8 Discussion

### 4.8.1 Environmental dependence of the stellar mass function

I investigate the environmental dependence of the SMF, by examining passive and star-forming galaxies separately. By defining the environment in terms of the local number density of galaxies I find no dependence of the shape of the SMF of SF galaxies on the environment, confirming the results I found at higher redshift in the galaxy cluster M1206. On the other hand, the SMF of passive galaxies depends on the local density, with a higher  $M^*$  and a flatter slope in the densest region, as shown in Fig. 4.11. The higher values of  $M^*$  found in the central region of the cluster could be the result of the dynamical friction processes that are effective in the cluster center, as also confirmed by the analysis of the stellar mass density profile (see below). Moreover, the SMF of passive galaxies is better fitted by a double Schechter function. This suggest the existence of two populations of passive galaxies: one formed by galaxies of high mass, while the other formed by galaxies of low masses ( $M_{*} \leq 10^{9.5} M_{\odot}$ ). In agreement with [Peng et al. \(2010b\)](#), one can interpret the SMF as the combination of the SMF of mass quenched galaxies and the SMF of SF galaxies turned into passive by "environmental quenching".

The "environmental quenching" responsible for the double component of the SMF can be the effect of different mechanisms, like starvation, ram-pressure stripping, galaxy-galaxy collisions and mergers, and harassment. Starvation and ram-pressure stripping affect the gas content of cluster galaxies, leading to a quenching of star formation. Starvation refers

to the stripping of the external gas reservoir of the galaxy (Larson et al., 1980) while ram-pressure strips the galaxy disk gas due to interaction with the hot and dense intra-cluster medium (Gunn and Gott, 1972). Ram-pressure stripping is thought to be effective only in the central cluster region, while starvation can also operate in the cluster outskirts. Galaxy-galaxy collisions and mergers are more likely to be effective in the external cluster regions, where the relative speed of the encounters is not very high (Spitzer and Baade 1951, Negroponte and White 1983). However, the velocity dispersion of A209 remains very high also beyond the virial radius ( $> 700 \text{ km s}^{-1}$ , Sartoris et al in prep.).

Harassment transforms galaxies by multiple high-speed galaxy-galaxy encounters and the interaction with the potential of the cluster as a whole (Moore et al. 1996, 1998, 1999). Moore et al. (1998) showed that harassment has no effect on systems as dense as giant ellipticals or spiral bulges but disk galaxies can be turned into spheroidal. This could induce a loss of Sc or Sd-Im in the LF (at  $\sim 2 \text{ mag}$  below  $L^*$ , Binggeli and Jerjen 1998) and a comparable break in the spheroidal LF that lies  $\sim 4 \text{ mag}$  below  $L^*$ . This would correspond to a dip in the SMF around  $M_\star = 10^{10.0} M_\odot$  and an upturn at  $M_\star \leq 10^{9.0} M_\odot$ , in agreement with our findings in the less dense region of the cluster, suggesting that harassment could be the main driver of galaxy transformations in the external cluster regions. Recent simulations (Smith et al. 2010; Bialas et al. 2015; Smith et al. 2015) indicate that harassment is not very effective for newly infalling galaxies with an orbital apocenter beyond half a virial radius. However, the low-mass passive galaxies in A209 are likely to have completed more than a single orbit. In agreement with our results, Popesso et al. (2006a) show that the  $r$ -band LF of local early-type galaxies requires a double Schechter function, with the faint-end slope having a significant and continuous variation with the environment, flattening in the central region of the cluster. They also interpret these results as an effect of galaxy transformation from star forming to quiescent systems through harassment in the periphery and dwarf tidal disruption in the core.

Analyzing the LFs of cluster galaxies at different epochs, Martinet et al. (2015) find a flatter slope of the red faint end at lower redshift. In agreement with our findings, the authors interpret this evolution of the LF in terms of the quenching of blue star forming galaxies in dense cluster environments to enrich the red-sequence population from high to lower redshift.

Since galaxies experience different cluster environments when moving along their orbits, it is likely that their properties are not affected by just one environmental process. For example, starvation can be effective in quenching the star formation of cluster galaxies even at large distances from the center, and part of the structural transformation could happen by preprocessing in groups before galaxies enter the cluster environment (Balogh et al., 2000).

The evidence for two components in the SMF of red passive galaxies was first discovered in the field by Drory et al. (2009) and has been recently shown at low (Baldry et al. 2012)

and high redshift (Muzzin et al. 2013a; Ilbert et al. 2013; Mortlock et al. 2015). The mass at which the composition of the two populations becomes evident is higher at lower redshifts. At  $z = 1$  the signature of the double Schechter (an upturn of the SMF) is found at  $M_\star \sim 10^{9.0} M_\odot$ , while at  $z = 0$  this transition mass is higher,  $M_\star \sim 10^{10.0} M_\odot$ . According to this scenario, in fact, I did not find any evidence of a double Schechter in the SMF of passive galaxies in the cluster of galaxies M1206. In fact, at this redshift the predicted transition mass is lower than the mass limit of that sample ( $M_\star \sim 10^{9.5} M_\odot$ ). On the other hand, in the most dense region of the cluster, the second component of the SMF of passive galaxies seems to be suppressed, due to a lack of subgiant galaxies. This could be interpreted as the effect of processes responsible for the stripping of both the gas around the galaxies and their stellar content. These processes are probably tidal interactions with the cluster potential.

#### 4.8.2 The origin of the intra-cluster light

By comparing the single Schechter parametrization of the SMF in the central and most dense region of the cluster, with the ones obtained in outer regions, I find that the shape of the SMF of passive galaxies depends on the environment only in the most dense region of the cluster (Region (a)). For M1206, I found that there was a significant change in the slope SMF of passive galaxies in the cluster M1206 in the region corresponding to  $R \leq 0.25 r_{200}$ . This environmental effect observed in M1206 was interpreted in terms of formation of the ICL. In fact, as supported by the analysis of the ICL in that cluster (Presotto et al. 2014), the change in slope in the most dense regions of the cluster might be due to tidal disruption of subgiant galaxies ( $M_\star \leq 10^{10.5} M_\odot$ ) leading to the formation of at least part of the ICL (see Chapter 3). This scenario is supported also in A209 by the evaluation of the missing mass from subgiant galaxies ( $\Delta M_{sub}$ ) by the comparison with the ICL mass (Sect. 4.4.2). According to the evaluation of the integral in Eq. 3.4, one of the main channel of formation of the ICL is the disruption of passive galaxies in the mass range  $10^{9.0} < M_\star < 10^{10.0} M_\odot$ , consistently with the analysis of the color of the ICL.

#### 4.8.3 The differential evolution of high and low-mass galaxies

I studied the mass-size relation of passive ETGs, separating the sample in low ( $M_\star \leq 10^{10} M_\odot$ ) and high-mass galaxies ( $M_\star \geq 10^{10} M_\odot$ ). Fig. 4.19 showed that low-mass galaxies follow a flatter relation with respect to the one of high-mass galaxies. The relation of low-mass early-type passive galaxies is in agreement, within  $1\sigma$ , with the relation presented for star-forming galaxies at similar redshift in van der Wel et al. (2014b). Moreover, van der Wel et al. (2014a) showed that at low redshifts emission-line galaxies are predominantly oblate and flat, that is, they are disks. This suggest that the mechanism responsible for the quenching

of star-forming galaxies should also affect the galaxy morphology changing late types into early ones. Furthermore, since I found that the slope of the passive SMF becomes steeper in low-density regions, i.e. the number of low-mass passive galaxies increases in the external regions of the cluster, the quenching mechanism has to be effective also at large radii. This, together with the possible change of the galaxy morphology, could favor mechanisms such as the harassment, (e.g. [Treu et al. 2003](#)). However, I can not exclude that starvation of the gas reservoir could lead to a changing appearance of the galaxy, by reducing the prominence of the disk relative to the bulge. Other quenching mechanisms, which act mainly on the truncation of star-formation, without affecting morphologies, could be effective also at small radii. In fact, I find a small number of galaxies in the spectroscopic sample which are passive according to the spectral classification but have a late-type morphology ( $n < 2.5$ ). The fraction of this type of galaxies is around 10% in the cluster center, then decreases at larger radii.

The evolution of galaxies in different cluster regions proposed so far is also supported by the analysis of the orbits, according to which, low-mass galaxies ( $M_{\star} \leq 10^{10} M_{\odot}$ ) in the center of the cluster have tangential orbits, meaning that they avoid small pericenters around the BCG. This could be explained by assuming that low-mass galaxies with radial orbits that go too close to the BCG are destroyed by tidal interactions. This is consistent with the analysis of the SMF and of the ICL discussed above. I also find that low-mass galaxies within  $\sim r_{-2}$  (0.65 Mpc) have smaller sizes per given mass than low-mass galaxies outside  $r_{-2}$  (Fig. 4.20). One can suppose that low-mass galaxies in the center are influenced by tidal interactions that reduce their sizes.

#### 4.8.4 Evidence of dynamical friction in stellar mass density profile

The environmental dependence of the stellar mass function is consistent with the relation between the number density, the stellar mass density and the total mass density profiles. I find that the ratio between the stellar mass density and the number density profiles is peaked towards the cluster center (fig. 20). This means that in the center of the cluster the mean mass is higher than in outer regions, a mass segregation effect. This effect is probably the combination of lack of low-mass galaxies and an excess of high-mass galaxies at small radii. The analysis of the ratio between the stellar mass density and the total mass density profiles suggests that dynamical friction has been effective in the cluster center, moving the most massive galaxies to the cluster center. Dynamical friction could also help lowering the galaxy velocities, thereby favoring the occurrence of mergers.





## Conclusions

---

The main focus of this Thesis was to analyze how cluster specific processes affect the evolution of cluster galaxies. This study was carried out by analyzing the properties of galaxies in two massive clusters: one at lower redshift, Abell 209 at  $\bar{z} = 0.21$ , and the other at higher redshift, MACS12066-0847 at  $\bar{z} = 0.44$ . For both clusters a large number of spectroscopic members (984 for A209 and 462 for M1206) was identified, reaching  $\sim 1/2$  of the total sample for Abell 209 and  $\sim 1/3$  of the total for M1206. From the simultaneous analysis of different galaxy properties one can understand the relative importance of different environmental processes in each cluster.

### MACS1206-0847

In the higher redshift cluster M1206, the whole distribution of galaxy stellar masses is clearly bimodal, with the total stellar mass function expressed in terms of a double Schechter function. The two components can be identified with the SMFs of Passive and SF galaxies respectively. The passive population is found to dominate the SF one for values of stellar mass greater than  $10^{10.1} M_{\odot}$  (see Sect. 3.3, Fig. 3.7). This value corresponds to the point at which the SMFs of passive and SF galaxies intersect each other and the total SMF deviates from a single Schechter. Below this value the population of SF galaxies is predominant. The value at which the SMFs of passive and SF galaxies cross depends on the environment, according to the model of Peng et al. (2010b), with higher values obtained in higher density regions. In agreement with this theoretical prediction, the crossing mass found in M1206 is  $\log M_{\star}/M_{\odot} \approx 10.5$  when considering only the region inside  $r_{200}$ , and  $\log M_{\star}/M_{\odot} \approx 9.5$

when considering only the region outside  $r_{200}$ . To analyze the effects of the environment on the SMF, I considered separately the SMF of passive and SF galaxies. This analysis has shown that the shape of the SMF of SF galaxies does not depend on the environment in all the cluster regions examined. This is consistent with predictions from the model of Peng et al. (2010b), and with other observations of the SMF of field galaxies (e.g. Ilbert et al., 2010; Huang et al., 2013).

The analysis of the SMF of passive galaxies, instead, shows a more complex scenario. I found that there is a significant change in the shape of the SMF of passive cluster galaxies only in the densest cluster region (corresponding to  $R \leq 0.25 r_{200} \sim 0.5 \text{ Mpc}$ ) (see Sect. 3.3, Fig. 3.9, bottom left panel). In this region, the SMF of passive galaxies is characterized by a different slope at the low mass end, smaller in absolute value. From Fig. 3.9, one can see that the SMF of passive galaxies in the densest cluster region intersects the SMFs in the outer regions at  $M_*/M_\odot \geq 10^{10.5}$ . By using this value to discriminate between giant ( $M_*/M_\odot \geq 10^{10.5}$ ) and subgiant ( $10^{9.5} \leq M_*/M_\odot < 10^{10.5}$ ) galaxies, the change of the SMF slope can also be seen in the radial trend in the giant/subgiant number ratio (GSNR see Fig. 3.11).

A possible interpretation of this radial trend is the following: in the outskirts of the cluster quenching mechanisms will transform the SF galaxies into passive ones. Since SF galaxies are less massive than passive ones, when they are quenched they populate the subgiant branch. However, very near the cluster center some process is capable of destroying subgiant galaxies, thus increasing the GSNR. This process could be tidal mass stripping by the cluster gravitational potential. At very small radii, tidal mass stripping become so effective that the low-mass galaxies are either totally destroyed or mass-stripped below the completeness limit of a given survey ( $10^{9.5} M_\odot$  in this case). The mass lost by galaxies in the subgiant range could create or at least partly contribute to the diffuse intra-cluster light (ICL) surrounding the cluster center. Support to this scenario comes from the comparison of the mass that is missing from galaxies in the subgiant range in the innermost cluster region (in comparison to the outer regions) and the mass of the ICL. The two mass values are:  $\Delta M_{sub} = 5.8_{-2.9}^{+3.3} \times 10^{11} M_\odot$  and  $M_{ICL} = 9.9 \pm 3.8 \times 10^{11} M_\odot$  (Presotto et al., 2014). Given the agreement between these two masses, one could suggest that the main progenitors of the ICL are passive galaxies with masses below  $10^{11} M_\odot$ .

The radial trend of the GSNR, as well as the environmental dependence of the SMF of passive galaxies, are also reflected in the decreasing stellar mass-to-number density profile ratio (see Sect. 3.4 Fig. 3.14). The mass segregation that is evident from the first two panels of Fig. 3.14 could originate from the lack of low mass galaxies in the cluster center or from an abundance of more massive galaxies in the same region due to dynamical friction. However, in this second case one would expect the total mass density profile to be less concentrated than the stellar mass density profile, as the diffuse dark matter component should gain energy at the expense of the subhalos (e.g. Del Popolo, 2012), and this is not seen (see the third

panel in Fig. 3.14). This is an indication that in this cluster the dynamical friction is not effective, as confirmed also from the fact the  $M^*$  of the SMFs of passive galaxies is similar in different cluster regions.

## Abell 209

Since this cluster is at lower redshift, it has been possible to analyze more galaxy properties than in M1206.

Also in this case the environmental dependence of the SMF has been investigated by examining passive and star-forming galaxies separately. As for M1206, no dependence on the environment was found for the SMF of SF galaxies. On the other hand, the SMF of passive galaxies was found to have a similar trend with local density as in M1206, with a smaller slope in the densest region, as shown in Fig. 4.11. This indicates also in this cluster a lack of low-mass galaxies in the densest cluster region, which could be the consequence of tidal stripping/destruction. As for M1206, this process could be at the origin of the ICL, as suggested from the comparison between the missing mass from subgiant galaxies and the ICL mass ( $\Delta M_{sub} = 1.4^{+0.5}_{-0.7} \times 10^{11} M_{\odot}$  and  $M_{ICL} = (2.9 \pm 0.7) \times 10^{11} M_{\odot}$ ). The higher contribution to the missing mass from subgiant galaxies seems to be due to galaxies in the mass range  $10^{9.0} < M_{\star} < 10^{10.0} M_{\odot}$ . Consistently, the  $B - R_C$  color of the ICL is in the same range of that of passive cluster members, supporting the idea that the ICL originate from these galaxies.

Additional support for the scenario of tidal destruction of low-mass galaxies comes from the analysis of their orbits in the cluster. The analysis of the velocity anisotropy profile (see Fig. 4.17) shows that low-mass passive galaxies are in fact characterized by tangential orbits that avoid small pericenters, whereas more massive galaxies ( $M_{\star} > 10^{10} M_{\odot}$ ) show radial orbits. This could probably be a selection effect, in the sense that low-mass galaxies with radial orbits that cross the cluster center are tidally destroyed and are therefore lacking from our sample.

The low-mass galaxies with tangential orbits that are able to survive in the cluster center thanks to their mostly tangential orbits, still suffer from the cluster tidal process, but in a lesser way. In fact, from the analysis of galaxy structural parameters it appears that low-mass galaxies within  $r \leq 0.65 Mpc$  have smaller sizes per given mass with respect to low-mass galaxies in more external regions (see Fig. 4.20). This could be an effect of tidal truncation by the cluster gravitational field.

At variance with the higher redshift sample, another effect of the environment on the SMFs of passive galaxies was found in terms of an increasing  $M^*$  with increasing local number density. This indicates an excess of massive galaxies towards the cluster center, which may originate from dynamical friction. This interpretation is further supported by the compara-

tive analysis of the cluster stellar and total mass density profiles shown in the third panel of Fig. 4.21. The fact that we do not observe dynamical friction in the  $z=0.44$  cluster while we do observe it in the  $z=0.21$  cluster suggests a lower limit of  $\sim 2$  Gyr for dynamical friction to operate (the cosmic time difference between the two redshifts). However, we cannot define a timescale for dynamical friction based only on two clusters, since the cosmic assembly history of the two can be very different, and play an important role in establishing mass segregation among galaxies.

The SMF of passive galaxies in A209 shows a low-mass component, that causes an upturn starting from  $10^{10} M_{\odot}$  (see Fig. 4.14), that is evident also in low density regions of the cluster. This component could originate from the environmental quenching of SF galaxies. This quenching becomes more effective at lower masses with increasing cosmic time, as suggested by the difference between the SMFs of passive galaxies in A209 and in M1206 (see Figs. 4.6 and 3.7). The presence of the low-mass component in the SMF of passive galaxies even in regions characterized by low number density suggests that the process responsible for the quenching of SF galaxies has to be effective also at large radii. In order to discriminate between different quenching mechanisms, I analyzed the mass-size relation of early type passive galaxies in two mass ranges using as threshold value  $10^{10} M_{\odot}$ . The relation obtained for the two samples is shown in Fig. 4.19. Low mass passive ETGs follow a mass-size relation which is flatter with respect to the one of high-mass galaxies but in agreement within  $1\sigma$  with the relation obtained for star-forming galaxies at similar redshift (van der Wel et al., 2014b). This suggests a scenario in which SF galaxies are accreted from the field, then quenched and morphologically transformed in passive early type systems also at large distances from the cluster center. These evidences seem to favor harassment (perhaps together with starvation) as the main quenching mechanism.

## Future perspectives

From the analyses carried out in this Thesis, it is clear that finding a consistent scenario for cluster assembly is complex, owing to the interplay of a number of different physical processes effective in clusters. In order to have a more comprehensive view of galaxy evolution, one should combine the information obtained from the stellar mass function together with the analysis of the ICL, while it is also important to add information derived from the analysis of galaxy kinematics and structural properties. The analyses presented in this Thesis will be carried out also for the other CLASH-VLT clusters for which we have the same kind of datasets, in order to increase the relevance of these results by increasing the statistics. It will be possible to test the scenarios proposed in this Thesis by considering clusters at different epochs (intermediate between the two considered so far) and in different dynamical states.

So far, little use has been done of the spectroscopic characteristics of cluster galaxies. Detailed information on the relative strengths of different absorption and emission lines will be used to provide approximate estimates of the ages of stellar populations (this will be possible in particular using a stacked spectra analysis). Characterizing the different cluster galaxy populations by their mean stellar ages will add a fundamental ingredient for our understanding of galaxy evolution and transformation.

It will be important also to compare the results obtained for these two clusters with predictions from semi-analytical models. In particular, it will be useful to test how different models (e.g. [Hirschmann et al., 2015](#); [Henriques et al., 2015](#); [De Lucia and Blaizot, 2007](#)) reproduce the SMFs of different galaxy types. In fact, the comparisons carried out so far either have been focused on field galaxies (e.g. [Fontanot et al., 2009](#)), or on the mass distribution of the total population without distinguishing among different galaxy types (e.g. [Vulcani et al., 2014](#)). Another important aspect will be to test the evolutionary scenario of cluster galaxies presented in this Thesis using semi-analytical models, in particular regarding the tidal destruction of low mass galaxies and the ICL formation. Knowledge of galaxy progenitors, available for semi-analytical models, is crucial to interpret the observational results obtained concerning the redshift evolution of cluster galaxies. Finally, since semi-analytical models provide information on the time at which each galaxy enters in the cluster, it will be also possible to test how different scenarios of galaxy evolution depend on the cluster accretion history.



# Bibliography

---

- G. O. Abell. The Distribution of Rich Clusters of Galaxies. *ApJS*, 3:211, May 1958. doi: 10.1086/190036.
- S. Andreon. Observational evidence that massive cluster galaxies were forming stars at  $z \sim 2.5$  and did not grow in mass at later times. *A&A*, 554:A79, June 2013. doi: 10.1051/0004-6361/201321071.
- M. Annunziatella, A. Mercurio, M. Brescia, S. Cavaoti, and G. Longo. Inside Catalogs: A Comparison of Source Extraction Software. *PASP*, 125:68–82, January 2013. doi: 10.1086/669333.
- M. Annunziatella, A. Biviano, A. Mercurio, M. Nonino, P. Rosati, I. Balestra, V. Presotto, M. Girardi, R. Gobat, C. Grillo, D. Kelson, E. Medezinski, M. Postman, M. Scodeggio, M. Brescia, R. Demarco, A. Fritz, A. Koekemoer, D. Lemze, M. Lombardi, B. Sartoris, K. Umetsu, E. Vanzella, L. Bradley, D. Coe, M. Donahue, L. Infante, U. Kuchner, C. Maier, E. Reg  s, M. Verdugo, and B. Ziegler. CLASH-VLT: The stellar mass function and stellar mass density profile of the  $z = 0.44$  cluster of galaxies MACS J1206.2-0847. *A&A*, 571:A80, November 2014. doi: 10.1051/0004-6361/201424102.
- M. Annunziatella, A. Mercurio, A. Biviano, M. Girardi, M. Nonino, I. Balestra, P. Rosati, G. Bartosch Caminha, M. Brescia, R. Gobat, C. Grillo, M. Lombardi, B. Sartoris, G. De Lucia, R. Demarco, B. Frye, A. Fritz, J. Moustakas, M. Scodeggio, U. Kuchner, C. Maier, and B. Ziegler. CLASH-VLT: Environment-driven evolution of galaxies in the  $z=0.209$  cluster Abell 209. *ArXiv e-prints*, October 2015.
- M. Arnaboldi, K. C. Freeman, R. H. Mendez, M. Capaccioli, R. Ciardullo, H. Ford, O. Gerhard, X. Hui, G. H. Jacoby, R. P. Kudritzki, and P. J. Quinn. The Kinematics of the Planetary Nebulae in the Outer Regions of NGC 4406. *ApJ*, 472:145, November 1996. doi: 10.1086/178050.

- H. Baba, N. Yasuda, S.-I. Ichikawa, M. Yagi, N. Iwamoto, T. Takata, T. Horaguchi, M. Taga, M. Watanabe, S.-I. Okumura, T. Ozawa, N. Yamamoto, and M. Hamabe. Development of public science archive system of Subaru Telescope. *Report of the National Astronomical Observatory of Japan*, 6:23–36, September 2002a.
- H. Baba, N. Yasuda, S.-I. Ichikawa, M. Yagi, N. Iwamoto, T. Takata, T. Horaguchi, M. Taga, M. Watanabe, T. Ozawa, and M. Hamabe. Development of the Subaru-Mitaka-Okayama-Kiso Archive System. In D. A. Bohlender, D. Durand, and T. H. Handley, editors, *Astronomical Data Analysis Software and Systems XI*, volume 281 of *Astronomical Society of the Pacific Conference Series*, page 298, 2002b.
- N. A. Bahcall and A. Kulier. Tracing mass and light in the Universe: where is the dark matter? *MNRAS*, February 2014. doi: 10.1093/mnras/stu107.
- I. K. Baldry, M. L. Balogh, R. Bower, K. Glazebrook, and R. C. Nichol. Color bimodality: Implications for galaxy evolution. In R. E. Allen, D. V. Nanopoulos, and C. N. Pope, editors, *The New Cosmology: Conference on Strings and Cosmology*, volume 743 of *American Institute of Physics Conference Series*, pages 106–119, December 2004. doi: 10.1063/1.1848322.
- I. K. Baldry, K. Glazebrook, and S. P. Driver. On the galaxy stellar mass function, the mass-metallicity relation and the implied baryonic mass function. *MNRAS*, 388:945–959, August 2008. doi: 10.1111/j.1365-2966.2008.13348.x.
- I. K. Baldry, S. P. Driver, J. Loveday, E. N. Taylor, L. S. Kelvin, J. Liske, P. Norberg, A. S. G. Robotham, S. Brough, A. M. Hopkins, S. P. Bamford, J. A. Peacock, J. Bland-Hawthorn, C. J. Conselice, S. M. Croom, D. H. Jones, H. R. Parkinson, C. C. Popescu, M. Prescott, R. G. Sharp, and R. J. Tuffs. Galaxy And Mass Assembly (GAMA): the galaxy stellar mass function at  $z < 0.06$ . *MNRAS*, 421:621–634, March 2012. doi: 10.1111/j.1365-2966.2012.20340.x.
- M. L. Balogh, J. F. Navarro, and S. L. Morris. The Origin of Star Formation Gradients in Rich Galaxy Clusters. *ApJ*, 540:113–121, September 2000. doi: 10.1086/309323.
- M. L. Balogh, F. R. Pearce, R. G. Bower, and S. T. Kay. Revisiting the cosmic cooling crisis. *MNRAS*, 326:1228–1234, October 2001. doi: 10.1111/j.1365-8711.2001.04667.x.
- M. Barden, B. Häußler, C. Y. Peng, D. H. McIntosh, and Y. Guo. GALAPAGOS: from pixels to parameters. *MNRAS*, 422:449–468, May 2012. doi: 10.1111/j.1365-2966.2012.20619.x.
- W. A. Barkhouse, H. K. C. Yee, and O. López-Cruz. The Galaxy Population of Low-redshift Abell Clusters. *ApJ*, 703:2024–2032, October 2009. doi: 10.1088/0004-637X/703/2/2024.



- M. Bartelmann. Arcs from a universal dark-matter halo profile. *A&A*, 313:697–702, September 1996.
- K. Bekki, W. J. Couch, and Y. Shioya. Passive Spiral Formation from Halo Gas Starvation: Gradual Transformation into S0s. *ApJ*, 577:651–657, October 2002. doi: 10.1086/342221.
- E. Bertin. Automated Morphometry with SExtractor and PSFEx. In I. N. Evans, A. Accomazzi, D. J. Mink, and A. H. Rots, editors, *Astronomical Data Analysis Software and Systems XX*, volume 442 of *Astronomical Society of the Pacific Conference Series*, page 435, July 2011a.
- E. Bertin. Automated Morphometry with SExtractor and PSFEx. In I. N. Evans, A. Accomazzi, D. J. Mink, and A. H. Rots, editors, *Astronomical Data Analysis Software and Systems XX*, volume 442 of *Astronomical Society of the Pacific Conference Series*, page 435, July 2011b.
- E. Bertin and S. Arnouts. SExtractor: Software for source extraction. *A&AS*, 117:393–404, June 1996a. doi: 10.1051/aas:1996164.
- E. Bertin and S. Arnouts. SExtractor: Software for source extraction. *A&AS*, 117:393–404, June 1996b. doi: 10.1051/aas:1996164.
- D. Bialas, T. Lisker, C. Olczak, R. Spurzem, and R. Kotulla. On the occurrence of galaxy harassment. *A&A*, 576:A103, April 2015. doi: 10.1051/0004-6361/201425235.
- R. Bielby, P. Hudelot, H. J. McCracken, O. Ilbert, E. Daddi, O. Le Fèvre, V. Gonzalez-Perez, J.-P. Kneib, C. Marmo, Y. Mellier, M. Salvato, D. B. Sanders, and C. J. Willott. The WIRCam Deep Survey. I. Counts, colours, and mass-functions derived from near-infrared imaging in the CFHTLS deep fields. *A&A*, 545:A23, September 2012. doi: 10.1051/0004-6361/201118547.
- B. Binggeli and H. Jerjen. Is the shape of the luminosity profile of dwarf elliptical galaxies an useful distance indicator? *A&A*, 333:17–26, May 1998.
- B. Binggeli, A. Sandage, and M. Tarenghi. Studies of the Virgo Cluster. I - Photometry of 109 galaxies near the cluster center to serve as standards. *AJ*, 89:64–82, January 1984. doi: 10.1086/113484.
- J. Binney and G. A. Mamon. M/l and velocity anisotropy from observations of spherical galaxies, or must m87 have a massive black hole? *MNRAS*, 200:361–375, July 1982.
- J. Binney and S. Tremaine. *Galactic dynamics*. Princeton, NJ, Princeton University Press, 1987, 747 p., 1987.

- J. Binney and S. Tremaine. *Galactic Dynamics*. Princeton University Press, 1987.
- A. Biviano. Galaxy systems in the optical and infrared. *ArXiv e-prints*, November 2008.
- A. Biviano and M. Girardi. The Mass Profile of Galaxy Clusters out to  $\sim 2r_{200}$ . *ApJ*, 585: 205–214, March 2003. doi: 10.1086/345893.
- A. Biviano and B. M. Poggianti. The orbital velocity anisotropy of cluster galaxies: evolution. *A&A*, 501:419–427, July 2009. doi: 10.1051/0004-6361/200911757.
- A. Biviano and P. Salucci. The radial profiles of the different mass components in galaxy clusters. *A&A*, 452:75–81, June 2006.
- A. Biviano, P. Katgert, T. Thomas, and C. Adami. The eso nearby abell cluster survey. xi. segregation of cluster galaxies and subclustering. *A&A*, 387:8–25, May 2002.
- A. Biviano, P. Rosati, I. Balestra, A. Mercurio, M. Girardi, M. Nonino, C. Grillo, M. Scodeggio, D. Lemze, D. Kelson, K. Umetsu, M. Postman, A. Zitrin, O. Czoske, S. Ettori, A. Fritz, M. Lombardi, C. Maier, E. Medezinski, S. Mei, V. Presotto, V. Strazzullo, P. Tozzi, B. Ziegler, M. Annunziatella, M. Bartelmann, N. Benitez, L. Bradley, M. Brescia, T. Broadhurst, D. Coe, R. Demarco, M. Donahue, H. Ford, R. Gobat, G. Graves, A. Koekemoer, U. Kuchner, P. Melchior, M. Meneghetti, J. Merten, L. Moustakas, E. Munari, E. Regős, B. Sartoris, S. Seitz, and W. Zheng. CLASH-VLT: The mass, velocity-anisotropy, and pseudo-phase-space density profiles of the  $z = 0.44$  galaxy cluster MACS J1206.2-0847. *A&A*, 558:A1, October 2013. doi: 10.1051/0004-6361/201321955.
- M. Bolzonella, K. Kovač, L. Pozzetti, E. Zucca, O. Cucciati, S. J. Lilly, Y. Peng, A. Iovino, G. Zamorani, D. Vergani, L. A. M. Tasca, F. Lamareille, P. Oesch, K. Caputi, P. Kampczyk, S. Bardelli, C. Maier, U. Abbas, C. Knobel, M. Scodeggio, C. M. Carollo, T. Contini, J.-P. Kneib, O. Le Fèvre, V. Mainieri, A. Renzini, A. Bongiorno, G. Coppia, S. de la Torre, L. de Ravel, P. Franzetti, B. Garilli, J.-F. Le Borgne, V. Le Brun, M. Mignoli, R. Pelló, E. Perez-Montero, E. Ricciardelli, J. D. Silverman, M. Tanaka, L. Tresse, D. Bottini, A. Cappi, P. Casata, A. Cimatti, L. Guzzo, A. M. Koekemoer, A. Leauthaud, D. Maccagni, C. Marinoni, H. J. McCracken, P. Memeo, B. Meneux, C. Porciani, R. Scaramella, H. Aussel, P. Capak, C. Halliday, O. Ilbert, J. Kartaltepe, M. Salvato, D. Sanders, C. Scarlata, N. Scoville, Y. Taniguchi, and D. Thompson. Tracking the impact of environment on the galaxy stellar mass function up to  $z \sim 1$  in the 10 k zCOSMOS sample. *A&A*, 524:A76, December 2010. doi: 10.1051/0004-6361/200912801.
- A. Boselli, S. Boissier, L. Cortese, A. Gil de Paz, M. Seibert, B. F. Madore, V. Buat, and D. C. Martin. The Fate of Spiral Galaxies in Clusters: The Star Formation History of the Anemic Virgo Cluster Galaxy NGC 4569. *ApJ*, 651:811–821, November 2006. doi: 10.1086/507766.

- H. Bouy, E. Bertin, E. Moraux, J.-C. Cuillandre, J. Bouvier, D. Barrado, E. Solano, and A. Bayo. Dynamical analysis of nearby clusters. Automated astrometry from the ground: precision proper motions over a wide field. *A&A*, 554:A101, June 2013. doi: 10.1051/0004-6361/201220748.
- M. Boylan-Kolchin, C.-P. Ma, and E. Quataert. Dynamical friction and galaxy merging time-scales. *MNRAS*, 383:93–101, January 2008. doi: 10.1111/j.1365-2966.2007.12530.x.
- G. B. Brammer, P. G. van Dokkum, and P. Coppi. EAZY: A Fast, Public Photometric Redshift Code. *ApJ*, 686:1503–1513, October 2008. doi: 10.1086/591786.
- M. Brescia, S. Cavuoti, R. D’Abrusco, G. Longo, and A. Mercurio. Photometric Redshifts for Quasars in Multi-band Surveys. *ApJ*, 772:140, August 2013. doi: 10.1088/0004-637X/772/2/140.
- G. Bruzual and S. Charlot. Stellar population synthesis at the resolution of 2003. *MNRAS*, 344:1000–1028, October 2003. doi: 10.1046/j.1365-8711.2003.06897.x.
- K. Bundy, R. S. Ellis, and C. J. Conselice. The Mass Assembly Histories of Galaxies of Various Morphologies in the GOODS Fields. *ApJ*, 625:621–632, June 2005. doi: 10.1086/429549.
- H. Butcher and A. Oemler, Jr. The evolution of galaxies in clusters. I - ISIT photometry of C1 0024+1654 and 3C 295. *ApJ*, 219:18–30, January 1978. doi: 10.1086/155751.
- G. Byrd and M. Valtonen. Tidal generation of active spirals and S0 galaxies by rich clusters. *ApJ*, 350:89–94, February 1990. doi: 10.1086/168362.
- J. A. R. Caldwell, D. H. McIntosh, H.-W. Rix, M. Barden, S. V. W. Beckwith, E. F. Bell, A. Borch, C. Heymans, B. Häußler, K. Jahnke, S. Jogee, K. Meisenheimer, C. Y. Peng, S. F. Sánchez, R. S. Somerville, L. Wisotzki, and C. Wolf. GEMS Survey Data and Catalog. *ApJS*, 174:136–144, January 2008. doi: 10.1086/521080.
- R. Calvi, B. M. Poggianti, B. Vulcani, and G. Fasano. The impact of global environment on galaxy mass functions at low redshift. *MNRAS*, 432:3141–3152, July 2013. doi: 10.1093/mnras/stt667.
- D. Capozzi, C. A. Collins, J. P. Stott, and M. Hilton. The evolution of  $K^*$  and the halo occupation distribution since  $z = 1.5$ : observations versus simulations. *MNRAS*, 419:2821–2835, February 2012. doi: 10.1111/j.1365-2966.2011.19895.x.

- M. Cappellari and E. Emsellem. Parametric Recovery of Line-of-Sight Velocity Distributions from Absorption-Line Spectra of Galaxies via Penalized Likelihood. *PASP*, 116:138–147, February 2004. doi: 10.1086/381875.
- M. Cappellari, N. Scott, K. Alatalo, L. Blitz, M. Bois, F. Bournaud, M. Bureau, A. F. Crocker, R. L. Davies, T. A. Davis, P. T. de Zeeuw, P.-A. Duc, E. Emsellem, S. Khochfar, D. Krajnović, H. Kuntschner, R. M. McDermid, R. Morganti, T. Naab, T. Oosterloo, M. Sarzi, P. Serra, A.-M. Weijmans, and L. M. Young. The ATLAS<sup>3D</sup> project - XV. Benchmark for early-type galaxies scaling relations from 260 dynamical models: mass-to-light ratio, dark matter, Fundamental Plane and Mass Plane. *MNRAS*, 432:1709–1741, July 2013. doi: 10.1093/mnras/stt562.
- R. G. Carlberg. Understanding the Universe. (Book Reviews: Principles of Physical Cosmology.). *Science*, 261:1758, September 1993. doi: 10.1126/science.261.5129.1758.
- R. G. Carlberg, H. K. C. Yee, E. Ellingson, S. L. Morris, R. Abraham, P. Gravel, C. J. Pritchet, T. Smecker-Hane, F. D. A. Hartwick, J. E. Hesser, J. B. Hutchings, and J. B. Oke. The Average Mass Profile of Galaxy Clusters. *ApJ*, 485:L13–L16, August 1997. doi: 10.1086/310801.
- S. Cavuoti, M. Brescia, G. Longo, and A. Mercurio. Photometric redshifts with the quasi Newton algorithm (MLPQNA) Results in the PHAT1 contest. *A&A*, 546:A13, October 2012. doi: 10.1051/0004-6361/201219755.
- G. Chabrier. Galactic Stellar and Substellar Initial Mass Function. *PASP*, 115:763–795, July 2003. doi: 10.1086/376392.
- S. Chandrasekhar. Dynamical Friction. I. General Considerations: the Coefficient of Dynamical Friction. *ApJ*, 97:255, March 1943. doi: 10.1086/144517.
- S. Charlot and S. M. Fall. A Simple Model for the Absorption of Starlight by Dust in Galaxies. *ApJ*, 539:718–731, August 2000. doi: 10.1086/309250.
- C. Conroy, R. H. Wechsler, and A. V. Kravtsov. The Hierarchical Build-Up of Massive Galaxies and the Intracluster Light since  $z = 1$ . *ApJ*, 668:826–838, October 2007. doi: 10.1086/521425.
- C. J. Conselice. The Formation of Low-Mass Cluster Galaxies and the Universal Initial Galaxy Mass Function. *ApJ*, 573:L5–L8, July 2002. doi: 10.1086/341878.

- E. Contini, G. De Lucia, Á. Villalobos, and S. Borgani. On the formation and physical properties of the intracluster light in hierarchical galaxy formation models. *MNRAS*, 437:3787–3802, February 2014a. doi: 10.1093/mnras/stt2174.
- E. Contini, G. De Lucia, Á. Villalobos, and S. Borgani. On the formation and physical properties of the intracluster light in hierarchical galaxy formation models. *MNRAS*, 437:3787–3802, February 2014b. doi: 10.1093/mnras/stt2174.
- M. C. Cooper, R. L. Griffith, J. A. Newman, A. L. Coil, M. Davis, A. A. Dutton, S. M. Faber, P. Guhathakurta, D. C. Koo, J. M. Lotz, B. J. Weiner, C. N. A. Willmer, and R. Yan. The DEEP3 Galaxy Redshift Survey: the impact of environment on the size evolution of massive early-type galaxies at intermediate redshift. *MNRAS*, 419:3018–3027, February 2012. doi: 10.1111/j.1365-2966.2011.19938.x.
- L. Cortese, D. Marcillac, J. Richard, H. Bravo-Alfaro, J.-P. Kneib, G. Rieke, G. Covone, E. Egami, J. Rigby, O. Czoske, and J. Davies. The strong transformation of spiral galaxies infalling into massive clusters at  $z \sim 0.2$ . *MNRAS*, 376:157–172, March 2007. doi: 10.1111/j.1365-2966.2006.11369.x.
- L. L. Cowie and A. Songaila. Thermal evaporation of gas within galaxies by a hot intergalactic medium. *Nature*, 266:501–503, April 1977. doi: 10.1038/266501a0.
- W. Cui, G. Murante, P. Monaco, S. Borgani, G. L. Granato, M. Killedar, G. De Lucia, V. Prestotto, and K. Dolag. Characterizing diffused stellar light in simulated galaxy clusters. *MNRAS*, 437:816–830, January 2014. doi: 10.1093/mnras/stt1940.
- E. da Cunha, S. Charlot, and D. Elbaz. A simple model to interpret the ultraviolet, optical and infrared emission from galaxies. *MNRAS*, 388:1595–1617, August 2008. doi: 10.1111/j.1365-2966.2008.13535.x.
- I. Davidzon, M. Bolzonella, J. Coupon, O. Ilbert, S. Arnouts, S. de la Torre, A. Fritz, G. De Lucia, A. Iovino, B. R. Granett, G. Zamorani, L. Guzzo, U. Abbas, C. Adami, J. Bel, D. Bottini, E. Branchini, A. Cappi, O. Cucciati, P. Franzetti, M. Fumana, B. Garilli, J. Krywult, V. Le Brun, O. Le Fèvre, D. Maccagni, K. Małek, F. Marulli, H. J. McCracken, L. Paioro, J. A. Peacock, M. Polletta, A. Pollo, H. Schlagenhauser, M. Scodeggio, L. A. M. Tasca, R. Tojeiro, D. Vergani, A. Zanicelli, A. Burden, C. Di Porto, A. Marchetti, C. Marinoni, Y. Mellier, L. Moscardini, T. Moutard, R. C. Nichol, W. J. Percival, S. Phleps, and M. Wolk. The VIMOS Public Extragalactic Redshift Survey (VIPERS). A precise measurement of the galaxy stellar mass function and the abundance of massive galaxies at redshifts  $0.5 < z < 1.3$ . *A&A*, 558:A23, October 2013. doi: 10.1051/0004-6361/201321511.

- G. De Lucia and J. Blaizot. The hierarchical formation of the brightest cluster galaxies. *MNRAS*, 375:2–14, February 2007. doi: 10.1111/j.1365-2966.2006.11287.x.
- R. De Propris and D. Christlein. A composite K-band luminosity function for cluster galaxies. *Astronomische Nachrichten*, 330:943, December 2009. doi: 10.1002/asna.200911268.
- R. De Propris, S. A. Stanford, P. R. Eisenhardt, B. P. Holden, and P. Rosati. The Rest-Frame K-Band Luminosity Function of Galaxies in Clusters to  $z = 1.3$ . *AJ*, 133:2209–2215, May 2007. doi: 10.1086/513516.
- G. de Vaucouleurs. Classification and Morphology of External Galaxies. *Handbuch der Physik*, 53:275, 1959.
- A. Del Popolo. On the density-profile slope of clusters of galaxies. *MNRAS*, 424:38–51, July 2012. doi: 10.1111/j.1365-2966.2012.21141.x.
- T. DeMaio, A. H. Gonzalez, A. Zabludoff, D. Zaritsky, and M. Bradač. On the origin of the intracluster light in massive galaxy clusters. *MNRAS*, 448:1162–1177, April 2015. doi: 10.1093/mnras/stv033.
- S. R. Dicker, P. M. Korngut, B. S. Mason, P. A. R. Ade, J. Aguirre, T. J. Ames, D. J. Benford, T. C. Chen, J. A. Chervenak, W. D. Cotton, M. J. Devlin, E. Figueroa-Feliciano, K. D. Irwin, S. Maher, M. Mello, S. H. Moseley, D. J. Tally, C. Tucker, and S. D. White. MUSTANG: 90 GHz science with the Green Bank Telescope. In *Society of Photo-Optical Instrumentation Engineers (SPIE) Conference Series*, volume 7020 of *Society of Photo-Optical Instrumentation Engineers (SPIE) Conference Series*, page 5, August 2008. doi: 10.1117/12.788361.
- S. Djorgovski and M. Davis. Fundamental properties of elliptical galaxies. *ApJ*, 313:59–68, February 1987. doi: 10.1086/164948.
- A. Dressler. Galaxy morphology in rich clusters - Implications for the formation and evolution of galaxies. *ApJ*, 236:351–365, March 1980. doi: 10.1086/157753.
- A. Dressler, A. Oemler, Jr., B. M. Poggianti, I. Smail, S. Trager, S. A. Shectman, W. J. Couch, and R. S. Ellis. Studying the Star Formation Histories of Galaxies in Clusters from Composite Spectra. *ApJ*, 617:867–878, December 2004. doi: 10.1086/424890.
- N. Drory and M. Alvarez. The Contribution of Star Formation and Merging to Stellar Mass Buildup in Galaxies. *ApJ*, 680:41–53, June 2008. doi: 10.1086/588006.

- N. Drory, K. Bundy, A. Leauthaud, N. Scoville, P. Capak, O. Ilbert, J. S. Kartaltepe, J. P. Kneib, H. J. McCracken, M. Salvato, D. B. Sanders, D. Thompson, and C. J. Willott. The Bimodal Galaxy Stellar Mass Function in the COSMOS Survey to  $z \sim 1$ : A Steep Faint End and a New Galaxy Dichotomy. *ApJ*, 707:1595–1609, December 2009. doi: 10.1088/0004-637X/707/2/1595.
- P. R. Durrell, R. Ciardullo, J. J. Feldmeier, G. H. Jacoby, and S. Sigurdsson. Intracuster Red Giant Stars in the Virgo Cluster. *ApJ*, 570:119–131, May 2002. doi: 10.1086/339735.
- H. Ebeling, A. C. Edge, and J. P. Henry. MACS: A Quest for the Most Massive Galaxy Clusters in the Universe. *ApJ*, 553:668–676, June 2001a. doi: 10.1086/320958.
- H. Ebeling, A. C. Edge, and J. P. Henry. MACS: A Quest for the Most Massive Galaxy Clusters in the Universe. *ApJ*, 553:668–676, June 2001b. doi: 10.1086/320958.
- H. Ebeling, C. J. Ma, J.-P. Kneib, E. Jullo, N. J. D. Courtney, E. Barrett, A. C. Edge, and J.-F. Le Borgne. A spectacular giant arc in the massive cluster lens macsj1206.2-0847. *MNRAS*, 395:1213–1224, May 2009a.
- H. Ebeling, C. J. Ma, J.-P. Kneib, E. Jullo, N. J. D. Courtney, E. Barrett, A. C. Edge, and J.-F. Le Borgne. A spectacular giant arc in the massive cluster lens MACSJ1206.2-0847. *MNRAS*, 395:1213–1224, May 2009b. doi: 10.1111/j.1365-2966.2009.14502.x.
- H. Ebeling, L. N. Stephenson, and A. C. Edge. Jellyfish: Evidence of Extreme Ram-pressure Stripping in Massive Galaxy Clusters. *ApJ*, 781:L40, February 2014. doi: 10.1088/2041-8205/781/2/L40.
- A. E. Evrard. Clues to galaxy activity from rich cluster simulations. *MNRAS*, 248:8P–10P, January 1991.
- S. M. Faber and R. E. Jackson. Velocity dispersions and mass-to-light ratios for elliptical galaxies. *ApJ*, 204:668–683, March 1976. doi: 10.1086/154215.
- D. Fadda, M. Girardi, G. Giuricin, F. Mardirossian, and M. Mezzetti. The Observational Distribution of Internal Velocity Dispersions in Nearby Galaxy Clusters. *ApJ*, 473:670, December 1996. doi: 10.1086/178180.
- J. J. Feldmeier, R. Ciardullo, G. H. Jacoby, and P. R. Durrell. Intracuster Planetary Nebulae in the Virgo Cluster. III. Luminosity of the Intracuster Light and Tests of the Spatial Distribution. *ApJ*, 615:196–208, November 2004. doi: 10.1086/424372.

- R. A. Fish. A Mass-Potential Relationship in Elliptical Galaxies and Some Inferences Concerning the Formation and Evolution of Galaxies. *ApJ*, 139:284, January 1964. doi: 10.1086/147753.
- A. Fontana, S. Salimbeni, A. Grazian, E. Giallongo, L. Pentericci, M. Nonino, F. Fontanot, N. Menci, P. Monaco, S. Cristiani, E. Vanzella, C. de Santis, and S. Gallozzi. The Galaxy mass function up to  $z=4$  in the GOODS-MUSIC sample: into the epoch of formation of massive galaxies. *A&A*, 459:745–757, December 2006. doi: 10.1051/0004-6361:20065475.
- F. Fontanot, G. De Lucia, P. Monaco, R. S. Somerville, and P. Santini. The many manifestations of downsizing: hierarchical galaxy formation models confront observations. *MNRAS*, 397:1776–1790, August 2009. doi: 10.1111/j.1365-2966.2009.15058.x.
- Y. Fujita. Quantitative Estimates of Environmental Effects on the Star Formation Rate of Disk Galaxies in Clusters of Galaxies. *ApJ*, 509:587–594, December 1998. doi: 10.1086/306518.
- Y. Fujita. Pre-Processing of Galaxies before Entering a Cluster. *PASJ*, 56:29–43, February 2004. doi: 10.1093/pasj/56.1.29.
- A. Gal-Yam, D. Maoz, P. Guhathakurta, and A. V. Filippenko. A Population of Intergalactic Supernovae in Galaxy Clusters. *AJ*, 125:1087–1094, March 2003. doi: 10.1086/346141.
- G. Garmire. Continuation of a Chandra Survey of a Uniformly Selected Sample of High-Redshift Galaxy Clusters. Chandra Proposal, September 2003.
- K. Gebhardt, C. Pryor, T. B. Williams, and J. E. Hesser. Fabry-Perot measurements of the dynamics of globular cluster cores: M15 (NGC 7078). *AJ*, 107:2067–2076, June 1994. doi: 10.1086/117017.
- E. Giallongo, N. Menci, A. Grazian, S. Gallozzi, M. Castellano, F. Fiore, A. Fontana, L. Pentericci, K. Boutsia, D. Paris, R. Speziali, and V. Testa. Diffuse Optical Intracuster Light as a Measure of Stellar Tidal Stripping: The Cluster CL0024+17 at  $z \sim 0.4$  Observed at the Large Binocular Telescope. *ApJ*, 781:24, January 2014. doi: 10.1088/0004-637X/781/1/24.
- S. Giodini, A. Finoguenov, D. Pierini, G. Zamorani, O. Ilbert, S. Lilly, Y. Peng, N. Scoville, and M. Tanaka. The galaxy stellar mass function of X-ray detected groups. Environmental dependence of galaxy evolution in the COSMOS survey. *A&A*, 538:A104, February 2012. doi: 10.1051/0004-6361/201117696.
- M. Girardi, A. Mercurio, I. Balestra, M. Nonino, A. Biviano, C. Grillo, P. Rosati, M. Annunziatella, R. Demarco, A. Fritz, R. Gobat, D. Lemze, V. Presotto, M. Scodeggio, P. Tozzi,



- G. Bartosch Caminha, M. Brescia, D. Coe, D. Kelson, A. Koekemoer, M. Lombardi, E. Medezinski, M. Postman, B. Sartoris, K. Umetsu, A. Zitrin, W. Boschin, O. Czoske, G. De Lucia, U. Kuchner, C. Maier, M. Meneghetti, P. Monaco, A. Monna, E. Munari, S. Seitz, M. Verdugo, and B. Ziegler. CLASH-VLT: Substructure in the galaxy cluster MACSJ1206.2-0847 from kinematics of galaxy populations. *A&A*, 579:A4, July 2015. doi: 10.1051/0004-6361/201425599.
- O. Y. Gnedin. Tidal Effects in Clusters of Galaxies. *ApJ*, 582:141–161, January 2003. doi: 10.1086/344636.
- S. Golwala, S. Ameglio, E. Pierpaoli, and J. Sayers. Sunyaev-Zeldovich Effect Studies of Galaxy Clusters with Bolocam (and Future Instrumentation). In D. C. Lis, J. E. Vaillancourt, P. F. Goldsmith, T. A. Bell, N. Z. Scoville, and J. Zmuidzinas, editors, *Submillimeter Astrophysics and Technology: a Symposium Honoring Thomas G. Phillips*, volume 417 of *Astronomical Society of the Pacific Conference Series*, page 311, December 2009.
- A. H. Gonzalez, A. I. Zabludoff, and D. Zaritsky. Intracluster Light in Nearby Galaxy Clusters: Relationship to the Halos of Brightest Cluster Galaxies. *ApJ*, 618:195–213, January 2005. doi: 10.1086/425896.
- A. H. Gonzalez, D. Zaritsky, and A. I. Zabludoff. A Census of Baryons in Galaxy Clusters and Groups. *ApJ*, 666:147–155, September 2007. doi: 10.1086/519729.
- A. H. Gonzalez, S. Sivanandam, A. I. Zabludoff, and D. Zaritsky. Galaxy Cluster Baryon Fractions Revisited. *ApJ*, 778:14, November 2013. doi: 10.1088/0004-637X/778/1/14.
- L. Guennou, C. Adami, C. Da Rocha, F. Durret, M. P. Ulmer, S. Allam, S. Basa, C. Benoist, A. Biviano, D. Clowe, R. Gavazzi, C. Halliday, O. Ilbert, D. Johnston, D. Just, R. Kron, J. M. Kubo, V. Le Brun, P. Marshall, A. Mazure, K. J. Murphy, D. N. E. Pereira, C. R. Rabaça, F. Rostagni, G. Rudnick, D. Russeil, T. Schrabback, E. Slezak, D. Tucker, and D. Zaritsky. Intracluster light in clusters of galaxies at redshifts  $0.4 < z < 0.8$ . *A&A*, 537:A64, January 2012. doi: 10.1051/0004-6361/201117482.
- J. E. Gunn and J. R. Gott, III. On the Infall of Matter Into Clusters of Galaxies and Some Effects on Their Evolution. *ApJ*, 176:1, August 1972. doi: 10.1086/151605.
- B. M. B. Henriques, S. D. M. White, P. A. Thomas, R. Angulo, Q. Guo, G. Lemson, V. Springel, and R. Overzier. Galaxy formation in the Planck cosmology - I. Matching the observed evolution of star formation rates, colours and stellar masses. *MNRAS*, 451:2663–2680, August 2015. doi: 10.1093/mnras/stv705.

- M. Hirschmann, G. De Lucia, and F. Fontanot. Galaxy assembly, stellar feedback and metal enrichment: the view from the GAEA model. *ArXiv e-prints*, December 2015.
- J.-S. Huang, S. M. Faber, C. N. A. Willmer, D. Rigopoulou, D. Koo, J. Newman, C. Shu, M. L. N. Ashby, P. Barmby, A. Coil, Z. Luo, G. Magdis, T. Wang, B. Weiner, S. P. Willner, X. Z. Zheng, and G. G. Fazio. Multi-Wavelength Study of a Complete IRAC 3.6  $\mu\text{m}$  Selected Galaxy Sample: A Fair Census of Red and Blue Populations at Redshifts 0.4-1.2. *ApJ*, 766:21, March 2013. doi: 10.1088/0004-637X/766/1/21.
- E. P. Hubble. Extragalactic nebulae. *ApJ*, 64:321–369, December 1926. doi: 10.1086/143018.
- M. Huertas-Company, F. Shankar, S. Mei, M. Bernardi, J. A. L. Aguerri, A. Meert, and V. Vikram. No Evidence for a Dependence of the Mass-Size Relation of Early-type Galaxies on Environment in the Local Universe. *ApJ*, 779:29, December 2013. doi: 10.1088/0004-637X/779/1/29.
- O. Ilbert, M. Salvato, E. Le Floc’h, H. Aussel, P. Capak, H. J. McCracken, B. Mobasher, J. Kartaltepe, N. Scoville, D. B. Sanders, S. Arnouts, K. Bundy, P. Cassata, J.-P. Kneib, A. Koekemoer, O. Le Fèvre, S. Lilly, J. Surace, Y. Taniguchi, L. Tasca, D. Thompson, L. Tresse, M. Zamojski, G. Zamorani, and E. Zucca. Galaxy Stellar Mass Assembly Between  $0.2 < z < 2$  from the S-COSMOS Survey. *ApJ*, 709:644–663, February 2010. doi: 10.1088/0004-637X/709/2/644.
- O. Ilbert, H. J. McCracken, O. Le Fèvre, P. Capak, J. Dunlop, A. Karim, M. A. Renzini, K. Caputi, S. Boissier, S. Arnouts, H. Aussel, J. Comparat, Q. Guo, P. Hudelot, J. Kartaltepe, J. P. Kneib, J. K. Krogager, E. Le Floc’h, S. Lilly, Y. Mellier, B. Milvang-Jensen, T. Moutard, M. Onodera, J. Richard, M. Salvato, D. B. Sanders, N. Scoville, J. D. Silverman, Y. Taniguchi, L. Tasca, R. Thomas, S. Toft, L. Tresse, D. Vergani, M. Wolk, and A. Zirm. Mass assembly in quiescent and star-forming galaxies since  $z \sim 4$  from UltraVISTA. *A&A*, 556:A55, August 2013. doi: 10.1051/0004-6361/201321100.
- D. H. Jones, W. Saunders, M. Colless, M. A. Read, Q. A. Parker, F. G. Watson, L. A. Campbell, D. Burkey, T. Mauch, L. Moore, M. Hartley, P. Cass, D. James, K. Russell, K. Fiegert, J. Dawe, J. Huchra, T. Jarrett, O. Lahav, J. Lucey, G. A. Mamon, D. Proust, E. M. Sadler, and K.-i. Wakamatsu. The 6dF Galaxy Survey: samples, observational techniques and the first data release. *MNRAS*, 355:747–763, December 2004. doi: 10.1111/j.1365-2966.2004.08353.x.
- G. Kauffmann, S. D. M. White, T. M. Heckman, B. Ménard, J. Brinchmann, S. Charlot, C. Tremonti, and J. Brinkmann. The environmental dependence of the relations between

- stellar mass, structure, star formation and nuclear activity in galaxies. *MNRAS*, 353:713–731, September 2004. doi: 10.1111/j.1365-2966.2004.08117.x.
- T. Kodama and R. Bower. The  $K_s$ -band luminosity and stellar mass functions of galaxies in  $z \sim 1$  clusters. *MNRAS*, 346:1–12, November 2003. doi: 10.1046/j.1365-2966.2003.07093.x.
- T. Kodama, I. Smail, F. Nakata, S. Okamura, and R. G. Bower. The Transformation of Galaxies within the Large-Scale Structure around a  $z=0.41$  Cluster. *ApJ*, 562:L9–L13, November 2001. doi: 10.1086/338100.
- A. M. Koekemoer, H. Aussel, D. Calzetti, P. Capak, M. Giavalisco, J.-P. Kneib, A. Leauthaud, O. Le Fèvre, H. J. McCracken, R. Massey, B. Mobasher, J. Rhodes, N. Scoville, and P. L. Shopbell. The COSMOS Survey: Hubble Space Telescope Advanced Camera for Surveys Observations and Data Processing. *ApJS*, 172:196–202, September 2007. doi: 10.1086/520086.
- A. M. Koekemoer, S. M. Faber, H. C. Ferguson, N. A. Grogin, D. D. Kocevski, D. C. Koo, K. Lai, J. M. Lotz, R. A. Lucas, E. J. McGrath, S. Ogaz, A. Rajan, A. G. Riess, S. A. Rodney, L. Strolger, S. Casertano, M. Castellano, T. Dahlen, M. Dickinson, T. Dolch, A. Fontana, M. Giavalisco, A. Grazian, Y. Guo, N. P. Hathi, K.-H. Huang, A. van der Wel, H.-J. Yan, V. Acquaviva, D. M. Alexander, O. Almaini, M. L. N. Ashby, M. Barden, E. F. Bell, F. Bournaud, T. M. Brown, K. I. Caputi, P. Cassata, P. J. Challis, R.-R. Chary, E. Cheung, M. Cirasuolo, C. J. Conselice, A. Roshan Cooray, D. J. Croton, E. Daddi, R. Davé, D. F. de Mello, L. de Ravel, A. Dekel, J. L. Donley, J. S. Dunlop, A. A. Dutton, D. Elbaz, G. G. Fazio, A. V. Filippenko, S. L. Finkelstein, C. Frazer, J. P. Gardner, P. M. Garnavich, E. Gawiser, R. Gruetzbauch, W. G. Hartley, B. Häussler, J. Herrington, P. F. Hopkins, J.-S. Huang, S. W. Jha, A. Johnson, J. S. Kartaltepe, A. A. Khostovan, R. P. Kirshner, C. Lani, K.-S. Lee, W. Li, P. Madau, P. J. McCarthy, D. H. McIntosh, R. J. McLure, C. McPartland, B. Mobasher, H. Moreira, A. Mortlock, L. A. Moustakas, M. Mozena, K. Nandra, J. A. Newman, J. L. Nielsen, S. Niemi, K. G. Noeske, C. J. Papovich, L. Pentericci, A. Pope, J. R. Primack, S. Ravindranath, N. A. Reddy, A. Renzini, H.-W. Rix, A. R. Robaina, D. J. Rosario, P. Rosati, S. Salimbeni, C. Scarlata, B. Siana, L. Simard, J. Smidt, D. Snyder, R. S. Somerville, H. Spinrad, A. N. Straughn, O. Telford, H. I. Teplitz, J. R. Trump, C. Vargas, C. Villforth, C. R. Wagner, P. Wandro, R. H. Wechsler, B. J. Weiner, T. Wiklind, V. Wild, G. Wilson, S. Wuyts, and M. S. Yun. CANDELS: The Cosmic Assembly Near-infrared Deep Extragalactic Legacy Survey—The Hubble Space Telescope Observations, Imaging Data Products, and Mosaics. *ApJS*, 197:36, December 2011. doi: 10.1088/0067-0049/197/2/36.

- E. Komatsu, K. M. Smith, J. Dunkley, C. L. Bennett, B. Gold, G. Hinshaw, N. Jarosik, D. Larson, M. R. Nolta, L. Page, D. N. Spergel, M. Halpern, R. S. Hill, A. Kogut, M. Limon, S. S. Meyer, N. Odegard, G. S. Tucker, J. L. Weiland, E. Wollack, and E. L. Wright. Seven-year Wilkinson Microwave Anisotropy Probe (WMAP) Observations: Cosmological Interpretation. *ApJS*, 192:18, February 2011. doi: 10.1088/0067-0049/192/2/18.
- J. Kormendy. Brightness distributions in compact and normal galaxies. II - Structure parameters of the spheroidal component. *ApJ*, 218:333–346, December 1977. doi: 10.1086/155687.
- J. E. Krick and R. A. Bernstein. Diffuse Optical Light in Galaxy Clusters. II. Correlations with Cluster Properties. *AJ*, 134:466–493, August 2007. doi: 10.1086/518787.
- M. Kriek, P. G. van Dokkum, I. Labbé, M. Franx, G. D. Illingworth, D. Marchesini, and R. F. Quadri. An Ultra-Deep Near-Infrared Spectrum of a Compact Quiescent Galaxy at  $z = 2.2$ . *ApJ*, 700:221–231, July 2009. doi: 10.1088/0004-637X/700/1/221.
- M. Kriek, I. Labbé, C. Conroy, K. E. Whitaker, P. G. van Dokkum, G. B. Brammer, M. Franx, G. D. Illingworth, D. Marchesini, A. Muzzin, R. F. Quadri, and G. Rudnick. The Spectral Energy Distribution of Post-starburst Galaxies in the NEWFIRM Medium-band Survey: A Low Contribution from TP-AGB Stars. *ApJ*, 722:L64–L69, October 2010. doi: 10.1088/2041-8205/722/1/L64.
- R. G. Kron. Photometry of a complete sample of faint galaxies. *ApJS*, 43:305–325, June 1980. doi: 10.1086/190669.
- F. Lamareille, T. Contini, J.-F. Le Borgne, J. Brinchmann, S. Charlot, and J. Richard. Spectrophotometric properties of galaxies at intermediate redshifts ( $z \sim 0.2$ – $1.0$ ). I. Sample description, photometric properties and spectral measurements. *A&A*, 448:893–906, March 2006. doi: 10.1051/0004-6361:20053601.
- C. Lani, O. Almaini, W. G. Hartley, A. Mortlock, B. Häußler, R. W. Chuter, C. Simpson, A. van der Wel, R. Grützbauch, C. J. Conselice, E. J. Bradshaw, M. C. Cooper, S. M. Faber, N. A. Grogan, D. D. Kocevski, A. M. Koekemoer, and K. Lai. Evidence for a correlation between the sizes of quiescent galaxies and local environment to  $z \sim 2$ . *MNRAS*, 435:207–221, October 2013. doi: 10.1093/mnras/stt1275.
- C. F. P. Laporte, S. D. M. White, T. Naab, and L. Gao. The growth in size and mass of cluster galaxies since  $z = 2$ . *MNRAS*, 435:901–909, October 2013. doi: 10.1093/mnras/stt912.
- M. A. Lara-López, A. Bongiovanni, J. Cepa, A. M. Pérez García, M. Sánchez-Portal, H. O. Castañeda, M. Fernández Lorenzo, and M. Pović. Study of star-forming galaxies in

- SDSS up to redshift 0.4. II. Evolution from the fundamental parameters: mass, metallicity and star formation rate. *A&A*, 519:A31, September 2010. doi: 10.1051/0004-6361/200913886.
- R. B. Larson, B. M. Tinsley, and C. N. Caldwell. The evolution of disk galaxies and the origin of S0 galaxies. *ApJ*, 237:692–707, May 1980. doi: 10.1086/157917.
- O. Le Fèvre, M. Saisse, D. Mancini, S. Brau-Nogue, O. Caputi, L. Castinel, S. D’Odorico, B. Garilli, M. Kissler-Patig, C. Lucuix, G. Mancini, A. Pauget, G. Sciarretta, M. Scodeggio, L. Tresse, and G. Vettolani. Commissioning and performances of the vlt-vimos instrument. In M. Iye and A. F. M. Moorwood, editors, *Society of Photo-Optical Instrumentation Engineers (SPIE) Conference Series*, volume 4841 of *Society of Photo-Optical Instrumentation Engineers (SPIE) Conference Series*, pages 1670–1681, March 2003. doi: 10.1117/12.460959.
- Y.-T. Lin and J. J. Mohr. K-band Properties of Galaxy Clusters and Groups: Brightest Cluster Galaxies and Intracluster Light. *ApJ*, 617:879–895, December 2004. doi: 10.1086/425412.
- Y.-T. Lin, J. J. Mohr, and S. A. Stanford. K-Band Properties of Galaxy Clusters and Groups: Luminosity Function, Radial Distribution, and Halo Occupation Number. *ApJ*, 610:745–761, August 2004. doi: 10.1086/421714.
- Y.-T. Lin, J. J. Mohr, A. H. Gonzalez, and S. A. Stanford. Evolution of the K-Band Galaxy Cluster Luminosity Function and Scaling Relations. *ApJ*, 650:L99–L102, October 2006. doi: 10.1086/508940.
- A. Longobardi, M. Arnaboldi, O. Gerhard, and R. Hanuschik. The outer regions of the giant Virgo galaxy M 87 Kinematic separation of stellar halo and intracluster light. *A&A*, 579: A135, July 2015. doi: 10.1051/0004-6361/201525773.
- A. V. Macciò, A. A. Dutton, and F. C. van den Bosch. Concentration, spin and shape of dark matter haloes as a function of the cosmological model: WMAP1, WMAP3 and WMAP5 results. *MNRAS*, 391:1940–1954, December 2008. doi: 10.1111/j.1365-2966.2008.14029.x.
- A. V. Macciò, X. Kang, F. Fontanot, R. S. Somerville, S. Koposov, and P. Monaco. Luminosity function and radial distribution of Milky Way satellites in a  $\Lambda$ CDM Universe. *MNRAS*, 402:1995–2008, March 2010. doi: 10.1111/j.1365-2966.2009.16031.x.
- D. T. Maltby, A. Aragón-Salamanca, M. E. Gray, M. Barden, B. Häußler, C. Wolf, C. Y. Peng, K. Jahnke, D. H. McIntosh, A. Böhm, and E. van Kampen. The environmental dependence of the stellar-mass-size relation in STAGES galaxies. *MNRAS*, 402:282–294, February 2010. doi: 10.1111/j.1365-2966.2009.15953.x.

- E. M. Malumuth and G. A. Kriss. Dynamics of the poor clusters MKW 4 and AWM 4. *ApJ*, 308:10–22, September 1986. doi: 10.1086/164474.
- G. A. Mamon, A. Biviano, and G. Murante. The universal distribution of halo interlopers in projected phase space. Bias in galaxy cluster concentration and velocity anisotropy? *A&A*, 520:A30, October 2010.
- G. A. Mamon, A. Biviano, and G. Boué. MAMPOSSt: Modelling Anisotropy and Mass Profiles of Observed Spherical Systems - I. Gaussian 3D velocities. *MNRAS*, 429:3079–3098, March 2013. doi: 10.1093/mnras/sts565.
- C. L. Mancone, T. Baker, A. H. Gonzalez, M. L. N. Ashby, S. A. Stanford, M. Brodwin, P. R. M. Eisenhardt, G. Snyder, D. Stern, and E. L. Wright. The Faint End of the Cluster-galaxy Luminosity Function at High Redshift. *ApJ*, 761:141, December 2012. doi: 10.1088/0004-637X/761/2/141.
- C. Maraston, E. Daddi, A. Renzini, A. Cimatti, M. Dickinson, C. Papovich, A. Pasquali, and N. Pirzkal. Evidence for TP-AGB Stars in High-Redshift Galaxies, and Their Effect on Deriving Stellar Population Parameters. *ApJ*, 652:85–96, November 2006. doi: 10.1086/508143.
- N. Martinet, F. Durret, L. Guennou, C. Adami, A. Biviano, M. P. Ulmer, D. Clowe, C. Halliday, O. Ilbert, I. Márquez, and M. Schirmer. The evolution of the cluster optical galaxy luminosity function between  $z = 0.4$  and  $0.9$  in the DAFT/FADA survey. *A&A*, 575:A116, March 2015. doi: 10.1051/0004-6361/201423796.
- I. G. McCarthy, C. S. Frenk, A. S. Font, C. G. Lacey, R. G. Bower, N. L. Mitchell, M. L. Balogh, and T. Theuns. Ram pressure stripping the hot gaseous haloes of galaxies in groups and clusters. *MNRAS*, 383:593–605, January 2008. doi: 10.1111/j.1365-2966.2007.12577.x.
- H. J. McCracken, B. Milvang-Jensen, J. Dunlop, M. Franx, J. P. U. Fynbo, O. Le Fèvre, J. Holt, K. I. Caputi, Y. Goranova, F. Buitrago, J. Emerson, W. Freudling, O. Herent, P. Hudelot, C. López-Sanjuan, F. Magnard, A. Muzzin, Y. Mellier, P. Møller, K. K. Nilsson, W. Sutherland, L. Tasca, and J. Zabl. UltraVISTA: A VISTA Public Survey of the Distant Universe. *The Messenger*, 154:29–31, December 2013.
- N. Menci, F. Fiore, and A. Lamastra. Galaxy formation in warm dark matter cosmology. *MNRAS*, 421:2384–2394, April 2012. doi: 10.1111/j.1365-2966.2012.20470.x.
- A. Mercurio, M. Girardi, W. Boschin, P. Merluzzi, and G. Busarello. Structure and evolution of galaxy clusters: Internal dynamics of ABCG 209 at  $z; \sim 0.21$ . *A&A*, 397:431–443, January 2003. doi: 10.1051/0004-6361:20021495.

- A. Mercurio, M. Massarotti, Paola Merluzzi, M. Girardi, F. La Barbera, et al. Optical luminosity functions of the Abell galaxy cluster ABCG 209 at  $z=0.21$ . *Astron.Astrophys.*, 408: 57–66, 2003. doi: 10.1051/0004-6361:20030971.
- A. Mercurio, F. La Barbera, C. P. Haines, P. Merluzzi, G. Busarello, and M. Capaccioli. Global properties of the rich cluster ABCG209 at  $z \sim 0.2$ . Spectroscopic and photometric catalogue. *MNRAS*, 387:1374–1390, July 2008. doi: 10.1111/j.1365-2966.2008.13253.x.
- P. Merluzzi, A. Mercurio, C. P. Haines, R. J. Smith, G. Busarello, and J. R. Lucey. ACCESS: NIR luminosity function and stellar mass function of galaxies in the Shapley supercluster environment. *MNRAS*, 402:753–766, February 2010. doi: 10.1111/j.1365-2966.2009.15929.x.
- D. Merritt. Relaxation and tidal stripping in rich clusters of galaxies. II. Evolution of the luminosity distribution. *ApJ*, 276:26–37, January 1984. doi: 10.1086/161590.
- J. Merten, M. Meneghetti, M. Postman, K. Umetsu, A. Zitrin, et al. CLASH: The Concentration-Mass Relation of Galaxy Clusters. 2014.
- S. L. Meyer. *Data Analysis for Scientists and Engineers*. John Wiley & Sons Inc., New York, 1975.
- J. C. Mihos. Interactions and Mergers of Cluster Galaxies. *Clusters of Galaxies: Probes of Cosmological Structure and Galaxy Evolution*, page 277, 2004.
- J. C. Mihos, P. Harding, J. Feldmeier, and H. Morrison. Diffuse Light in the Virgo Cluster. *ApJ*, 631:L41–L44, September 2005. doi: 10.1086/497030.
- R. H. Miller. Flyby - Numerical experiments on a galaxy orbiting within a galaxy cluster. *A&A*, 167:41–52, October 1986.
- S. Miyazaki, M. Sekiguchi, K. Imi, N. Okada, F. Nakata, and Y. Komiyama. Characterization and mosaicking of CCDs and the applications to the SUBARU wide-field camera (Suprime-Cam). In S. D’Odorico, editor, *Optical Astronomical Instrumentation*, volume 3355 of *Society of Photo-Optical Instrumentation Engineers (SPIE) Conference Series*, pages 363–374, July 1998.
- J. J. Mohr, R. Armstrong, E. Bertin, G. Daues, S. Desai, M. Gower, R. Gruendl, W. Hanlon, N. Kuropatkin, H. Lin, J. Marriner, D. Petravic, I. Sevilla, M. Swanson, T. Tomashek, D. Tucker, and B. Yanny. The Dark Energy Survey data processing and calibration system. In *Society of Photo-Optical Instrumentation Engineers (SPIE) Conference Series*, volume 8451

- of *Society of Photo-Optical Instrumentation Engineers (SPIE) Conference Series*, page 84510D, September 2012. doi: 10.1117/12.926785.
- M. Montes and I. Trujillo. Intracuster Light at the Frontier: A2744. *ApJ*, 794:137, October 2014. doi: 10.1088/0004-637X/794/2/137.
- B. Moore, N. Katz, G. Lake, A. Dressler, and A. Oemler. Galaxy harassment and the evolution of clusters of galaxies. *Nature*, 379:613–616, February 1996. doi: 10.1038/379613a0.
- B. Moore, F. Governato, T. Quinn, J. Stadel, and G. Lake. Resolving the Structure of Cold Dark Matter Halos. *ApJ*, 499:L5, May 1998. doi: 10.1086/311333.
- B. Moore, G. Lake, T. Quinn, and J. Stadel. On the survival and destruction of spiral galaxies in clusters. *MNRAS*, 304:465–474, April 1999. doi: 10.1046/j.1365-8711.1999.02345.x.
- A. Mortlock, C. J. Conselice, A. F. L. Bluck, A. E. Bauer, R. Grützbauch, F. Buitrago, and J. Owers. A deep probe of the galaxy stellar mass functions at  $z \sim 1-3$  with the GOODS NICMOS Survey. *MNRAS*, 413:2845–2859, June 2011. doi: 10.1111/j.1365-2966.2011.18357.x.
- A. Mortlock, C. J. Conselice, W. G. Hartley, K. Duncan, C. Lani, J. R. Owers, O. Almaini, A. v. d. Wel, K.-H. Huang, M. L. N. Ashby, S. P. Willner, A. Fontana, A. Dekel, A. M. Koekemoer, H. C. Ferguson, S. M. Faber, N. A. Grogin, and D. D. Kocevski. Deconstructing the galaxy stellar mass function with UKIDSS and CANDELS: the impact of colour, structure and environment. *MNRAS*, 447:2–24, February 2015. doi: 10.1093/mnras/stu2403.
- J. Moustakas, A. L. Coil, J. Aird, M. R. Blanton, R. J. Cool, D. J. Eisenstein, A. J. Mendez, K. C. Wong, G. Zhu, and S. Arnouts. PRIMUS: Constraints on Star Formation Quenching and Galaxy Merging, and the Evolution of the Stellar Mass Function from  $z = 0-1$ . *ApJ*, 767:50, April 2013. doi: 10.1088/0004-637X/767/1/50.
- E. Munari, A. Biviano, S. Borgani, G. Murante, and D. Fabjan. The relation between velocity dispersion and mass in simulated clusters of galaxies: dependence on the tracer and the baryonic physics. *MNRAS*, 430:2638–2649, April 2013. doi: 10.1093/mnras/stt049.
- G. Murante, M. Arnaboldi, O. Gerhard, S. Borgani, L. M. Cheng, A. Diaferio, K. Dolag, L. Moscardini, G. Tormen, L. Tornatore, and P. Tozzi. The Diffuse Light in Simulations of Galaxy Clusters. *ApJ*, 607:L83–L86, June 2004. doi: 10.1086/421348.



- G. Murante, M. Giovalli, O. Gerhard, M. Arnaboldi, S. Borgani, and K. Dolag. The importance of mergers for the origin of intracluster stars in cosmological simulations of galaxy clusters. *MNRAS*, 377:2–16, May 2007a. doi: 10.1111/j.1365-2966.2007.11568.x.
- G. Murante, M. Giovalli, O. Gerhard, M. Arnaboldi, S. Borgani, and K. Dolag. The importance of mergers for the origin of intracluster stars in cosmological simulations of galaxy clusters. *MNRAS*, 377:2–16, May 2007b. doi: 10.1111/j.1365-2966.2007.11568.x.
- A. Muzzin, H. K. C. Yee, P. B. Hall, E. Ellingson, and H. Lin. Near-Infrared Properties of Moderate-Redshift Galaxy Clusters: Luminosity Functions and Density Profiles. *ApJ*, 659: 1106–1124, April 2007. doi: 10.1086/511669.
- A. Muzzin, G. Wilson, M. Lacy, H. K. C. Yee, and S. A. Stanford. The Evolution of Dusty Star Formation and Stellar Mass Assembly in Clusters: Results from the IRAC 3.6, 4.5, 5.8, and 8.0  $\mu\text{m}$  Cluster Luminosity Functions. *ApJ*, 686:966–994, October 2008. doi: 10.1086/591542.
- A. Muzzin, D. Marchesini, M. Stefanon, M. Franx, H. J. McCracken, B. Milvang-Jensen, J. S. Dunlop, J. P. U. Fynbo, G. Brammer, I. Labbé, and P. G. van Dokkum. The Evolution of the Stellar Mass Functions of Star-forming and Quiescent Galaxies to  $z = 4$  from the COSMOS/UltraVISTA Survey. *ApJ*, 777:18, November 2013a. doi: 10.1088/0004-637X/777/1/18.
- A. Muzzin, D. Marchesini, M. Stefanon, M. Franx, B. Milvang-Jensen, J. S. Dunlop, J. P. U. Fynbo, G. Brammer, I. Labbé, and P. van Dokkum. A Public  $K_s$ -selected Catalog in the COSMOS/ULTRA VISTA Field: Photometry, Photometric Redshifts, and Stellar Population Parameters. *ApJS*, 206:8, May 2013b. doi: 10.1088/0067-0049/206/1/8.
- J. F. Navarro, C. S. Frenk, and S. D. M. White. A universal density profile from hierarchical clustering. *ApJ*, 490:493–508, December 1997a.
- J. F. Navarro, C. S. Frenk, and S. D. M. White. A Universal Density Profile from Hierarchical Clustering. *ApJ*, 490:493, December 1997b. doi: 10.1086/304888.
- J. Negroponte and S. D. M. White. Simulations of mergers between disc-halo galaxies. *MNRAS*, 205:1009–1029, December 1983.
- M. Nonino, M. Dickinson, P. Rosati, A. Grazian, N. Reddy, S. Cristiani, M. Giavalisco, H. Kuntschner, E. Vanzella, E. Daddi, R. A. E. Fosbury, and C. Cesarsky. Deep U Band and R Imaging of GOODS-South: Observations, Data Reduction and First Results. *ApJS*, 183:244–260, August 2009. doi: 10.1088/0067-0049/183/2/244.

- P. E. J. Nulsen. Transport processes and the stripping of cluster galaxies. *MNRAS*, 198: 1007–1016, March 1982.
- A. Oemler, Jr. The Systematic Properties of Clusters of Galaxies. Photometry of 15 Clusters. *ApJ*, 194:1–20, November 1974. doi: 10.1086/153216.
- N. Okabe, G. P. Smith, K. Umetsu, M. Takada, and T. Futamase. LoCuSS: The Mass Density Profile of Massive Galaxy Clusters at  $z = 0.2$ . *ApJ*, 769:L35, June 2013. doi: 10.1088/2041-8205/769/2/L35.
- G. G. C. Palumbo, P. Saracco, P. Hickson, and C. Mendes de Oliveira. Environment of compact groups of galaxies. *AJ*, 109:1476–1484, April 1995. doi: 10.1086/117377.
- J.A. Peacock. *Cosmological Physics*. Cambridge Astrophysics Series. Cambridge University Press, 1999. ISBN 9780521422703.
- C. Y. Peng, L. C. Ho, C. D. Impey, and H.-W. Rix. Detailed Decomposition of Galaxy Images. II. Beyond Axisymmetric Models. *AJ*, 139:2097–2129, June 2010a. doi: 10.1088/0004-6256/139/6/2097.
- Y.-j. Peng, S. J. Lilly, K. Kovač, M. Bolzonella, L. Pozzetti, A. Renzini, G. Zamorani, O. Ilbert, C. Knobel, A. Iovino, C. Maier, O. Cucciati, L. Tasca, C. M. Carollo, J. Silverman, P. Kampczyk, L. de Ravel, D. Sanders, N. Scoville, T. Contini, V. Mainieri, M. Scodeggio, J.-P. Kneib, O. Le Fèvre, S. Bardelli, A. Bongiorno, K. Caputi, G. Coppia, S. de la Torre, P. Franzetti, B. Garilli, F. Lamareille, J.-F. Le Borgne, V. Le Brun, M. Mignoli, E. Perez Montero, R. Pello, E. Ricciardelli, M. Tanaka, L. Tresse, D. Vergani, N. Welikal, E. Zucca, P. Oesch, U. Abbas, L. Barnes, R. Bordoloi, D. Bottini, A. Cappi, P. Casata, A. Cimatti, M. Fumana, G. Hasinger, A. Koekemoer, A. Leauthaud, D. Maccagni, C. Marinoni, H. McCracken, P. Memeo, B. Meneux, P. Nair, C. Porciani, V. Presotto, and R. Scaramella. Mass and Environment as Drivers of Galaxy Evolution in SDSS and zCOSMOS and the Origin of the Schechter Function. *ApJ*, 721:193–221, September 2010b. doi: 10.1088/0004-637X/721/1/193.
- A. Pisani. A Non-Parametric and Scale-Independent Method for Cluster Analysis - Part One - the Univariate Case. *MNRAS*, 265:706, December 1993.
- B. M. Poggianti, R. Calvi, D. Bindoni, M. D’Onofrio, A. Moretti, T. Valentinuzzi, G. Fasano, J. Fritz, G. De Lucia, B. Vulcani, D. Bettoni, M. Gullieuszik, and A. Omizzolo. Superdense Galaxies and the Mass-Size Relation at Low Redshift. *ApJ*, 762:77, January 2013. doi: 10.1088/0004-637X/762/2/77.

- P. Popesso, A. Biviano, H. Böhringer, and M. Romaniello. RASS-SDSS Galaxy cluster survey. IV. A ubiquitous dwarf galaxy population in clusters. *A&A*, 445:29–42, January 2006a. doi: 10.1051/0004-6361:20052954.
- P. Popesso, A. Biviano, H. Böhringer, and M. Romaniello. RASS-SDSS Galaxy cluster survey. IV. A ubiquitous dwarf galaxy population in clusters. *A&A*, 445:29–42, January 2006b. doi: 10.1051/0004-6361:20052954.
- M. Postman and M. J. Geller. The morphology-density relation - The group connection. *ApJ*, 281:95–99, June 1984. doi: 10.1086/162078.
- M. Postman, M. Franx, N. J. G. Cross, B. Holden, H. C. Ford, G. D. Illingworth, T. Goto, R. Demarco, P. Rosati, J. P. Blakeslee, K.-V. Tran, N. Benítez, M. Clampin, G. F. Hartig, N. Homeier, D. R. Ardila, F. Bartko, R. J. Bouwens, L. D. Bradley, T. J. Broadhurst, R. A. Brown, C. J. Burrows, E. S. Cheng, P. D. Feldman, D. A. Golimowski, C. Gronwall, L. Infante, R. A. Kimble, J. E. Krist, M. P. Lesser, A. R. Martel, S. Mei, F. Menanteau, G. R. Meurer, G. K. Miley, V. Motta, M. Sirianni, W. B. Sparks, H. D. Tran, Z. I. Tsvetanov, R. L. White, and W. Zheng. The Morphology-Density Relation in  $z \sim 1$  Clusters. *ApJ*, 623:721–741, April 2005. doi: 10.1086/428881.
- M. Postman, D. Coe, N. Benítez, L. Bradley, T. Broadhurst, M. Donahue, H. Ford, O. Graur, G. Graves, S. Jouvel, A. Koekemoer, D. Lemze, E. Medezinski, A. Molino, L. Moustakas, S. Ogaz, A. Riess, S. Rodney, P. Rosati, K. Umetsu, W. Zheng, A. Zitrin, M. Bartelmann, R. Bouwens, N. Czakon, S. Golwala, O. Host, L. Infante, S. Jha, Y. Jimenez-Teja, D. Kelson, O. Lahav, R. Lazkoz, D. Maoz, C. McCully, P. Melchior, M. Meneghetti, J. Merten, J. Moustakas, M. Nonino, B. Patel, E. Regös, J. Sayers, S. Seitz, and A. Van der Wel. The Cluster Lensing and Supernova Survey with Hubble: An Overview. *ApJS*, 199:25, April 2012. doi: 10.1088/0067-0049/199/2/25.
- L. Pozzetti, M. Bolzonella, E. Zucca, G. Zamorani, S. Lilly, A. Renzini, M. Moresco, M. Mignoli, P. Cassata, L. Tasca, F. Lamareille, C. Maier, B. Meneux, C. Halliday, P. Oesch, D. Vergani, K. Caputi, K. Kovač, A. Cimatti, O. Cucciati, A. Iovino, Y. Peng, M. Carollo, T. Contini, J.-P. Kneib, O. Le Fèvre, V. Mainieri, M. Scodeggio, S. Bardelli, A. Bongiorno, G. Coppia, S. de la Torre, L. de Ravel, P. Franzetti, B. Garilli, P. Kampczyk, C. Knobel, J.-F. Le Borgne, V. Le Brun, R. Pellò, E. Perez Montero, E. Ricciardelli, J. D. Silverman, M. Tanaka, L. Tresse, U. Abbas, D. Bottini, A. Cappi, L. Guzzo, A. M. Koekemoer, A. Leauthaud, D. Maccagni, C. Marinoni, H. J. McCracken, P. Memeo, C. Porciani, R. Scaramella, C. Scarlata, and N. Scoville. zCOSMOS - 10k-bright spectroscopic sample. The bimodality in the galaxy stellar mass function: exploring its evolution with redshift. *A&A*, 523:A13, November 2010. doi: 10.1051/0004-6361/200913020.

- V. Presotto, M. Girardi, M. Nonino, A. Mercurio, C. Grillo, P. Rosati, A. Biviano, M. Annunziatella, I. Balestra, W. Cui, B. Sartoris, D. Lemze, B. Ascaso, J. Moustakas, H. Ford, A. Fritz, O. Czoske, S. Ettori, U. Kuchner, M. Lombardi, C. Maier, E. Medezinski, A. Molino, M. Scodeggio, V. Strazzullo, P. Tozzi, B. Ziegler, M. Bartelmann, N. Benitez, L. Bradley, M. Brescia, T. Broadhurst, D. Coe, M. Donahue, R. Gobat, G. Graves, D. Kelson, A. Koekoer, P. Melchior, M. Meneghetti, J. Merten, L. Moustakas, E. Munari, M. Postman, E. Reg  s, S. Seitz, K. Umetsu, W. Zheng, and A. Zitrin. Intra Cluster Light properties in the CLASH-VLT cluster MACSJ1206.2-0847. March 2014. arXiv:1403.4979.
- W. H. Press and P. Schechter. Formation of Galaxies and Clusters of Galaxies by Self-Similar Gravitational Condensation. *ApJ*, 187:425–438, February 1974. doi: 10.1086/152650.
- W. H. Press, G. B. Rybicki, and D. P. Schneider. Properties of high-redshift Lyman-alpha clouds. I - Statistical analysis of the Schneider-Schmidt-Gunn quasars. *ApJ*, 414:64–81, September 1993. doi: 10.1086/173057.
- E. Puchwein, V. Springel, D. Sijacki, and K. Dolag. Intracluster stars in simulations with active galactic nucleus feedback. *MNRAS*, 406:936–951, August 2010. doi: 10.1111/j.1365-2966.2010.16786.x.
- C. W. Purcell, J. S. Bullock, and A. R. Zentner. Shredded Galaxies as the Source of Diffuse Intrahalo Light on Varying Scales. *ApJ*, 666:20–33, September 2007. doi: 10.1086/519787.
- V. Quilis, B. Moore, and R. Bower. Gone with the Wind: The Origin of S0 Galaxies in Clusters. *Science*, 288:1617–1620, June 2000. doi: 10.1126/science.288.5471.1617.
- H.-W. Rix, M. Barden, S. V. W. Beckwith, E. F. Bell, A. Borch, J. A. R. Caldwell, B. H  ussler, K. Jahnke, S. Jogee, D. H. McIntosh, K. Meisenheimer, C. Y. Peng, S. F. Sanchez, R. S. Somerville, L. Wisotzki, and C. Wolf. GEMS: Galaxy Evolution from Morphologies and SEDs. *ApJS*, 152:163–173, June 2004. doi: 10.1086/420885.
- C. S. Rudick, J. C. Mihos, and C. McBride. The Formation and Evolution of Intracluster Light. *ApJ*, 648:936–946, September 2006. doi: 10.1086/506176.
- C. S. Rudick, J. C. Mihos, L. H. Frey, and C. K. McBride. Tidal Streams of Intracluster Light. *ApJ*, 699:1518–1529, July 2009. doi: 10.1088/0004-637X/699/2/1518.
- G. Rudnick, A. von der Linden, R. Pell  , A. Arag  n-Salamanca, D. Marchesini, D. Clowe, G. De Lucia, C. Halliday, P. Jablonka, B. Milvang-Jensen, B. Poggianti, R. Saglia, L. Simard, S. White, and D. Zaritsky. The Rest-frame Optical Luminosity Function of Cluster Galaxies at  $z < 0.8$  and the Assembly of the Cluster Red Sequence. *ApJ*, 700:1559–1588, August 2009. doi: 10.1088/0004-637X/700/2/1559.

- R. Sánchez-Janssen, J. A. L. Aguerri, and C. Muñoz-Tuñón. Properties of the Dwarf Galaxy Population in Galaxy Clusters. *ApJ*, 679:L77–L80, June 2008. doi: 10.1086/589617.
- P. Schechter. An analytic expression for the luminosity function for galaxies. *ApJ*, 203:297–306, January 1976. doi: 10.1086/154079.
- M. Scodeggio, P. Franzetti, B. Garilli, A. Zanichelli, S. Paltani, D. Maccagni, D. Bottini, V. Le Brun, T. Contini, R. Scaramella, C. Adami, S. Bardelli, E. Zucca, L. Tresse, O. Ilbert, S. Foucaud, A. Iovino, R. Merighi, G. Zamorani, I. Gavignaud, D. Rizzo, H. J. McCracken, O. Le Fèvre, J. P. Picat, G. Vettolani, M. Arnaboldi, S. Arnouts, M. Bolzonella, A. Cappi, S. Charlot, P. Ciliegi, L. Guzzo, B. Marano, C. Marinoni, G. Mathez, A. Mazure, B. Meneux, R. Pellò, A. Pollo, L. Pozzetti, and M. Radovich. The VVDS Data-Reduction Pipeline: Introducing VIPGI, the VIMOS Interactive Pipeline and Graphical Interface. *PASP*, 117: 1284–1295, November 2005. doi: 10.1086/496937.
- M. Scodeggio, D. Vergani, O. Cucciati, A. Iovino, P. Franzetti, B. Garilli, F. Lamareille, M. Bolzonella, L. Pozzetti, U. Abbas, C. Marinoni, T. Contini, D. Bottini, V. Le Brun, O. Le Fèvre, D. Maccagni, R. Scaramella, L. Tresse, G. Vettolani, A. Zanichelli, C. Adami, S. Arnouts, S. Bardelli, A. Cappi, S. Charlot, P. Ciliegi, S. Foucaud, I. Gavignaud, L. Guzzo, O. Ilbert, H. J. McCracken, B. Marano, A. Mazure, B. Meneux, R. Merighi, S. Paltani, R. Pellò, A. Pollo, M. Radovich, G. Zamorani, E. Zucca, M. Bondi, A. Bongiorno, J. Brinchmann, S. de La Torre, L. de Ravel, L. Gregorini, P. Memeo, E. Perez-Montero, Y. Mellier, S. Tempurin, and C. J. Walcher. The Vimos VLT Deep Survey. Stellar mass segregation and large-scale galaxy environment in the redshift range  $0.2 < z < 1.4$ . *A&A*, 501:21–27, July 2009. doi: 10.1051/0004-6361/200810511.
- N. Scoville, H. Aussel, A. Benson, A. Blain, D. Calzetti, P. Capak, R. S. Ellis, A. El-Zant, A. Finoguenov, M. Giavalisco, L. Guzzo, G. Hasinger, J. Koda, O. Le Fèvre, R. Massey, H. J. McCracken, B. Mobasher, A. Renzini, J. Rhodes, M. Salvato, D. B. Sanders, S. S. Sasaki, E. Schinnerer, K. Sheth, P. L. Shopbell, Y. Taniguchi, J. E. Taylor, and D. J. Thompson. Large Structures and Galaxy Evolution in COSMOS at  $z < 1.1$ . *ApJS*, 172:150–181, September 2007. doi: 10.1086/516751.
- F. Shankar, F. Marulli, M. Bernardi, S. Mei, A. Meert, and V. Vikram. Size evolution of spheroids in a hierarchical Universe. *MNRAS*, 428:109–128, January 2013. doi: 10.1093/mnras/sts001.
- S. Shen, H. J. Mo, S. D. M. White, M. R. Blanton, G. Kauffmann, W. Voges, J. Brinkmann, and I. Csabai. The size distribution of galaxies in the Sloan Digital Sky Survey. *MNRAS*, 343: 978–994, August 2003. doi: 10.1046/j.1365-8711.2003.06740.x.

- B. W. Silverman. *Density estimation for statistics and data analysis*. 1986.
- R. Smith, J. I. Davies, and A. H. Nelson. How effective is harassment on infalling late-type dwarfs? *MNRAS*, 405:1723–1735, July 2010. doi: 10.1111/j.1365-2966.2010.16545.x.
- R. Smith, R. Sanchez-Janssen, M. A. Beasley, G. N. Candlish, B. K. Gibson, T. H. Puzia, J. Janz, A. Knebe, J. A. L. Aguerri, T. Lisker, G. Hensler, M. Fellhauer, L. Ferrarese, and S. K. Yi. The Sensitivity of Harassment to Orbit: Mass Loss from Early-Type Dwarfs in Galaxy Clusters. *ArXiv e-prints*, September 2015.
- D. Sobral, P. N. Best, I. Smail, B. Mobasher, J. Stott, and D. Nisbet. The stellar mass function of star-forming galaxies and the mass-dependent SFR function since  $z = 2.23$  from HiZELS. *MNRAS*, 437:3516–3528, February 2014. doi: 10.1093/mnras/stt2159.
- J. M. Solanes and E. Salvador-Solé. Analytical anisotropic models of clusters of galaxies. *A&A*, 234:93–98, August 1990.
- J. M. Solanes, A. Manrique, C. García-Gómez, G. González-Casado, R. Giovanelli, and M. P. Haynes. The H I Content of Spirals. II. Gas Deficiency in Cluster Galaxies. *ApJ*, 548: 97–113, February 2001. doi: 10.1086/318672.
- L. Spitzer, Jr. and W. Baade. Stellar Populations and Collisions of Galaxies. *ApJ*, 113:413, March 1951. doi: 10.1086/145406.
- M. Stefanon and D. Marchesini. The evolution of the rest-frame J- and H-band luminosity function of galaxies to  $z=3.5$ . *MNRAS*, 429:881–894, February 2013. doi: 10.1093/mnras/sts388.
- V. Strazzullo, P. Rosati, S. A. Stanford, C. Lidman, M. Nonino, R. Demarco, P. E. Eisenhardt, S. Ettori, V. Mainieri, and S. Toft. The near-infrared luminosity function of cluster galaxies beyond redshift one. *A&A*, 450:909–923, May 2006. doi: 10.1051/0004-6361:20054341.
- J. E. Taylor and A. Babul. The evolution of substructure in galaxy, group and cluster haloes - I. Basic dynamics. *MNRAS*, 348:811–830, March 2004. doi: 10.1111/j.1365-2966.2004.07395.x.
- M. B. Taylor. STILTS - A Package for Command-Line Processing of Tabular Data. In C. Gabriel, C. Arviset, D. Ponz, and S. Enrique, editors, *Astronomical Data Analysis Software and Systems XV*, volume 351 of *Astronomical Society of the Pacific Conference Series*, page 666, July 2006.

- A. Toomre and J. Toomre. Galactic Bridges and Tails. *ApJ*, 178:623–666, December 1972. doi: 10.1086/151823.
- T. Treu, R. S. Ellis, J.-P. Kneib, A. Dressler, I. Smail, O. Czoske, A. Oemler, and P. Natarajan. A Wide-Field Hubble Space Telescope Study of the Cluster Cl 0024+16 at  $z = 0.4$ . I. Morphological Distributions to 5 Mpc Radius. *ApJ*, 591:53–78, July 2003. doi: 10.1086/375314.
- R. B. Tully and J. R. Fisher. A new method of determining distances to galaxies. *A&A*, 54: 661–673, February 1977.
- R. B. Tully, J. R. Mould, and M. Aaronson. A color-magnitude relation for spiral galaxies. *ApJ*, 257:527–537, June 1982. doi: 10.1086/160009.
- K. Umetsu, T. Broadhurst, A. Zitrin, E. Medezinski, D. Coe, and M. Postman. A Precise Cluster Mass Profile Averaged from the Highest-quality Lensing Data. *ApJ*, 738:41, September 2011. doi: 10.1088/0004-637X/738/1/41.
- K. Umetsu, E. Medezinski, M. Nonino, J. Merten, A. Zitrin, A. Molino, C. Grillo, M. Carrasco, M. Donahue, A. Mahdavi, D. Coe, M. Postman, A. Koekemoer, N. Czakon, J. Sayers, T. Mroczkowski, S. Golwala, P. M. Koch, K.-Y. Lin, S. M. Molnar, P. Rosati, I. Balestra, A. Mercurio, M. Scodeggio, A. Biviano, T. Anguita, L. Infante, G. Seidel, I. Sendra, S. Jouvel, O. Host, D. Lemze, T. Broadhurst, M. Meneghetti, L. Moustakas, M. Bartelmann, N. Benítez, R. Bouwens, L. Bradley, H. Ford, Y. Jiménez-Teja, D. Kelson, O. Lahav, P. Melchior, J. Moustakas, S. Ogaz, S. Seitz, and W. Zheng. CLASH: Mass Distribution in and around MACS J1206.2-0847 from a Full Cluster Lensing Analysis. *ApJ*, 755:56, August 2012. doi: 10.1088/0004-637X/755/1/56.
- T. Valentinuzzi, J. Fritz, B. M. Poggianti, A. Cava, D. Bettoni, G. Fasano, M. D’Onofrio, W. J. Couch, A. Dressler, M. Moles, A. Moretti, A. Omizzolo, P. Kjærgaard, E. Vanzella, and J. Varela. Superdense Massive Galaxies in Wings Local Clusters. *ApJ*, 712:226–237, March 2010. doi: 10.1088/0004-637X/712/1/226.
- M. Valluri. A study of the environmental influences on spiral galaxies in clusters. *Bulletin of the Astronomical Society of India*, 21:377–378, September 1993.
- M. Valluri and C. J. Jog. Collisional removal of H I from the inner disks of Virgo Cluster galaxies. *ApJ*, 357:367–372, July 1990. doi: 10.1086/168927.
- R. F. J. van der Burg, A. Muzzin, H. Hoekstra, C. Lidman, A. Rettura, G. Wilson, H. K. C. Yee, H. Hildebrandt, D. Marchesini, M. Stefanon, R. Demarco, and K. Kuijken. The environmental dependence of the stellar mass function at  $z \sim 1$ . Comparing cluster and

- field between the GCLASS and UltraVISTA surveys. *A&A*, 557:A15, September 2013. doi: 10.1051/0004-6361/201321237.
- A. van der Wel, Y.-Y. Chang, E. F. Bell, B. P. Holden, H. C. Ferguson, M. Giavalisco, H.-W. Rix, R. Skelton, K. Whitaker, I. Momcheva, G. Brammer, S. A. Kassin, M. Martig, A. Dekel, D. Ceverino, D. C. Koo, M. Mozena, P. G. van Dokkum, M. Franx, S. M. Faber, and J. Primack. Geometry of Star-forming Galaxies from SDSS, 3D-HST, and CANDELS. *ApJ*, 792:L6, September 2014a. doi: 10.1088/2041-8205/792/1/L6.
- A. van der Wel, M. Franx, P. G. van Dokkum, R. E. Skelton, I. G. Momcheva, K. E. Whitaker, G. B. Brammer, E. F. Bell, H.-W. Rix, S. Wuyts, H. C. Ferguson, B. P. Holden, G. Barro, A. M. Koekemoer, Y.-Y. Chang, E. J. McGrath, B. Häussler, A. Dekel, P. Behroozi, M. Fumagalli, J. Leja, B. F. Lundgren, M. V. Maseda, E. J. Nelson, D. A. Wake, S. G. Patel, I. Labbé, S. M. Faber, N. A. Grogin, and D. D. Kocevski. 3D-HST+CANDELS: The Evolution of the Galaxy Size-Mass Distribution since  $z = 3$ . *ApJ*, 788:28, June 2014b. doi: 10.1088/0004-637X/788/1/28.
- A. Vazdekis, P. Sánchez-Blázquez, J. Falcón-Barroso, A. J. Cenarro, M. A. Beasley, N. Cardiel, J. Gorgas, and R. F. Peletier. Evolutionary stellar population synthesis with MILES - I. The base models and a new line index system. *MNRAS*, 404:1639–1671, June 2010. doi: 10.1111/j.1365-2966.2010.16407.x.
- B. Vulcani, B. M. Poggianti, A. Aragón-Salamanca, G. Fasano, G. Rudnick, T. Valentinuzzi, A. Dressler, D. Bettoni, A. Cava, M. D’Onofrio, J. Fritz, A. Moretti, A. Omizzolo, and J. Varela. Galaxy stellar mass functions of different morphological types in clusters, and their evolution between  $z = 0.8$  and 0. *MNRAS*, 412:246–268, March 2011. doi: 10.1111/j.1365-2966.2010.17904.x.
- B. Vulcani, B. M. Poggianti, G. Fasano, V. Desai, A. Dressler, A. Oemler, R. Calvi, M. D’Onofrio, and A. Moretti. The importance of the local density in shaping the galaxy stellar mass functions. *MNRAS*, 420:1481–1494, February 2012. doi: 10.1111/j.1365-2966.2011.20135.x.
- B. Vulcani, B. M. Poggianti, A. Oemler, A. Dressler, A. Aragón-Salamanca, G. De Lucia, A. Moretti, M. Gladders, L. Abramson, and C. Halliday. The galaxy stellar mass function and its evolution with time show no dependence on global environment. *A&A*, 550:A58, February 2013. doi: 10.1051/0004-6361/201118388.
- B. Vulcani, G. De Lucia, B. M. Poggianti, K. Bundy, S. More, and R. Calvi. What do Simulations Predict for the Galaxy Stellar Mass Function and its Evolution in Different Environments? *ApJ*, 788:57, June 2014. doi: 10.1088/0004-637X/788/1/57.



- S. M. Weinmann, F. C. van den Bosch, X. Yang, and H. J. Mo. Properties of galaxy groups in the Sloan Digital Sky Survey - I. The dependence of colour, star formation and morphology on halo mass. *MNRAS*, 366:2–28, February 2006. doi: 10.1111/j.1365-2966.2005.09865.x.
- M. W. Werner, T. L. Roellig, F. J. Low, G. H. Rieke, M. Rieke, W. F. Hoffmann, E. Young, J. R. Houck, B. Brandl, G. G. Fazio, J. L. Hora, R. D. Gehrz, G. Helou, B. T. Soifer, J. Stauffer, J. Keene, P. Eisenhardt, D. Gallagher, T. N. Gautier, W. Irace, C. R. Lawrence, L. Simmons, J. E. Van Cleve, M. Jura, E. L. Wright, and D. P. Cruikshank. The Spitzer Space Telescope Mission. *ApJS*, 154:1–9, September 2004. doi: 10.1086/422992.
- S. D. M. White. Dynamical friction in spherical clusters. *MNRAS*, 174:19–28, January 1976.
- B. C. Whitmore, D. M. Gilmore, and C. Jones. What determines the morphological fractions in clusters of galaxies? *ApJ*, 407:489–509, April 1993. doi: 10.1086/172531.
- S. Zibetti, S. D. M. White, D. P. Schneider, and J. Brinkmann. Intergalactic stars in  $z \sim 0.25$  galaxy clusters: systematic properties from stacking of Sloan Digital Sky Survey imaging data. *MNRAS*, 358:949–967, April 2005. doi: 10.1111/j.1365-2966.2005.08817.x.
- F. Ziparo, P. Popesso, A. Biviano, A. Finoguenov, S. Wuyts, D. Wilman, M. Salvato, M. Tanaka, O. Ilbert, K. Nandra, D. Lutz, D. Elbaz, M. Dickinson, B. Altieri, H. Aussel, S. Berta, A. Cimatti, D. Fadda, R. Genzel, E. Le Flo'ch, B. Magnelli, R. Nordon, A. Poglitsch, F. Pozzi, M. S. Portal, L. Tacconi, F. E. Bauer, W. N. Brandt, N. Cappelluti, M. C. Cooper, and J. S. Mulchaey. The lack of star formation gradients in galaxy groups up to  $z \sim 1.6$ . *MNRAS*, 434:3089–3103, October 2013. doi: 10.1093/mnras/stt1222.
- F. Zwicky. Die Rotverschiebung von extragalaktischen Nebeln. *Helvetica Physica Acta*, 6: 110–127, 1933.
- F. Zwicky. The Coma Cluster of Galaxies. *PASP*, 63:61, April 1951. doi: 10.1086/126318.